On sensitivity analysis and estimation of soil moisture from radar responses

Yuan Liu

Yuan Liu. On sensitivity analysis and estimation of soil moisture from radar responses. Instrumentation and Detectors [physics.ins-det]. Université de Strasbourg, 2016. English. NNT : 2016STRAD032 . tel-01547494

HAL Id: tel-01547494
https://theses.hal.science/tel-01547494v1

Submitted on 26 Jun 2017

UNIVERSITÉ DE STRASBOURG

ÉCOLE DOCTORALE MATHEMATIQUES SCIENCES DE L'INFORMATION ET DE L'INGENIEUR

[Uds – INSA - ENGEES]

THÈSE présentée par:

Yuan LIU

Soutenue le 23 Septembre 2016

pour obtenir le grade de: **Docteur de l'Université de Strasbourg**

Discipline/ Spécialité: Electronique / Télédétection

Analyse de sensibilité et estimation de l'humidité du sol à partir de données radar

THÈSE dirigée par :

M. Z.-L. LI	Directeur de Recherches CNRS, France

RAPPORTEURS :

M. J. SOBRINO	Professeur, University de Valencia, Espagne
M. G. YAN	Professeur de BNU, Chine

AUTRES MEMBRES DU JURY :

Mme F. NERRY	Directeur de Recherches CNRS, France
M. K-S. CHEN	Professeur de Recherches RADI, Chine

Acknowledgments

I gained a lot of help during my Ph.D. period; there are so many great people to whom I really want to express my thanks.

My supervisor Li Zhao-liang helped me a lot both with study and life. I remember when I was just arrived in France, and I was still having problems communicating with the local people, Professor Li and his wife Mrs. Zhao helped me solved a lot of problems. Professor Li gave me the greatest patience on my study, using all he has to help me finish my research. I am so very glad for being under the tutelage of Professor Li; I express my most sincere respect and gratitude to him.

I really need to give my great respect and thankfulness to Professor Chen Kun-shan. I am so glad that he gave me the great chance to study with him. He is the most ideal teacher, who teaches students in accordance with their aptitude. He not only guided us in the academic, but also advised us in life lessons, letting us see various possibilities in one person’s future. With such a high academic achievement, he still remaining unassuming to every student, encouraging and educating us with endless patience. I am sure if I hadn’t met Professor Chen, I wouldn’t have safely graduated. The thankfulness for him is written both in here and in my mind.

Meanwhile, I present my thankfulness to my second supervisor Mr. Zeng Jiang-yuan. He helped me so much on every part of my research, shared his wisdom and methods with me, and taught me everything needed to be a qualified Ph.D. graduate. He is an outstanding intelligent person with a high efficiency in learning and working, I really thank him for his patience and time in helping me, which took him a lot of weekends and private times. Every word of my dissertation was written under his direction and supervision, he is the person who helped me the most during my research and writing period.

Thanks also for my friend Qiu Shi, who advised me a lot to help save me from many twists and turns. Thanks for Mrs. Liu Yu who helped me debug the program, always concerned, and directed my research process. Also thanks to my friend Jiang

Rui who helped me generously on programming when I was most in need. Thanks for my friend Ren Hua-zhong who was the first person to teach me how to process radar imagery and program in IDL.

Thanks for Mrs. Claudia Kuenzer who allowed me an internship at the German Aerospace Centre. Thanks for all the support of my parents.

I will remember all the help from you. I hope all of you can live happy and healthy forever.

Résumé

La diffusion des ondes électromagnétiques par une surface rugueuse aléatoire est de première importance dans de nombreuses disciplines et conduit à diverses applications notamment pour le traitement de surface par télédétection. Par exemple, il y a une pratique courante pour obtenir les paramètres géophysiques d'intérêt de la diffusion et / ou des mesures d'émission, en analysant la sensibilité du comportement et des mécanismes de diffusion. En connaissant les modes de rétrodiffusion, on peut détecter la présence de la rugosité aléatoire indésirable de la surface de réflexion telle que la réflecteur d'antenne et par conséquent trouver un moyen pour corriger ou compenser des erreurs de phase. Par conséquent, l'étude de la diffusion des ondes électromagnétiques des surfaces aléatoires est à la fois théorique et pratique. La recherche et le progrès, ayant une longue histoire, ce sujet a bien été documenté et est encore gardé à jour.

L'humidité du sol est peut-être le paramètre le plus important pour caractériser les conditions de surface qui se rapportent à l'écosystème, les prévisions météorologiques, les prévisions climatiques, la productivité agricole, les inondations et les alertes de sécheresse précoce. Par conséquent, l'acquisition de la distribution spatiale et temporelle de l'humidité du sol de surface à l'échelle à la fois locale et globale est très critique. La mesure de l'humidité du sol est difficile. La mesure in situ est en mesure de fournir une bonne précision de l'humidité du sol sur des points de référence, mais ne représente qu'une petite échelle spatiale due en partie à la forte hétérogénéité de la surface de la terre. Techniquement, les observations in situ ne peuvent pas pleinement, et en même temps, caractériser la variabilité spatiale et temporelle de l'humidité du sol à des échelles utiles. Une manière efficace consiste à déduire l'humidité du sol par satellite micro-ondes actif. La technique (SAR Synthetic Aperture Radar) est particulièrement intéressante pour la télédétection de l'humidité du sol à une résolution fine; elle fournit une mesure de la teneur en humidité du sol absolue et a l'avantage d'une couverture à grande échelle et d'un fonctionnement en tout temps. Par conséquent, les micro-ondes en mode actif, en particulier par SAR, sont considérées comme l'un des moyens les plus efficaces pour surveillance de l'humidité du sol actuellement.

Cette thèse porte sur l’obtention de l'humidité du sol de surface à partir de mesures radar. L'organisation de cette thèse est la suivante. Le chapitre 1 ouvre la présentation par une introduction du contexte, de la motivation de cette recherche, et donne un bref historique des méthodes de détermination de l'humidité du sol à l'aide de la télédétection radar. Le chapitre 2 décrit le principe de micro-ondes de la télédétection de l'humidité du sol. La description de la surface rugueuse de façon aléatoire est présentée, suivie par les interactions d'ondes électromagnétiques avec les média. En particulier, un modèle d'équation intégrale avancé (AIEM) est introduit. La validité du modèle AIEM, qui est adopté comme modèle de travail, se fait par une large comparaison avec des simulations numériques et des données expérimentales, et est exposée dans le chapitre 3. Le chapitre 4 analyse les caractéristiques des configurations radar bistatique et étudie la sensibilité de la diffusion bistatique à l'humidité du sol et à la rugosité de surface. Le chapitre 5 présente le cadre de la détermination de l'humidité du sol à partir de mesures radar en utilisant un réseau de neurones à base de filtre de Kalman récurrent. La formation du réseau et l'inversion des données sont décrits. Enfin, le chapitre 6 conclut les travaux de recherche et suggère des sujets connexes pour des recherches futures.

Récemment, il y a une nette tendance de l'expansion de monostatique à bistatique pour les mesures radar et ceci a attiré de plus en plus d'intérêt à exploiter l’information diélectrique du terrain et l'information géométrique. Un modèle théorique a été développé, pour caractériser les mécanismes de diffusion des ondes électromagnétiques pour permettre de configurer au mieux les conditions d’observation bistatique pour déduire la teneur en humidité à partir des coefficients de diffusion - multi-polarisations ou polarimétrique. Parmi les modèles théoriques, l'AIEM a démontré un éventail beaucoup plus large pour les conditions de rugosité de surface, par rapport aux modèles classiques, tels que le modèle de perturbation, le modèle optique physique, et le modèle d'optique géométrique. Pour cette raison, l'analyse numérique dans cette thèse de diffusion est basée sur le modèle de AIEM.

Chapitre 1 non seulement introduit le contexte de la recherche, mais présente également les propriétés de l'humidité du sol et le développement de la méthode de mesure de l'humidité du sol à la façon traditionnelle et à la façon de télédétection. Les méthodes traditionnelles de mesure de l'humidité du sol comprennent la méthode de pesée, la méthode de séchage rapide, la méthode de résistance et la réflectométrie dans le domaine temporel, etc. Ces méthodes peuvent estimer avec précision l'humidité du sol; pourtant, ils exigent beaucoup de mains-d'œuvre et matériaux et ne peuvent obtenir que l'information de l'humidité du sol sur une très petite échelle spatiale. Techniquement, des observations in situ ne peuvent pas caractériser, pleinement et simultanément, la variabilité spatiale et temporelle de l'humidité du sol à des échelles substantiellement applicables. La technologie de la télédétection peut jouer un rôle de plus en plus important dans la surveillance de l'humidité du sol, c'est parce qu'elle détecte les changements de l'humidité du sol à la fois temporellement et spatialement, mais aussi elle présente les avantages d'une large portée de la couverture et des observations continues. Actuellement, les informations quantitatives sur l'humidité du sol à une échelle locale ou globale est avérée très importantes dans beaucoup d'applications hydrologiques et météorologiques, y compris la gestion des ressources en eau, l'irrigation scientifique et l'estimation des rendements des cultures. La méthode traditionnelle basée sur le point ne peut pas obtenir les informations sur l'humidité du sol, ni les changements dynamiques de l'humidité du sol à une grande échelle. En revanche, la technologie de télédétection peut remédier aux insuffisances des méthodes traditionnelles, et elle est maintenant considérée comme le moyen le plus efficace pour la surveillance de l'humidité du sol dans le temps et dans l'espace, notamment à de grandes échelles spatiales.

L'application des images du satellite de télédétection pour extraire l'humidité du sol a commencé à la fin des années 1960. Bien que les observations par satellite à la bande de l'infrarouge visible-proche, à la bande de l'infrarouge thermique, et à la bande des micro-ondes ont les réponses différentes à l'humidité du sol, ils peuvent tous atteindre le but de surveiller l'humidité du sol. En conclusion, chaque méthode a ses avantages. Les modèles de la bande de l'infrarouge visible-proche peuvent surveiller l'humidité du sol aux résolutions plus fines. Cependant, les observations optiques sont souvent influencées par les nuages et les conditions atmosphériques. En outre, les capteurs optiques ne peuvent pas travailler jour et nuit. La surveillance de l'infrarouge thermique sur l'humidité du sol a une bonne précision, mais elle est aussi vulnérable à l'influence des nuages et peut éprouver facilement la saturation du signal sous l'état de la végétation dense. La première est une limitation majeure comme environ la moitié de la surface terrestre est recouverte par des nuages à n'importe quel moment. La télédétection passive par micro-ondes utilise la température de brillance pour estimer l'humidité du sol. Il peut cartographier l'humidité du sol avec une résolution temporelle élevée et avec une grande précision. Mais, comme la taille de l'antenne du capteur passif est limitée, sa résolution spatiale est trop faible pour qu'il puisse être utilisé pour certaines applications pratiques, par exemple l'estimation de la productivité agricole à une échelle locale. En revanche, la télédétection active par micro-ondes a des avantages uniques pour la surveillance de l'humidité du sol car elle est capable de travailler jour et nuit; capable de pénétrer les couches de nuages, et elle est moins affectée par les conditions atmosphériques; elle est directement liée à l'humidité du sol par permittivité du sol, et elle peut fournir des observations avec une résolution spatiale beaucoup plus élevée que les capteurs passifs de micro-ondes. Par conséquent, nous avons utilisé les observations de télédétection active par micro-ondes pour récupérer l'humidité du sol dans cette thèse de recherche.

Le problème difficile pour la récupération de l'humidité du sol est que la relation entre l'humidité du sol et le coefficient de rétrodiffusion n’est pas linéaire. La rugosité, la couverture végétale, la constante diélectrique, les propriétés physiques du sol (structure, composition, etc.) et les paramètres de radar affectent tous la force de l'écho. Les couches de végétation ont une épaisseur suffisante pour protéger les informations de diffusion à partir de la surface du sol, alors, la végétation est généralement considérée comme le facteur le plus important qui affecte la précision de la récupération de l'humidité du sol. Pour optimiser l’inversion de l'humidité du sol, les chercheurs ont recommandé qu'un angle d'incidence faible avec une bande de longueur d'onde (bande L) puisse minimiser les effets de la rugosité de la surface et de la végétation. La rugosité de la surface (la hauteur moyenne quadratique s, la longueur de corrélation l et la fonction d'autocorrélation statistique) est un autre facteur important. Des études de sensibilité des paramètres sur les signaux de radar provenant d'une variété de surfaces de sol indiquent que la contribution de la rugosité de surface au signal de radar est équivalente ou même supérieure à celle de l'humidité du sol. Par conséquent, l'une des tâches les plus difficiles de la télédétection active par micro-ondes de l'humidité du sol est de découpler les effets de l'humidité du sol et la rugosité de surface. Les chercheurs ont trouvé que l'utilisation du rapport de polarisation peut minimiser l'effet de la rugosité. Théoriquement, la méthode de multi-polarisation peut améliorer la précision de récupération. Pendant les trente dernières années, de nombreux modèles ont été développés, qui peuvent quantitativement décrire la relation entre le coefficient de diffusion et l'humidité du sol. Les modèles de la diffusion de surface les plus couramment utilisés sont divisés en trois catégories: les modèles théoriques, les modèles semi-empiriques et les modèles empiriques. Les modèles théoriques comprennent principalement le modèle Kirchhoff (par exemple, le modèle de l'optique physique et le modèle de l'optique géométrique, ainsi que d'un petit modèle de perturbation), le modèle d'équation intégrale, et le modèle d'équation intégrale amélioré et avancé. Les modèles empiriques et semi-empiriques se comportent principalement le modèle Oh, le modèle Dubois et le modèle Shi. Peut-être les modèles empiriques et semi-empiriques ne sont pas applicables pour l'ensemble des données autres que ceux qui sont utilisés dans leur développement. En raison de sa complexité et l'exigence d'une connaissance détaillée de la rugosité de la surface, il est difficile d'inverser l'humidité du sol en utilisant directement les modèles théoriques. Toutefois, ils peuvent être utilisés pour prédire précisément les rendements de diffusion pour une variété de profils de surface, qui est très utile pour la compréhension du mécanisme de la diffusion de la surface.

Le chapitre 2 est consacré à la description des surfaces rugueuses de façon aléatoire. Bien que les propriétés fractales aient été étudiées dans le contexte de la description d'une surface aléatoire, nous avons adopté une méthode plus classique, et plus communément utilisé qui mesure l'échelle de rugosité horizontale, et la racine carrée moyenne (RMS) hauteur, qui représente l'échelle de la rugosité verticale et qui appelée l'approche. Les fonctions de corrélation utilisées de manière courante, ou de manière équivalente, les spectres de puissance pour les surfaces naturelles sont donnés. Dans ce chapitre, les interactions électromagnétiques ondes-matière sont brièvement discutées au moyen de Electric Field Integral Equation (EFIE) and Magnetic Field Integral Equation (MFIE) qui sont deux équations fondamentales qui régissent les champs tangentiels de surface à partir de laquelle les champs dispersés peut être déterminé de manière unique. Il est également connu que le modèle AIEM a été développé en résolvant de manière itérative ces deux équations jusqu'au second ordre.

Cette thèse de recherche a utilisé des bandes de micro-ondes pour étudier les caractéristiques du sol. Son mécanisme est l’autorotation et la rotation des molécules de matière, ainsi que l'interaction entre l'autorotation des électrons et des ondes électromagnétiques émises, qui décide le mécanisme d'interaction intrinsèque entre les caractéristiques de la surface et le radar imageur utilisé dans le spectre de micro-ondes. Une image radar reflète l'interaction entre les ondes électromagnétiques émises par le radar et les objectifs des caractéristiques de la surface. Les ondes électromagnétiques émises par les capteurs radar révèlent les courants électriques sur la surface des cibles. Par le rayonnement, les ondes électromagnétiques d'incidence et les cibles de détection interagissent dans la région du champ lointain de l'antenne, qui produit les ondes électromagnétiques de diffusion et qui modifie l'amplitude, la fréquence, la position de phase, le mode de polarisation et d'autres paramètres de l'écho. La qualité d'une onde de diffusion est différente de celle d'une onde d'incidence: elle comprend l’information de la structure physique sur les cibles, qui est un support de l'information cible. Ceci est provoqué par l'effet de modulation des cibles sur les ondes électromagnétiques d’incidence. L'effet de modulation est déterminé par les caractéristiques de la structure physique des cibles. Les différents objectifs ont les caractéristiques de modulation différentes sur la même onde d'incidence. La télédétection de radar extrait les paramètres des caractéristiques des cibles en fonction de la variance de modulation, c’est-à-dire, les différentes cibles affectent différemment les ondes électromagnétiques. La valeur mesurée basique de chaque pixel d'une image est une paire de valeurs de tension. Ces valeurs mesurées indiquent l'impact de l'information de la surface sur l'onde transmise, qui décrit essentiellement la propagation en espace de Maxwell et l'équation de l’équation caractéristique de la diffusion. L'équation radar peut montrer les relations entre le système radar, le cible de détection et les signaux reçus.

Certains modèles typiques de la diffusion de micro-ondes de la surface sont le modèle Oh, le modèle Dubois et l'AIEM (modèle avancé d'équation intégrale). Cependant, le modèle Oh est déconseillé car il a de grandes erreurs dans la valeur analogique des données de diffusion de la co-polarisation, même si elle peut simuler les caractéristiques de la diffusion de la polarisation croisée. Le modèle Dubois a une réponse différente à la situation actuelle (changement de l'angle d'incidence et la constante diélectrique), comme il est une sorte de modèle empirique qui manque de l'appui de la théorie physique. Comme ce que nous avons présenté dans les chapitres précédents, l'AIEM (modèle avancé d'équation intégrale) a une grande précision par rapport aux simulations et aux mesures sur le terrain et donc il a été adopté comme modèle de travail dans cette recherche. L'analyse des caractéristiques du radar par l'AIEM pourrait nous aider à mieux comprendre les caractéristiques de la rétrodiffusion de radar.

Dans le chapitre 3, nous avons validé les prédictions de AIEM par comparaison avec des simulations numériques et des données expérimentales. L'étude de la diffusion des micro-ondes a de larges applications dans la télémétrie, la transformation sans fil, la détection de radar etc. Un modèle de diffusion de surface pratique et fiable est nécessaire pour obtenir une bonne compréhension du mécanisme de la diffusion de surface. La recherche sur la diffusion des micro-ondes sur une surface aléatoire a été en cours depuis plus de quarante ans. Pendant les années 1960 à 1970, plusieurs modèles de diffusion de surface ont été développés, y compris le petit modèle de perturbation (SPM) et le modèle Kirchhoff. Ces deux modèles sont considérés comme les normes prééminentes dans leur champ d'application. Le SPM est capable dans la basse fréquence et les circonstances de petite surface de perturbation, alors que le modèle Kirchhoff est adapté à la haute fréquence et les surfaces rugueuses à grande échelle. Depuis 1990, le Dr A. K. Fung a proposé le modèle de l'équation intégrale (IEM) qui résout d'abord la limitation du champ d'application. L'IEM original a été développé sur la base de plusieurs approximations simplificatrices conduisant à la solution d'une paire d'équations intégrales, relativement simple, et pourtant assez précise, gouvernant les courants de surface. Il y a eu des progrès significatifs dans l'amélioration de l'estimation du courant de surface pour étendre sa région de validité. Cependant, dans le modèle d'IEM, la dépendance de la hauteur de la surface sur la phase de la fonction de Green a été ignorée, ce qui conduit à une erreur importante hors de la direction de rétrodiffusion.

Le modèle AIEM est une extension base sur le physique du modèle analytique IEM. Il montre les améliorations significatives pour la diffusion unique et les prédictions d'émissivité pour une portée large d'échelles de rugosité, surtout dans les régions de rugosité intermédiaires. En plus, la diffusion de multiple-surface se convient bien avec les résultats de simulation numérique et les mesures de laboratoire contrôlées acquises à partir des surfaces connues. L'AIEM a supprimé certaines hypothèses faibles de l'IEM original. Bien que l'AIEM soit théoriquement considéré pour offrir les prédictions précises, le niveau de précision de ses prédictions doit encore être confirmé.

Tout d'abord, nous avons comparé AIEM à des simulations numériques pour la rétrodiffusion et de la diffusion bistatique. Dans la rétrodiffusion, nous avons comparé AIEM avec le Méthode numérique 3D des équations de Maxwell (NMM3D), qui est une méthode de moment (MoM) appliquée pour calculer diffusion de surface rugueuse et est adapté pour une application à la fois pour la télédétection active et passive. Dans les conditions bistatiques, nous avons comparé l’AIEM avec les résultats numériques l’approximation des pentes faibles (SSA) et le MoM dans la diffusion plane. Les résultats montrent que comparer avec les données de simulations numériques, toutes les prédictions sont très proches les unes des autres, sauf en cas de grand événement / angle de diffusion. Nous avons également comparé le modèle AIEM avec des mesures en rétrodiffusion et en conditions de diffusion bistatique. Le POLASCAT LCX de l'Université du Michigan a été conçu avec pour mesurer la matrice de diffusion de points des cibles distribués à des fréquences de 1,5, 4,75, 9,5 GHz. Les ensembles de données ont été mesurés dans deux conditions d'humidité différentes, relativement humides et relativement secs. Les surfaces des paramètres de rugosité tels que la RMS, la longueur de corrélation et la pente de la RMS ont été calculées à partir des profils de hauteur de la surface de mesure. Les résultats montrent que l'AIEM est en bon accord avec les données mesurées dans tous les cas. Dans le cas de la diffusion bistatique, les données ont été acquises sur des surfaces connues fournies par Laboratoire européen de signature micrométrique (EMSL). En comparant avec les données de mesure de l’EMSL, l’AIEM montre également un bon accord, bien que les prévisions de l'AIEM sauf aux grands angles de diffusion et que la séparation entre les polarisations n’est pas assez importante. De façon générale, les prévisions de AIEM correspondent bien à la fois aux simulations numériques et aux données expérimentales.

Le système traditionnel de radar actif détecte presque entièrement l'humidité du sol basée sur les coefficients de rétrodiffusion. Pourtant, le réglage de l’émetteur et le récepteur dans la même direction présente les inconvénients apparents théoriques, car seul le signal provenant de la direction d’inverse peut être obtenue. L'un des problèmes critiques dans l'estimation des paramètres de surface à partir des signaux radar de rétrodiffusion est que les paramètres de surface, y compris la rugosité statistique de surface (la hauteur moyenne quadratique s et la longueur de corrélation l) et la constante diélectrique sont fortement couplés sous un certain ensemble de paramètres de radar (fréquence, l'angle d'incidence et la polarisation). Ce fait entrave considérablement la capacité de détection des micro-ondes de l'humidité du sol, même pour les surfaces nues. Ainsi, il est intéressant de comprendre les caractéristiques de la diffusion bi-statique (qui sont beaucoup moins comprises par rapport à la rétrodiffusion) afin de trouver une configuration d'émetteur-récepteur appropriée pour découpler, à un niveau optimal, la rugosité de surface et la constante diélectrique. Mais, dans la configuration bi-statique, il existe de nombreux scénarios à être conçus. Alors, il est essentiel de mener une analyse de sensibilité des paramètres pour déterminer une configuration optimale qui peut maximiser le contenu de l'information des paramètres d'intérêt tout en minimisant la contribution des paramètres indésirables.

Par conséquent, l'estimation de l'humidité du sol dans un mode bi-statique a attiré une attention croissante au cours des dernières années. Dans certaines études, les chercheurs ont trouvé que, en comparaison avec l'observation mono-statique traditionnelle, l’utilisation des géométries bi-statique peut obtenir plus d'informations pour récupérer l'humidité du sol. Mais, la littérature limitée est disponible pour la détection de l'humidité du sol avec la configuration bi-statique. Ainsi, plus de travail doit être effectué pour explorer les comportements de diffusion bi-statique avec les paramètres du sol dans les diverses conditions de sol, il s’agit à la fois de l'intérêt théorique et pratique. Plusieurs facteurs influent sur la caractérisation de la rugosité du sol. En plus de longueur de corrélation et de la hauteur moyenne quadratique (hauteur RMS), la fonction d'autocorrélation de surface (ACF) a aussi une influence importante. Dans les situations pratiques, les ACFs sont difficiles à déterminer. En conséquence, l'effet des ACFs est généralement ignorée ou simplement supposé a priori pour simplifier le problème d'inversion dans le processus d'inversion. Alors, comment supprimer l'effet des ACFs pour l'estimation de l'humidité du sol plus fiable est aussi un défi attrayant.

Dans le chapitre 4, nous avons effectué une analyse de sensibilité des paramètres pour la diffusion bistatique d’une surface rugueuse. La diffusion radar d’une surface de sol nu rugueuse aléatoirement est complexe et est déterminée par l'humidité du sol et la rugosité de surface d'une manière fortement non linéaire. Découpler les effets de l'humidité du sol et de la rugosité de surface est essentielle si l'inversion de l'humidité du sol est l’intérêt majeur. Utiliser uniquement la rétrodiffusion est difficile, sinon impossible, car seul le signal provenant de l'arrière est disponible. Par conséquent, l'estimation de l'humidité du sol dans un mode bistatique a attiré une attention considérable ces dernières années. Pour obtenir une meilleure compréhension des caractéristiques de diffusion bistatique, et trouver les configurations appropriées, voire optimales, nous avons étudié la réponse radar bistatique de l'humidité du sol et de la rugosité de surface des surfaces de sol nu dans la bande L en utilisant le modèle AIEM. Les résultats montrent que la sensibilité la plus élevée de diffusion radar à l'humidité du sol peut être obtenue en configurant l'observation bistatique par rapport à l'observation monostatique à partir duquel seuls les coefficients de rétrodiffusion peuvent être obtenus. Dans un mode bistatique, les coefficients de diffusion de polarisation VV sont généralement plus sensibles à l'humidité du sol que celles de polarisation HH. Contrairement à l'utilisation d'un seul coefficient polarisé ou simple diffusion angulaire, l’influence de la fonction de corrélation, qui est un effet indésirable, peut être considérablement supprimé par une combinaison de doubles polarisation ou de double mesures angulaires. Par rapport aux résultats en simple polarisation ou en données combinées de double polarisation, il semble que la combinaison de double mesures angulaires réalise l'estimation de l'humidité du sol la plus fiable car elle permet de supprimer l'influence de la rugosité de surface, tout en maintenant une bonne sensibilité à l'humidité du sol. Il est également important à noter que la région vers l’avant est préférable indépendamment de la fonction de corrélation, une caractéristique tout à fait attrayante et utile. De plus, il apparaît que plus la différence entre les angles croît, plus la sensibilité des mesures angulaires à l'humidité du sol augmente. Il convient de noter que, bien que les configurations de radar bistatique montrent un grand potentiel pour la surveillance de l'humidité du sol, les limitations imposées par la fenêtre angulaire étroite et le niveau faible de signal dans ces configurations hors-plan sont susceptibles de rendre l'utilisation de ces configurations difficiles. Enfin, en raison de la complexité géométrique de la configuration bistatique, ainsi que la diversité des conditions de surface, des études théoriques et expérimentales complémentaires devraient être menées pour confirmer la meilleure configuration bistatique pour la détection de l'humidité du sol dans le futur.

Dans le chapitre 5, nous avons analysé la réponse en rétrodiffusion radar de l'humidité du sol et, pour tester les données réelles, développé une méthode pour extraire l'humidité du sol à partir des données du ALOS-2 (Advanced Land Observing Satellite-2). Cependant, la récupération de l'humidité du sol à partir de données SAR est complexe, car elle est profondément affectée par la rugosité de la surface, la couverture végétale et la texture du sol, entre autres facteurs. Le modèle AIEM a été de nouveau utilisé pour simuler les caractéristiques de diffusion radar de la surface du sol pour analyser les effets de couplage des paramètres de surface, y compris la hauteur de RMS, la longueur de corrélation, l'humidité du sol, ainsi que les paramètres du système radar, y compris l'angle d'incidence et de polarisation.

De la sensibilité des coefficients de rétrodiffusion à l'humidité du sol sous différentes fréquences, nous voyons que le changement des coefficients de rétrodiffusion est plus importante dans la bande L quand les changements d'humidité du sol varient. Nous observons que la sensibilité des signaux de rétrodiffusion à l'humidité du sol est élevée lorsque l'angle d'incidence est relativement faible dans la polarisation VV. La sensibilité des signaux de rétrodiffusion à l'humidité du sol diminue à mesure que la hauteur de RMS augmente. Par ailleurs, on constate que l'influence de la longueur de corrélation des signaux de rétrodiffusion est nettement inférieure à celle de la hauteur RMS.

Un modèle de données permet une mise en correspondance de l'espace de mesure à l’espace des paramètres. Comme nous l'avons vu dans les chapitres précédents, la diffusion radar de par une surface rugueuse est un processus complexe, et les paramètres de surface sont fortement couplés. Pour résoudre les problèmes de recherche multidimensionnelle, la méthode de réseau neuronal à base de filtre récurrent de Kalman a été développé en raison de sa capacité à s’adapter à des dimensions géophysiques élevées, de sa robustesse au bruit et surtout sa capacité à gérer la cartographie non linéaire. Pour l'essentiel, l'opération peut être divisé en deux phases. La première phase est la formation de réseau - pour construire la fonction de mappage. Nous avons utilisé le modèle AIEM pour générer la base de données d’apprentissage en configurant les paramètres de radar (fréquence, angle d'incidence, polarisation) et les paramètres de surface (l'humidité du sol, hauteur RMS, fonction de corrélation, et la longueur de corrélation). Après avoir terminé la formation du réseau, nous procédons à la deuxième phase qui est le fonctionnement du réseau neuronal, à savoir, la récupération de l'humidité du sol. En utilisant la base de données générée pour former le réseau de neurones à base de filtres de Kalman, nous avons vérifié les résultats avec les données simulées à l'exception des données d'apprentissage. Les résultats montrent que la précision sur l'humidité du sol et sur la hauteur RMS est meilleure que celle de la longueur de corrélation, et est généralement satisfaisante.

Il s’agit maintenant de tester le processus sur des données réelles. La zone d'étude est le delta du fleuve Jaune (YRD), l'un des plus grands deltas en Chine formés par les limons du fleuve Jaune dans la province du Shandong, en Chine. Dans le temps, la rivière Huang He coulait dans le nord du Jiangsu dans la mer Huanghai et cela pendant près de 700 ans. Le delta du fleuve Jaune, est situé dans la province du Shandong de 13 °21'-38 °12 'N et 118 °07'-119 °10'E, avec une superficie de 5450 km². Dans cette étude, nous avons utilisé deux ensembles d’images de niveau 1.0 ALOS-2, une a été acquis le 13 Novembre 2014, et l'autre le 20 Décembre 2014. La fréquence du ALOS-2 est de 1,2 GHz et la largeur d'observation est de 25 km avec une résolution de 3 mètres dans le mode "spotlight". Les deux images étaient toutes deux situées dans la zone YRD, avec une zone substantielle de recouvrement. Nous avons choisi une région de sol nu pour tester notre méthode. Après l'application de la méthode d'inversion développée en utilisant les deux données ALOS-2, nous avons obtenu la variation relative de l'humidité du sol de la zone de recherche. D'après les résultats, nous pouvons voir que la distribution spatiale de la variation de l'humidité du sol est relativement uniforme. Dans la plupart de la région, l'humidité du sol a été asséchée. Le relativement plus important changement relatif d'humidité du sol a eu lieu dans la limite sud de la zone. La limite était humide sans doute en raison de sa proximité de la mer. De façon générale, la répartition spatiale de la variation de l'humidité du sol est raisonnable, ce qui démontre l'efficacité de la méthode.

Nous tirons les conclusions dans le chapitre 6. Dans cette thèse, nous présentons une analyse systématique des diffusions radar bistatiques de surface rugueuse aléatoire basée sur un mode AIEM théorique, modèle bien connu. Par la suite, une analyse de sensibilité a été effectuée pour explorer les processus complexes et le couplage non linéaire des interactions onde-matière, dont la teneur en humidité du sol est l'un intérêt majeur. Puis nous procédons à l'inversion du problème - la récupération de l'humidité du sol à partir de mesures radar. Le déficit en utilisant uniquement des coefficients de rétrodiffusion, dans la mesure où la détermination de l'humidité du sol est principalement concernée, a été mis en évidence et sa compensation par le biais de mesures de diffusion bistatique est discutée. Des études futures sont alors suggérées.

Publications durant la thèse :

Liu, Y., Chen, K.-S, Li, Z.-L, and Zeng, J.-Y., "On Estimation of Surface Parameters From Radar Bistatic Scattering," to be submitted to *IEEE TGARS*, 2016.

Liu, Y., Chen, K.-S,, **Liu, Y.**, Li, Z.-L, Zeng, J.-Y., and Xu, P., "On Angular Features of Radar Bistatic Scattering from Rough Surface," under review, *IEEE TGARS*, 2016.

Liu, Y., Chen, K.-S., Li, Z.-L., Liu, Y. (2015). Radar response of soil moisture from ALOS-2 SAR, *Progress In Electromagnetics Research Symposium (PIERS), Prague,* Abstract, oral presentation.

Liu, Y., Zeng, J.-Y., Chen, K.-S. and Li, Z.-L. (2016). Parameter sensitivity analysis for bistatic scattering of rough surface, *International Geoscience and Remote Sensing Symposium (IGARSS).*

Zeng, J.-Y., Chen, K.-S., **Liu, Y.**, Bi H.-Y., Chen, Q. (2016). Response of bistatic scattering to soil moisture and surface roughness at L-band, *International*

Geoscience and Remote Sensing Symposium (IGARSS).

Zeng, J.-Y., Chen, K.-S., Bi, H.-Y., Chen, Q., **Liu, Y.** (2016) A preliminary assessment of the SMAP radiometer soil moisture product using three in-situ networks, *International Geoscience and Remote Sensing Symposium (IGARSS)*.

Liu, Y., Chen, K.-S., **Liu, Y.**, Li, Z.-L., Xu, P., Zeng, J.-Y., Jin, M. (2016). Modeling and characteristics of bistatic scattering from rice canopy, *International Geoscience and Remote Sensing Symposium (IGARSS).*

Contents

List of Tables

List of Figures

Chapter 1 Introduction

1.1 Background

Soil moisture, which is also called the soil water content, is one of the surface parameters which has been widely used in various environmental applications, including weather and climate forecasting, agricultural productivity predictions, flood monitoring, and drought early warning (Entekhabi et al., 2014; Miralles et al., 2014; Taylor et al., 2012; Zeng et al., 2016a). It plays a significant role in numerous hydrological-related processes. Many studies have proved that soil moisture observations at large scales are very useful in hydrology, meteorology, climatology, and agriculture (Bi et al., 2016; Koster et al., 2004; Jung et al., 2010). Therefore, acquiring the temporal and spatial distribution of surface soil moisture at both local and global scales is essentially critical.

Traditional methods of soil moisture measurement include the weighing method, rapid drying method, resistance method and time domain reflectometry, etc. These methods can accurately estimate the soil moisture; however, they require a lot of manpower and materials and can only obtain soil moisture information over a very small spatial scale (Tian et al., 1991). Currently, hydrological and meteorological stations can provide only sparse spatial points of soil moisture information, which cannot fully characterize the spatial and temporal variability of soil moisture and also cannot effectively investigate its impact on environmental change (Li et al., 2010). Technically, in situ observations are not able to fully, and simultaneously, characterize the spatial and temporal variability of soil moisture at substantially applicable scales (Zeng et al., 2015b).

Remote sensing technology plays an increasingly important role in soil moisture monitoring. Not only can it detect changes in soil moisture both temporally and spatially, but also it has the advantages of a wide range of coverage and continuous observations (Zhang et al., 2010). Currently, quantitative information on soil moisture at a local or global scale has proved to be of palpable importance in many hydrological and meteorological applications, including management of water resources, scientific irrigation and estimation of crop yields. The traditional point-based method cannot obtain soil moisture information as well as the dynamic changes in soil moisture at a large scale (Shao et al., 2006). In contrast, remote sensing technology can make up for the shortcomings of the traditional methods, and it is now considered to be the most effective means for soil moisture monitoring in both time and space, especially at large spatial scales.

1.2 Properties of soil moisture

Soil layers, in the direction of the cross section, can be divided into three layers: the surface soil, the subsoil and parent material. The colour of topsoil humus layers is deeper, and this layer is richer in flora and fauna conversion of organic matter, therefore crop farming is carried out on this layer. The colour of the subsoil layer is lighter, and it contains less organic matter. The parent material is mainly composed of rock after weathering inorganic composition. Climate, topography, vegetation and time will affect the physical and chemical properties of soil. Soil is composed of solids (minerals and organic matter particles), liquids (soil moisture), and gases (air). Mechanical soil composition refers to the proportions in each soil of different grain sizes (sand, silt and clay), or so-called soil texture. Soil porosity is composed of part of the common air and soil moisture. Soil moisture content can use different means of expression, as shown below.

1.2.1 Volumetric water content

Volumetric water content *mv*, also known as the volumetric moisture content, is the unit of soil moisture volume, which can be expressed as the percentage:

$$mv = v_w \ / \ v_t \tag{1.1}$$

where $\mathrm{v_w}$ and $\mathrm{v_t}$ represent the volume of water in the soil and the total volume of soil (units: cm^3), respectively. Care must be taken that it is not the volume of solid soil particles.

1.2.2 The quality of the water content

The quality of the water content mg, also known as the weight moisture content, is the ratio of soil moisture quality and the weight of the soil after drying:

$$mg = m_w \ / \ m_s \tag{1.2}$$

where m_w represents the soil moisture quality (units: g) and m_s represents the weight of the soil after drying. The relationship between the volumetric water content and the weight moisture content can be described as:

$$mv = \rho_b \ / \ m_g \tag{1.3}$$

where ρ_b is the soil bulk density, also called the bulk density (units: g/cm^3).

1.2.3 Relative water content

Relative water content (RWC) is the ratio of the soil moisture content and field capacity, which represents the soil water saturation level.

$$RWC = \quad soil \ moisture \ content \ / \ field \ capacity \quad * \ 100\% \quad . \tag{1.4}$$

In agricultural and hydrological studies, the field capacity represents the soil moisture after irrigation over two days.

1.3 Remote sensing of soil moisture

Application of remote sensing satellite images to extract soil moisture began in the late 1960s. Although satellite observations at the visible-near infrared band, thermal infrared band, and microwave band have different responses to soil moisture, they all can achieve the purpose of monitoring soil moisture (Wang and Qu, 2009).

1.3.1 Visible-near infrared remote sensing of soil moisture

With the visible-near infrared band, soil moisture detection is based on the characteristics of the vegetation reflectance spectra. According to the imaging mechanism of remote sensing and object spectrum characteristics, dry soils have a high reflectivity: soil reflectivity will decrease as the soil becomes wetter. The main indices used to detect soil moisture are divided into two categories: the remote sensing index method and the temperature-vegetation index spatial characteristics method.

1.3.1.1 Remote sensing index method

Under stable temperature and light conditions, soil moisture is the major factor that affects vegetation growth. Studies have shown that vegetation indices, such as the vegetation condition index (VCI) (Kogan, 1998), can reflect water shortage in crops, and thus can be closely related to soil moisture. In addition to soil moisture, air temperature and rainfall and other environmental factors also affect the vegetation index, therefore it cannot fully reflect any water shortages. However, combined with the vegetation temperature canopy (TC) and the normalized difference vegetation index (NDVI), soil moisture information can be extracted under vegetation cover. The vegetation supply water index (VSWI) is defined as the ratio of NDVI to TC. As the soil becomes drier, then NDVI decreases, TC increases, and VSWI decreases; in contrast, when the soil gets wetter, then NDVI increases, TC decreases, and VSWI increases. According to this principle, any soil drought under an area of vegetation coverage can be detected (Carlson et al., 1994). In addition, some remote sensing humidity indices, such as the normalized difference water index (NDWI), and the normalized difference moisture index (NDMI) (Gao, 1997), can also extract humidity information.

1.3.1.2 The temperature-vegetation index spatial characteristics method

In 1985, Goward et al. (1985) proposed the temperature-vegetation index spatial characteristics method. In most cases, the NDVI and surface temperature (Ts) have a negative correlation: the greater the inclination, the lower the soil moisture. Studies have shown that the temperature-vegetation index (TVX) method has a great potential for monitoring the regional soil moisture (Goward et al., 2002). In addition, Sandholt et al. (2002) have developed a simplified temperature vegetation dryness index (TVDI) which is directly related to the soil moisture and, also, does not rely on secondary data.

1.3.2 Thermal infrared remote sensing of soil moisture

Thermal infrared remote sensing of soil moisture, which is based mainly on the soil surface emissivity and temperature, uses two main methods: the thermal inertia method and the plant evapotranspiration and water stress index method.

1.3.2.1 Thermal inertia method

Soil thermal inertia is a kind of soil thermal property. The change of soil temperature is caused by internal factors and, as the thermal inertia of soil is less than that of water, so soil with a higher moisture content will have a greater thermal inertia. Therefore, thermal inertia and soil moisture are closely related. By establishing the relationship between the soil thermal inertia and remote sensing data, as well as the relationship between soil moisture and thermal inertia, then a model used to describe the relationship between soil moisture and remote sensing data can be established (Lasne et al., 2004).

1.3.2.2 Plant evapotranspiration and plant water stress index method

Plant evapotranspiration consists of two parts: evaporation and transpiration. Evaporation is the plant’s surface moisture being diffused into the atmosphere. Transpiration is the diffusion of soil moisture into the atmosphere through the plants.

The basic principle of the plant evapotranspiration and plant water stress index method is that there is a relationship between the canopy temperature and plants, a relationship that can be used to extract soil moisture data. The vegetation water stress index (VWSI) and the crop water stress index (CWSI) reflect soil moisture information at the range of the plants’ root area (Jackson et al., 1981). Based on the energy balance, by use of the surface albedo, surface radiation temperature and weather station data, and a combination of canopy temperature, temperature difference and aerodynamic resistance, the actual evapotranspiration and potential evapotranspiration can be obtained. Then the soil moisture can be estimated. This method is physically-based, which can overcome the limitations of empirical models.

1.3.3 Microwave remote sensing of soil moisture

1.3.3.1 Passive microwave remote sensing of soil moisture

The physical basis of using passive microwave remote sensing for soil moisture monitoring is that microwave brightness temperature is highly related to the soil dielectric constant, which is mainly determined by soil moisture (Zeng et al., 2014). The current spaceborne passive microwave satellites/sensors for soil moisture measurements mainly include the Soil Moisture and Ocean Salinity (SMOS) satellite (de Jeu et al., 2009; Kerr et al., 2012; Saleh et al., 2009; Wigneron et al., 2007), the Fengyun-3 (FY3) (Shi et al., 2006; Parinussa et al., 2014), the Advanced Microwave Scanning Radiometer 2 (AMSR2) (Koike et al., 2004; Njoku and Chan, 2006; Owe et al., 2008; Zeng et al., 2015a), and the Soil Moisture Active Passive (SMAP) satellite (Entekhabi et al., 2010, 2014; Zeng et al., 2016a). Overall, retrieving soil moisture from passive microwave brightness temperature mainly consists of two parts: the first part is use of a radiative transfer model to link the brightness temperature and the soil dielectric constant. The second part is use of a dielectric mixing model to link the soil permittivity and soil moisture. Overall, the current inversion algorithms can be divided into four categories. First is the single-channel algorithm (SCA) that uses only single polarized brightness temperature measurements along with lots of auxiliary data to retrieval soil moisture (Jackson, 1993; Zeng et al., 2016a). The second is the multi-parameter iterative inversion algorithm, which can estimate several parameters simultaneously (e.g. soil moisture, vegetation optical depth and surface temperature) (Kerr et al., 2012). The third is the polarization-index algorithm which uses the polarization index to estimate soil moisture (Njoku and Chan, 2006). The fourth is the intelligent inversion algorithm, e.g. neural network and genetic algorithm (Santi et al., 2012; Wigneron et al., 2003).

1.3.3.2 Active microwave remote sensing of soil moisture

Microwave signals can not only penetrate clouds, but also can penetrate vegetation and soil to some extent. The bare soil’s backscattering coefficients receive by the active microwave sensors (e.g. radar) have a strong correlation with soil moisture (Baghdadi et al., 2011; Zribi et al., 2014a). In addition, the backscattering signals are also affected by many other factors, such as vegetation cover, surface roughness, and soil texture (Barrett et al., 2009; Kornelsen and Coulibaly, 2013). The key to improving the retrieval accuracy of soil moisture is to remove effectively the effects of surface roughness and vegetation cover (Bryant et al., 2007).

Over the past decades, researchers have achieved great success in terms of soil moisture inversion for areas of bare soil or sparse vegetation cover. Many models have been developed for soil moisture inversion or prediction of the scattering returns for a variety of surface profiles. The empirical or semi-empirical models mainly include the Oh model (Oh et al., 1992), the Dubois model (Dubois et al., 1995), and the Shi model (Shi et al., 1997). The theoretical models mainly include the physical optic model (POM), the geometric optic model (GOM), the small perturbation model (SPM), the Integral Equation Model (IEM) (Fung et al., 1992), and the advanced integral equation model (AIEM) (Chen et al., 2003).

The Oh model was developed based on the multiband fully polarimetric scatterometer data. The Oh model can be applied to a wide range of soil roughness. Especially when the RMS height s of the soil surface is in the range of 0.1 cm to 0.6 cm and the correlation length l is in the range of 2.6 cm to 19.7 cm, then the model predictions are more consistent with the actual measurements. However, a lot of ground observation data with limited surface condition information has been used to build the Oh model, thus its universality needs more in-depth analysis and verification.

The Dubois model was developed based on multi-band and multi-polarization scatterometer data. When the ks is less than 2.5 (k is the wave number, s is the RMS height), the incident angle is larger than 30°, and soil volumetric water content is less than 35%, the Dubois model has a good accuracy. However, when the ks is larger than 2.5, the Dubois model can no longer describe the radar backscatter of a rough surface. Based on the IEM model, Shi et al. (1997) analysed the effects of different soil parameters (soil roughness and soil dielectric constant) on the scattering signals, then they built the relationship between backscattering coefficients and soil moisture at the L-band. In the Shi model, the surface roughness spectrum which affects the scattering coefficient has also been involved.

The Kirchhoff approximation model includes the GOM model and the POM model. The GOM model assumes that when the soil surface RMS height s is larger, scattering is completely incoherent. The scattering coefficient is calculated by using the stationary-phase approximation method. The GOM model is suitable for large surface roughness. The POM model assumes that when the RMS height *s* is small, there is a coherent scattering. When the *ks*=0, it obtained pure coherent reflection. Under that situation, the POM model uses an approximation analog method to simulate the scattering characteristics of target objects. The POM model is suitable for medium surface roughness. When the surface becomes smooth, the Kirchhoff model is no longer applicable. The SPM model is suitable for relatively smooth, and a smaller correlation length surfaces. The IEM model is a theoretical model based on a microwave radiation transfer equation. It can simulate the real situation of soil backscatter value in a large surface roughness range. IEM shows both a high simulation accuracy and easier operation in practical applications. The AIEM is extended from the IEM, but its prediction accuracy is much improved compared to the original IEM (Chen et al., 2003; Wu et al., 2008). It has been the model most often chosen as the forward model to simulate the scattering coefficients of bare soil surfaces with various ground conditions in many previous studies (Brogioni et al., 2010; Pierdicca et al., 2008).

1.3.4 Summary of remote sensing methods

In conclusion, each method has its advantages. Visible-near infrared band models can monitor soil moisture at finer resolutions. However, optical observations are often influenced by clouds and atmospheric conditions. Also, the optical sensors cannot work all day and night. The thermal infrared monitoring of soil moisture has a good accuracy, but it is also vulnerable to the influence of clouds and may experience signal saturation easily under the condition of heavy vegetation. The former is a major limitation since about half of the land surface is covered by clouds at any one time (Zeng et al., 2015a). Passive microwave remote sensing uses brightness temperature to estimate soil moisture. It can map soil moisture with high temporal resolution and high accuracy. However, since the antenna size of the passive sensor is limited, its spatial resolution is too low for it to be used for some practical applications such as agricultural productivity estimation at a local scale (Kornelsen and Coulibaly, 2013). In contrast, active microwave remote sensing has unique advantages for soil moisture monitoring as it: (a) is capable of working both day and night, (b) is able to penetrate cloud layers, and is less affected by atmospheric conditions, (c) is directly related to soil moisture through soil permittivity, and (d) can provide observations with much higher spatial resolution than passive microwave sensors. Therefore, we used active microwave remote sensing observations to retrieve soil moisture in this dissertation research.

1.4 Research status of active remote sensing of soil moisture

Estimating soil moisture from active microwave remote sensing began with Ulaby's experiments (Rao et al., 1993). The challenging issue for soil moisture retrieval is that the relationship between soil moisture and the backward scattering coefficient is not linear. Roughness, vegetation cover, dielectric constant, soil physical properties (structure, composition, etc.) and radar parameters all affect the strength of the echo. Vegetation layers have a thickness sufficient to shield the scattering information from the soil surface, thus, vegetation is usually considered to be the most important factor that affects the retrieval accuracy of soil moisture (Srivastava et al., 2009).When the wavelength is long (e.g. L-band), the influence of the vegetation on backscattering signals becomes weak (Baghdadi et al., 2006). Short wavelengths (e.g. X-band, 3 cm) reflect information from the vegetation canopy, while long wavelengths (e.g. L-band, 24 cm) can penetrate the canopy and obtain echo signals reflected from the soil surface. Medium wavelengths (e.g. C-band, 6 cm) reflect both from the soil and the vegetation canopy. Brown et al. (1988) have found that the C-band can also penetrate vegetation when the vegetation water content is not high. For optimum soil moisture inversion, Ulaby et al. (1982) have recommended that a low incidence angle with a long-wave band (L-band) can minimize the effects from surface roughness and vegetation

The surface roughness (root mean square height *s*, correlation length *l* and autocorrelation function of statistical expression) is another important factor. Parameter sensitivity studies on radar signals from a variety of soil surfaces indicate that the contribution of surface roughness to the radar signal is equivalent or even larger than that of soil moisture (Lin et al., 1994). Therefore, one of the most challenging tasks in active microwave remote sensing of soil moisture is to decouple the effects of soil moisture and surface roughness. Ulaby and Batlivala (1976) have found that when the incident angle is greater than 60°, the echo signals received by the sensor will increase with the same soil surface roughness. In addition, the surface roughness is difficult to measure, and the measurement of large areas is also difficult and expensive. Rahman et al. (2008) put forward the most commonly used soil roughness measurement tool: needle cross-sectional plate, what also finds it hard to describe surface roughness accurately. Subsurface rock fragments also have some impact on the backscatter coefficient, but they cannot be measured (Jackson, 1993). Due to the strong coupling of soil moisture and surface roughness, many researchers are working on the optimal radar configuration for soil moisture retrieval. Rao et al. (1993) found that multi-frequency radar data is more suitable for soil moisture estimation than single-frequency radar data. Srivastava et al. (2009) and Baghdadi et al. (2006) found that combining the low and high incident angle of SAR data (C-band) can get better results in inversion of soil moisture than using a single incidence angle.

Holah et al. (2005) claim that a low incident angle (20°-37°) is more suitable for soil moisture retrieval. The vertical (VV) polarization has the highest sensitivity to soil moisture, followed by horizontal (HH) polarization, while cross (HV and VH) polarization is relatively insensitive to soil moisture. Chen et al. (2005) found that the use of the polarization ratio can minimize the effect of roughness. Theoretically, the multi-polarization method can improve retrieval accuracy. However, some studies have shown a contrary result. For example, Baghdadi et al. (2006) found that the retrieval accuracy of soil moisture is not improved by using the dual polarization (HH / HV) compared to using a single polarization. In the past thirty years, many models have been developed which can quantitatively describe the relationship between the scattering coefficient and soil moisture. The most commonly used surface scattering models are divided into three categories: theoretical models, semi-empirical models, and empirical models. The theoretical models mainly include the Kirchhoff model (e.g. physical optics model and geometrical optics model as well as a small perturbation model), the integral equation model, and the improved advanced integral equation model. The empirical and semi-empirical models mainly include the Oh, Dubois and Shi models. Empirical and semi-empirical models may not be applicable for data sets other than those used in their development. Due to its complexity and the requirement of a detailed knowledge of the surface roughness, it is difficult to invert soil moisture directly using the theoretical models. However, they can be used to predict accurately the scattering returns for a variety of surface profiles, which is very helpful for understanding the surface scattering mechanism.

1.5 Flow chart and outline of the dissertation research

1.5.1 The flow chart of the dissertation research

In this dissertation research, firstly I validated the AIEM model, which was adopted as our working model. The validation was made by extensive comparison with numerical simulations and experimental measurements. Results showed that AIEM predictions matched well with both the numerical simulations and experimental data. With the confirmed confidence, we conducted sensitivity analysis of radar scattering to soil moisture and surface roughness by using the AIEM. First, we investigated the bistatic radar response of soil moisture and surface roughness of bare soil surfaces. To better explore the potential of bistatic scattering for soil moisture sensing, we investigated the sensitivity of single polarized scattering, the combination of dual polarized scattering, and the combination of dual angular scattering, to soil moisture and surface roughness, respectively. Then, the AIEM model was again used to simulate the radar backscattering characteristics of the soil surface. A recurrent Kalman filter-based neural network method was developed to retrieve soil moisture without any auxiliary data. Finally, we selected a bare soil region to test our method. After applying the developed inversion method by using the two ALOS-2 data, we obtained the relative soil moisture change of the research area. A flow chart of the dissertation research is shown below.

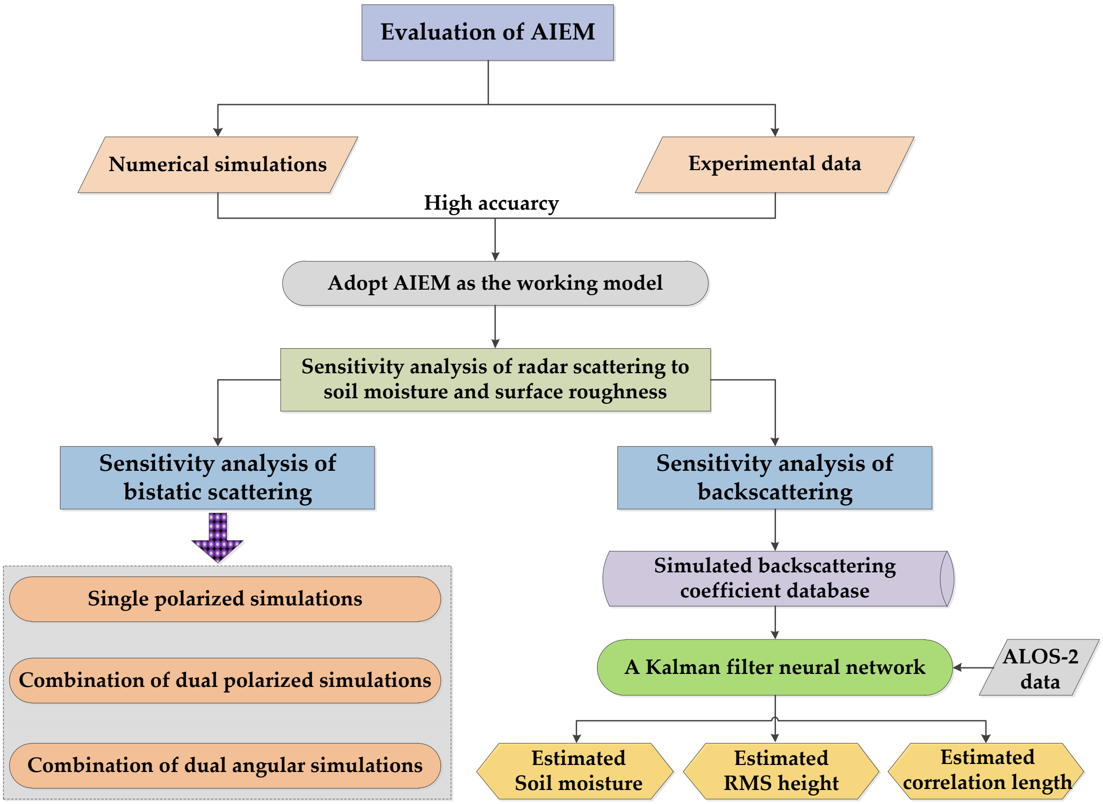

Figure 1.1 Flow chart of the dissertation research.

1.5.2 Outline of the dissertation research

This dissertation focuses on the retrieval of surface soil moisture from radar measurements. The organization of this dissertation is as follows. Chapter 1 introduces the research background and motivation, and gives a brief history of soil moisture remote sensing using radar. Chapter 2 describes the principles of microwave remote sensing of soil moisture. A description of the randomly rough surface is presented, followed by the electromagnetic wave interactions with the media. In particular, an advanced integral equation model (AIEM) is introduced. Chapter 3 elucidates the validity of the AIEM model by extensive comparison with numerical simulations and experimental data. Chapter 4 analyses the characteristics of the bistatic radar configurations and dissects the sensitivity of bistatic scattering to soil moisture and surface roughness of soil surfaces. Chapter 5 presents a framework of soil moisture retrieval from radar measurements using a recurrent Kalman filter-based neural network. The network training and data inversion are described in detail. Chapter 6 concludes the research results and suggests related topics worth future study.

Chapter 2 Electromagnetic wave scattering from rough surfaces

Electromagnetic wave scattering from a randomly rough surface is of palpable importance in many fields of disciplines and bears itself in various applications spanning from surface treatment to remote sensing of terrain and sea (Fung, 1994; Fung and Chen, 2009; Spizzichino and Beckman, 1963; Tsang and Kong, 2001; Ulaby et al., 1982; Voronovich, 1994). For example, in microwave remote sensing of terrain, it has been a common practice to retrieve, by analysing the sensitivity of the scattering behaviour and mechanisms, the geophysical parameters of interest from the scattering and/or emission measurements (Chen et al., 2015; Johnson and Ouellette, 2014). Another example is that by knowing the backscattering patterns, one may be able to detect the presence of the undesired random roughness of a reflective surface such as antenna reflector and, thus, accordingly devise a means to correct or to compensate the phase errors with respect to the phase centre. Therefore, it has been important both theoretically and practically to study the electromagnetic wave scattering from the random surfaces.

In order to tackle the complex and sometimes intricate mathematical derivations and yet to retain a high level of accuracy beyond conventional models [notably, Kirchhoff and small perturbation method (SPM)], the integral equation model (IEM) has been developed by (Chen et al., 1992; Fung, 1994; Fung et al., 1992) under certain physical-justified assumptions. One among these assumptions was to use a simplified Green’s function by dropping off the phase term associated with the random surface height. Doing so might have a more profoundly critical impact among all of these assumptions: While greatly alleviating the burden of mathematical derivations, it unavoidably degrades the model accuracy to a certain extent, depending upon the surface properties and observation geometry. Nevertheless, the IEM model proves to perform very well in backscattering and offers to seamlessly bridge the gap between the Kirchhoff and SPM models. Driven by the need of predicting bistatic scattering and microwave emissivity, much effort has been devoted to further improving IEM accuracy (Chen et al., 2000, 2003; Du, 2008; Fung et al., 2002; Fung and Chen, 2004; Li et al., 2002; Li and Fung, 1991; Wu et al., 2001, 2008; Wu and Chen, 2004;) by removing some of the assumptions that were imposed for the purposes of mathematical simplicity during the course of derivation. This has been done by re-deriving the expressions, though this required excessive and tedious manipulations. Another step forward was the introduction of a transition function into the Fresnel reflection coefficients to take spatial dependencies into account, removing the restrictions on the limits of surface roughness and permittivity (Fung, 1994; Fung et al., 2002). The improved and updated IEM model, called Advanced IEM (AIEM) has proven to work perfectly for a broad range of surface dielectric and geometric parameters (Fung and Chen, 2009, 2004; Fung et al., 2002).

2.1. Description of randomly rough surfaces

The reflection of electromagnetic waves from a planar interface between two media, as matter of fact, is well known via reflection law and Snell’s law. The reflected wave, being specularly directed, is dependent on the incident wavelength, incident angle, and electrical properties of the media. Waves from a rough surface are much more complicated in the sense that the reflected energy is distributed in all directions (though some favour certain directions more than others): its directional pattern is determined by the properties of the rough surface. The roughness of the surface can be characterized as periodically, randomly or quasi-periodically randomly rough. For natural surfaces, however, periodically rough surfaces are most often encountered.

A good example of a quasi-periodically randomly rough surface is a surface formed by wind erosion, saltation of snow particles, and deposition of surface (known as a Sastrugi surface) which is frequently found in polar regions. Wind-blown grubby sand dunes, which cover a vast area on Earth, present yet another interesting surface in view of electromagnetic wave scattering. Mathematically, the Sastrugi surface may be given as a superposition of “ridges and grooves”:

$$z = z(x, y) = \sum_{m=-\infty}^{\infty} \sum_{n=-\infty}^{\infty} a_m \zeta(x - x_m, y - y_n) \tag{2.1}$$

where the amplitude coefficient a_m is assumed to have a uniform random distribution in $[h_0(1 \pm 5\%)]$ with mean height h_0. The position (x_m, y_n) may be assumed to have a Poisson random distribution and is determined by the ridge density (number of ridges per unit length). Notice in particular that for purposes of simulation, the total surface length is of finite L in both directions. The “ridge” function $\zeta(x,y)$ can be of the form:

$$\zeta(x,y) = \rho(x)\mathrm{rect}(x/\ell_x)\mathrm{rect}(y/\ell_y) \tag{2.2}$$

where $\rho(\cdot)$ is the shape function that specifies the ridges’ shape, $\mathrm{rect}(\cdot)$ is the rectangular function, and ℓ_x, ℓ_y defines the width and length of the ridge, respectively.

Other classes of naturally occurring surfaces, such as terrain and sea, are best and, perhaps, only can be modelled by random processes. The two classical approaches commonly used to model natural surfaces, fractal and statistical approaches, are here treated.

2.1.1 Fractal approach

It has been proved that fractal geometry provides a sound and reliable description of natural surfaces (Li et al., 1994; Xu et al., 2010, 2012). However, in order to apply fractal geometry to remote sensing, it is mandatory to devise a fractal model for the surface that allows for a possibly approximate evaluation of the scattered electromagnetic field. A viable fractal model for surface description is the fractional Brownian motion (fBm) model. By definition, an isotropic surface z(x,y) belongs to the class of fBm if:

$$P\{z(x,y) - z(x',y') < \bar{\xi}\} = \frac{1}{\sqrt{2\pi}T^{(1-H)}\tau^H} \int_{-\infty}^{\bar{\xi}} \exp\{-\frac{\xi^2}{2T^{2(1-H)}\tau^{2H}} d\xi \tag{2.3}$$

where *H* is the Hurst coefficient, *T* is the topothesy.

$$\tau = \sqrt{(x-x')^2 + (y-y')^2} \quad . \tag{2.4}$$

Hence, an fBm surface is characterized by stationary Gaussian distributed height increments, while the surface is not stationary. Its description relies on only the two parameters, *H* and *T*. Incidentally, we note that different choices can be made for the set of parameters representing the fBm surface (Li et al., 1994; Xu et al., 2010, 2012). For instance, the fractal dimension *D* and the standard deviation *s* of the height increments at unitary displacement can be used without any restriction on the following analysis. In fact, *D* and *s* are related to *H* and *T* such that:

$$\begin{array}{l} D = 3 - H \\ s = T^{(1-H)} \end{array} \quad . \tag{2.5}$$

Once the surface has been described by means of an fBm random process, it is not straightforward to obtain the corresponding evaluation of the scattered field. This is because fulfilment of the model hypotheses (Agnon and Stiassnie, 1991; Ewe et al., 2001; Franceschetti et al., 1999; Macelloni et al., 2000), mathematical developments (Agnon and Stiassnie, 1991; Ewe et al., 2001; Franceschetti et al., 1999; Macelloni et al., 2000), limits of validity (Agnon and Stiassnie, 1991; Franceschetti et al., 1999; Macelloni et al., 2000), and related issues need to be addressed. In particular, we stress that a surface satisfying Eq. (2.3) for any small value of the distance t would be not differentiable in any point, and its root mean square (RMS) slope would be infinite. On the other hand, a surface satisfying Eq. (2.3) for any large value of the distance τ would suffer from the infinite variance problem (infrared catastrophe). Fortunately, real natural surfaces satisfy Eq. (2.3) only in a limited (although wide) range of t values (or, equivalently, of spatial frequencies). In addition, whenever a scattering problem is in order, the range of distances t to be considered is limited on one side by the illuminated patch size (pixel size), and on the other by the incident electromagnetic wavelength l (values of t much smaller than l need not be considered). Therefore, band limited fBm surfaces must be used (Agnon and Stiassnie, 1991; Ewe et al., 2001; Franceschetti et al., 1999; Li et al., 2002; Macelloni et al., 2000; Wu et al., 2008), and hence lower and upper cut-off frequencies must be introduced. Limits of validity of scattering models obviously depend on such cut-off frequencies (Agnon and Stiassnie, 1991; Franceschetti et al., 1999). However, we here want to stress again that these latter parameters are often not related to surface properties, but rather to illumination (illuminated patch size, wavelength), and therefore they are known a priori.

An example of a fractal random surface is illustrated below.

$$z(x,y) = \sigma \mathrm{C} \sum_{n=0}^{N_f-1} b^{(s-2)} \sin[K_0 b^n (x \cos\beta_n + y \sin\beta_n) + \alpha_n]; \quad b > 1{,}1 < s < 2 \tag{2.6}$$

where z is a band-limited generalized Weierstrass surface with fractal dimension $D=s+1$;

K_0 : is a fundamental wave number;

C : is a normalized coefficient such that z has an RMS height σ such that:

$$C = \left[\frac{2(1-b^{2(s-2)})}{1-b^{2N_f(s-2)}} \right]^{1/2} \quad ; \tag{2.7}$$

α_n: is a random phase uniformly distributed over $[-\pi,\pi]$ and independent of β_n; and

β_n: is a random phase with mean $\overline{\beta}_n$ and some kind of distribution depending on what type of rough surfaces.

The autocovariance function is:

$$\mathfrak{C}_z(\xi,\zeta) = \mathrm{E}\left\{ \frac{\sigma^2 \mathrm{C}^2}{2} \sum_{n=0}^{N_f-1} b^{2(s-2)n} \cos K_n (\xi \cos\beta_n + \zeta \sin\beta_n) \right\} \tag{2.8}$$

where E (.) = expectation operator and $K_n = K_0 b^n$.

After some mathematical manipulation, we arrive at

$$\mathfrak{C}_z(\rho,\phi) = \pi\sigma^2 \mathrm{C}^2 \sum_{n=0}^{N_f-1} b^{2(s-2)n} \sum_{=-\infty}^{\infty} J_m(K_n \rho) S(m) e^{jm(\phi+\pi/2-\overline{\beta}_n} \tag{2.9}$$

where $$S(m) = \frac{1}{2\pi} \int_{-\pi}^{\pi} P_n(\psi_n) e^{-jm\psi_n} \, d\psi_n \tag{2.10}$$

and $J_m(\cdot)$ is the Bessel function of order *m*.

By noting $J_m(K_n\rho) = (-1)^m J_{-m}(K_n\rho)$, we may rewrite $\mathfrak{C}$ as:

$$\begin{aligned}\mathfrak{C}_z(\rho,\phi) = \pi\sigma^2\mathrm{C}^2 \Bigg\{ &\sum_{n=0}^{N_f-1} \frac{b^{2(s-2)n}}{2} J_0(K_n\rho) \\ &+ \sum_{n=0}^{N_f-1} b^{2(s-2)n} \sum_{m=1}^{\infty} (-1)^m J_{2m}(K_n\rho) S(2m) \cos 2m(\phi - \overline{\beta}_n \Bigg\}\end{aligned} \tag{2.11}$$

By considering the finite antenna beam-width, a Gaussian beam of the form $e^{-1/2(\rho/R_n)^2}$ is introduced to account for finite footprint, where $R_n = \varepsilon\Lambda_n; \varepsilon > 0$ and $\Lambda_n = \frac{2\pi}{K_n}$.

Therefore,

$$\begin{aligned}\mathfrak{C}_z(\rho,\phi) = \pi\sigma^2\mathrm{C}^2 \Bigg\{ &\sum_{n=0}^{N_f-1} \frac{b^{2(s-2)n}}{2} e^{-\rho^2/2R_n^2} J_0(K_n\rho) \\ &+ \sum_{n=0}^{N_f-1} b^{2(s-2)n} e^{-\rho^2/2R_n^2} \sum_{m=1}^{\infty} (-1)^m J_{2m}(K_n\rho) S(2m) \cos 2m(\phi - \overline{\beta}_n) \Bigg\}\end{aligned} . \tag{2.12}$$

The corresponding roughness spectra is:

$$\begin{aligned} W(K,\Phi) &= \frac{1}{2\pi} \int_0^{\infty} \int_0^{2\pi} \rho \mathfrak{C}_z(\rho,\phi) e^{-jK\rho\cos(\phi-\Phi)} d\phi d\rho \\ &= \frac{\sigma^2\mathrm{C}^2}{2} \Bigg\{ \sum_{n=0}^{N_f-1} \frac{b^{2(s-2)n}}{2} R_n^2 e^{-\frac{R_n^2(K_n^2+K^2)}{2}} I_0(R_n^2 K_n K) + \\ &\qquad \sum_{n=0}^{N_f-1} 4\pi b^{2(s-2)n} R_n^2 e^{-\frac{R_n^2(K_n^2+K^2)}{2}} \sum_{m=1}^{\infty} S(2m) \cos[2m(\Phi - \overline{\beta}_n) I_{2m}(R_n^2 K_n K) \Bigg\} \end{aligned} \tag{2.13}$$

where $I_n(\cdot)$ is a modified Bessel function of order *e*.

For sea surfaces, one possible choice of the random phase is

$\overline{\beta}_n$ = mean wind direction, and

$\psi_n = \beta_n - \overline{\beta}_n$ with probability density function

$$P(\psi_n) = g_n \left| \cos\frac{\psi_n}{2} \right|^{2e_n} \mathrm{rect}\left[\frac{\psi_n}{2\pi} \right] \tag{2.14}$$

with

$$g_n = \frac{2^{2e_n - 1}\Gamma^2(1+e_n)}{\pi\Gamma(1+2e_n)}\;;\quad e_n = \left(\frac{n_T+1}{n+1}\right)^{1/2}\;;\quad n_T = Int\left\{\frac{\ln(K_T / K_0)}{\ln(b)}\right\}$$; and

$K_T = \sqrt{\frac{g\rho_w}{\tau_s}}$ =3.63 rad/cm

where

g: gravitational acceleration=981 cm/ s^2 ;

ρ_w: water density; and

τ_s: surface tension.

2.1.2 $\sigma - \ell$ approach

Though fractal properties were investigated in the context of describing a random surface, we adopted more classical, and more commonly used, roughness parameters: the correlation length and the RMS height. The correlation length measures the horizontal roughness scale. The RMS height describes the vertical roughness scale. The ratio of RMS height to correlation length is related to surface RMS slope.

Assuming a randomly rough surface $z(x,y)$ and a real stationary process with zero mean and standard deviation σ, then

$$\left\langle z(x,y)z(x+\tau_x, y+\tau_y\right\rangle = \sigma^2\rho(\tau_x,\tau_y) \tag{2.15}$$

where $\sigma^2 = \left\langle z^2\right\rangle - \left\langle z\right\rangle^2$ and z follows a Gaussian distribution such that:

$$p(z) = \frac{1}{\sqrt{2\pi}\sigma}e^{-z^2/2\sigma^2} \quad . \tag{2.16}$$

For an isotropic surface, we have $\tau_x = \tau_y = \tau$. In what follows, the isotropic surface is treated unless otherwise specified.

For the surface scattering problem, the joint probability density function between two points on the surface is of interest, and is:

$$p(z,z') = \frac{\exp\{-(z^2 - \rho zz' + z'^2) / (2\sigma^2(1-\rho^2)\}}{2\pi\sigma^2\sqrt{1-\rho^2}} \quad . \tag{2.17}$$

The correlation function $\rho(\tau_x, \tau_y) \leftrightarrow \rho(\tau, \phi)$ appearing in Esq. (2.15) and (2.17) is defined by:

$$\rho(\tau) = \lim_{L\to\infty} \frac{1}{L} \int_0^{L-\tau} z(r)z(r+\tau)\,dr \tag{2.18}$$

where $r = \sqrt{x^2 + y^2}$; and L is the surface length.

The surface spectrum and correlation function are related by the Wiener-Khintchine Theorem, which states that the spectrum of a wide-sense stationary random process of zero mean and its autocorrelation function form a Fourier transform pair:

$$W(k,\varphi) = \int_0^{2\pi} \int_0^{\infty} \rho(\tau,\phi) e^{jk\tau\cos(\varphi-\phi)} \tau\, d\tau\, d\phi \quad . \tag{2.19}$$

For an isotropic surface, the autocorrelation function $\rho(\tau, \phi)$ is independent of direction ϕ and dependent only on lag distance τ. The relation reduces to:

$$W(K) = \int_0^{\infty} \rho(r) J_0(Kr) r\, dr \tag{2.20}$$

where J_0 is zeroth order Bessel function.

In reality, surface length L is finite, leading to a cut-off spectrum given by:

$$W_m(K) = \begin{cases} 0 & , \quad 0 \le K < 2\pi / L \\ K_n / K^n & , \quad 2\pi / L < K < \infty \end{cases} \tag{2.21}$$

where K_n is defined similar to that of Eq. (2.8). The corresponding measured height variance and correlation length are, respectively, calculated by the following equations:

$$\begin{aligned} \sigma_m^2 &= \frac{K_n L^{n-1}}{n-1} \\ \ell_m &= \frac{(n-1)^2 L}{2(2n-1)} \end{aligned} \tag{2.22}$$

For simplicity, but without loss of generality, we have only discussed the isotropic surface. Note that for an isotropic surface, $\rho(\tau,\phi)=\rho(\tau)$. In general, the correlation length ℓ is directionally dependent for anisotropic surfaces such as the sea. When the correlation function drops from 1 (the maximum value) to e^{-1}, the corresponding value of τ is called the correlation length ℓ, that is $\rho(\ell)=e^{-1}$. Fig. 2.1 illustrates the correlation function as a function of lag distance τ. The standard deviation and correlation length are called the intrinsic surface parameters under the $\sigma-\ell$ model.

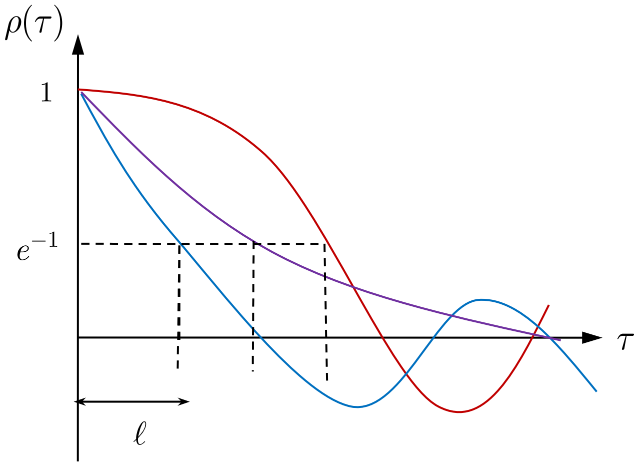

Figure 2.1 Correlation function and correlation length *l*.

2.2 Surface spectrum and correlation function

This subsection gives commonly used surface correlation functions and their surface spectra. For natural surfaces, because of their formation mechanisms, a distinct correlation function may be presented that best describes its correlation properties. The following pairs of equations illustrate three commonly used functions: Gaussian, Lorentzian (better known as Exponential), and Exponential-like.

Gaussian function

$$\rho(r)=e^{-r^2/\ell^2} \tag{2.23a}$$

$$W(K)=\frac{\ell}{\pi}e^{-K^2\ell^2/2} \tag{2.23b}$$

Lorentzian (Exponential) function

$$\rho(r) = e^{-|r|/\ell}; \tag{2.24a}$$

$$W(K) = \frac{1}{\pi\ell(1+K^2\ell^2)} \tag{2.24b}$$

1.5-Power

$$\rho(r) = \frac{1}{[1+(r\,/\,\ell)^2]^{1.5}} \tag{2.25a}$$

$$W(K) = \frac{\sqrt{K\ell}J_{0.5}(K\ell)}{2^{1.5}\pi\Gamma(1.5)} \tag{2.25b}$$

Exponential-like function

$$\rho(r) = \exp[-r(1-e^{-r/x})\,/\,L] \tag{2.26a}$$

$$W^{(n)}(K) = \sum_{m=0}^{\infty}\left(\frac{L_e}{L}\right)^m \frac{{L_e}^2}{m!}\Gamma(m+2)\,{}_2F_1(\frac{2+m}{2},\frac{3+m}{2},1,-KL_e) \tag{2.26b}$$

where $L_e = (xL)\,/\,(x+mL)$, ${}_2F_1(a,b,c;z)$ is the hypergeometric function, and $L \geq x$.

To achieve a clear separation between a Gaussian shape around the origin and an Exponential elsewhere, it is necessary to choose $L >> x$. When x is small, the correlation length will be approximately equal to *L*. The transition region from Exponential to Gaussian is proportional to the x value, which controls the actual shape of the correlation function.

2.3 Roughness parameters

In the statistical sense, $\mathbf{y} = \{\sigma,\ell\}$ is a random variable due to spatially and temporally varying properties such that

$$\mathbf{y} = \mathbf{y}_t + \mathbf{y}_n \tag{2.27}$$

where $\mathbf{y}_t$ is "truth", and $\mathbf{y}_n$ is an error term.

In practice, the “truth” is never obtainable, nor measurable. Statistically, $\mathbf{y}_t$ and $\mathbf{y}_n$ may be assumed to be, as they usually are, uncorrelated, such that $\mathbf{y}$ is an unbiased estimate of $\mathbf{y}_t$, i.e.:

$$\mathrm{E}(\mathbf{y}) = \mathrm{E}(\mathbf{y}_t), \forall \mathbf{y}_n \sim \mathscr{N}(0, \sigma^2_{\mathbf{y}_n}) \tag{2.28}$$

where E denotes statistical mean, and $\sigma^2_{\mathbf{y}_n}$ is the variance of $\mathbf{y}_n$.

It turns out that to estimate the correlation length, we need to know the correlation function ρ. For natural surfaces, the RMS height and the correlation length typically depend on the measured length.

The variance of estimate correlation function $\hat{\rho}$ is:

$$\mathrm{var}[\hat{\rho}(\zeta)] = \frac{1}{L_s}\int_0^\infty [\rho^2(\xi) + \rho(\xi-\zeta)\rho(\xi+\zeta) - 4\rho(\zeta)\rho(\xi)\rho(\xi+\zeta) + 2\rho^2(\xi)\rho^2(\zeta)]d\xi \tag{2.29}$$

where L_s is the profile length used to estimate ρ.

The variance of estimate RMS height σ is:

$$var(\hat{\sigma}) = \frac{\sigma^2}{L_s}\int_0^\infty \rho^2(\xi)\, d\xi \quad . \tag{2.30}$$

It is evident that both variances are strongly dependent on the shape of the correlation function. The RMS height and correlation length increase with the measurement trace length.

2.4 Electromagnetic wave-media interactions

2.4.1 Electric field integral equation (EFIE) and magnetic field integral equation (MFIE)

Referring to Fig. 2.2, considering a plane wave impinges onto a dielectric rough surface which scatters waves up into the incident plane and down into the lower medium, with the electric and magnetic fields been written as:

$$\vec{E}^i = \hat{p}E_0 \exp\left[-j\left(\vec{k}_i \cdot \vec{r}\right)\right] \tag{2.31a}$$

$$\vec{H}^i = \frac{1}{\eta}\hat{k}_i \times \vec{E}^i \tag{2.31b}$$

where $j = \sqrt{-1}$; i denotes the incident wave; $\hat{p}$is the unit polarization vector; E_0 is the amplitude of the incident electric field, and η is the intrinsic impedance of the upper medium, respectively. The position vector is $\vec{r} = x\hat{x} + y\hat{y} + z\hat{z}$ and the wavenumber vectors in the incident and scattering directions are defined as follows, respectively:

$$\vec{k}_i = k\hat{k}_i = \hat{x}k_{ix} + \hat{y}k_{iy} + \hat{z}k_{iz}; k_{ix} = k\sin\theta_i\cos\phi_i, k_{iy} = k\sin\theta_i\sin\phi_i, k_{iz} = k\cos\theta_i \quad ; \tag{2.32a}$$

e $$\vec{k}_s = k\hat{k}_s = \hat{x}k_{sx} + \hat{y}k_{sy} + \hat{z}k_{sz}; k_{sx} = k\sin\theta_s\cos\phi_s, k_{sy} = k\sin\theta_s\sin\phi_s, k_{sz} = k\cos\theta_s \quad . \tag{2.32b}$$

For linearly polarized horizontally polarized and vertically polarized waves, the polarization vector $\hat{p}$ for incident (*i*) and scattering (*s*) waves, respectively, is defined as:

$$\begin{aligned} \hat{h}_i &= -\hat{x}\sin\phi_i + \hat{y}\cos\phi_i \\ \hat{v}_i &= \hat{h}_i \times \hat{k}_i = -(\hat{x}\cos\theta_i\cos\phi_i + \hat{y}\cos\theta_i\sin\phi_i + \hat{z}\sin\theta_i) \\ \hat{h}_s &= \hat{\phi} = -\hat{x}\sin\phi_s + \hat{y}\cos\phi_s \\ \hat{v}_s &= \hat{\theta} = \hat{h}_s \times \hat{k}_s = \hat{x}\cos\theta_s\cos\phi_s + \hat{y}\cos\theta_s\sin\phi_s - \hat{z}\sin\theta_s \end{aligned} \quad . \tag{2.33}$$

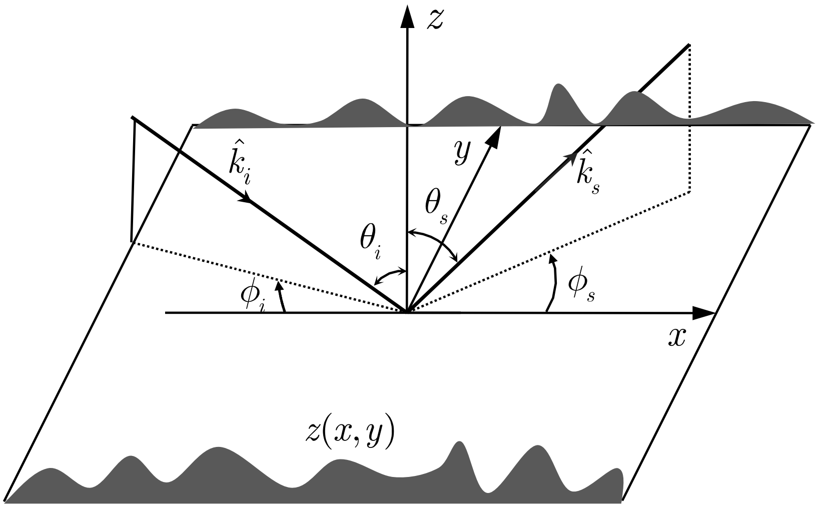

Figure 2.2 Wave scattering geometry

The total electric and magnetic fields according to the Stratton-Chu Formula may be expressed (Ulaby et al., 1982; Tsang and Kong, 2001) as:

$$\vec{E}(\vec{r}) = \oiint_{S'} dS'\left\{ i\omega\mu[\hat{n} \times \vec{H}(\vec{r}\,')]G(\vec{r},\vec{r}\,') + [\hat{n} \cdot \vec{E}(r')]\nabla' G(\vec{r},\vec{r}\,') + [\hat{n} \times \vec{E}(r')] \times \nabla' G(\vec{r},\vec{r}\,') \right\} \tag{2.34a}$$

$$\vec{H}(\vec{r}) = \oiint_{S'} dS'\left\{ -i\omega\varepsilon[\hat{n} \times \vec{E}(\vec{r}\,')]G(\vec{r},\vec{r}\,') + [\hat{n} \cdot \vec{H}(r')]\nabla' G(\vec{r},\vec{r}\,') + [\hat{n} \times \vec{H}(r')] \times \nabla' G(\vec{r},\vec{r}\,') \right\} \tag{2.34b}$$

where G is Green's function, $\hat{n}$ is the unit normal vector pointing to the scattering region, and the integration is performed over the rough surface S'.

The total field is the sum of the incident field, which is known, and the scattered field, which is unknown and is to be determined. For a source-free region as in our case, it is expressed mathematically (Ewe et al., 2001) as:

$$\vec{E}(\vec{r}) = \Upsilon \vec{E}_i(\vec{r}) - \frac{\Upsilon}{4\pi} \oiint dS'\left\{ i\omega\mu[\hat{n} \times \vec{H}]G - [\hat{n} \times \vec{E}] \times \nabla' G - [\hat{n} \cdot \vec{E}]\nabla' G \right\} \tag{2.35a}$$

$$\vec{H}(\vec{r}) = \Upsilon \vec{H}_i(\vec{r}) + \frac{\Upsilon}{4\pi} \oiint dS'\left\{ i\omega\varepsilon[\hat{n} \times \vec{E}]G + [\hat{n} \times \vec{H}] \times \nabla' G + [\hat{n} \cdot \vec{H}]\nabla' G \right\} \tag{2.35b}$$

where $\Upsilon = (1 - \Omega / 4\pi)^{-1}, \Omega = \begin{cases} 0, \vec{r} \notin S' \\ 2\pi, \vec{r} \in S' \end{cases}$.

2.4.2 Far-zone scattered field and scattering coefficients

Equation (2.34) states the Huygens' Principle (Tsang and Kong., 2001): The field solution in a given volume V' is completely determined by the tangential fields specified over the surface S' enclosing V'. From Eq. (2.35), to find the surface fields one has to solve the pair of Fredholm integral equations of the second kind. For a rough surface with an irregular boundary, the completely analytic solution is almost prohibitive. Instead, an approximate estimate of the surface tangential fields is usually, and preferably, adopted by taking the vector product with the unit surface normal on both sides of Equations (2.35a) and (2.35b) and, after some reformulations (Macelloni et al., 2000), by using an iterative scheme to find the estimates.

Once the surface tangential field estimates are made available, the scattered field for q polarization at far-zone distance R is readily calculated by making use of the Stratton-Chu formula (see Fig. 2):

$$E_{qp}^{s} = \mathbb{C} E_0 \int [\hat{q} \times \hat{k}_s \cdot (\hat{n} \times \vec{E}_p) + \eta \hat{q} \cdot (\hat{n} \times \vec{H}_p)] \exp[j(k\hat{k}_s \cdot \vec{r})] dS \tag{2.36}$$

where $\mathbb{C} = -\dfrac{jk_i}{4\pi R} \exp(-jk_i R)$.

Once the scattered field is solved, the scattering coefficient with q polarization is calculated as (Ulaby et al., 1982):

$$\sigma_{qp}^{o} = \frac{4\pi R^2 \mathfrak{Re}\left\{\left\langle \left|E_{qp}^{s}\right|^2 \right\rangle\right\}}{A_0 \cos\theta_i \mathfrak{Re}\left\{\left|E_i\right|^2\right\}} \tag{2.37}$$

where R is the range from surface to observation point and A_0 is the illuminated area of overlap, confined by transmitting and receiving antenna beam patterns over the surface.

2.5 The advanced IEM model

In IEM and AIEM modelling (Fung, 1994; Fung et al., 1992), the estimation of surface fields is the sum of the Kirchhoff field and the complementary field, or:

$$(\hat{n} \times \vec{E}_p) = (\hat{n} \times \vec{E}_p)_k + (\hat{n} \times \vec{E}_p)_c \tag{2.38a}$$

$$(\hat{n} \times H_p) = (\hat{n} \times \vec{H}_p)_k + (\hat{n} \times \vec{H}_p)_c \tag{2.38b}$$

where the Kirchhoff fields can be expressed as:

$$(\hat{n}\times\vec{E}_p)_k = \hat{n}\times[(1-R_v)\hat{p}+(R_v+R_h)(\hat{p}\cdot\hat{t})\hat{t}]E^i \tag{2.39a}$$

$$\eta_1(\hat{n}\times\vec{H}_p)_k = \hat{n}\times\hat{k}_i\times[(1+R_v)\hat{p}+(R_v+R_h)(\hat{p}\cdot\hat{t})\hat{t}]E^i \tag{2.39b}$$

and the complementary surface fields, which correct the Kirchhoff estimates, are written as:

$$\begin{aligned}(\hat{n}\times\vec{E}_v)_c = -\frac{1}{4\pi}[\hat{n}\times\int(1-R_v)\vec{\mathscr{E}}_v ds' + \hat{n}\times\int(1+R_v)\vec{\mathscr{E}}_{vt} ds' \\ -(R_v+R_h)(\hat{n}\times\hat{t})(\hat{n}\times\hat{t})\cdot\hat{n}\times\int(\vec{\mathscr{E}}_v-\vec{\mathscr{E}}_{vt})ds' \quad]\end{aligned} \tag{2.40a}$$

$$\begin{aligned}(\hat{n}\times\vec{E}_h)_c = -\frac{1}{4\pi}[\hat{n}\times\int(1+R_h)\vec{\mathscr{E}}_h ds' + \hat{n}\times\int(1-R_h)\vec{\mathscr{E}}_{ht} ds' \\ +(R_v+R_h)\hat{t}\hat{t}\cdot\hat{n}\times\int(\vec{\mathscr{E}}_h-\vec{\mathscr{E}}_{ht})ds' \quad]\end{aligned} \tag{2.40b}$$

$$\begin{aligned}(\hat{n}\times\vec{H}_v)_c = \frac{1}{4\pi}[\hat{n}\times\int(1+R_v)\vec{\mathscr{H}}_v ds' + \hat{n}\times\int(1-R_v)\vec{\mathscr{H}}_{vt} ds' \\ -(R_v+R_h)\hat{t}\hat{t}\cdot\hat{n}\times\int(\vec{\mathscr{H}}_v-\vec{\mathscr{H}}_{vt})ds' \quad]\end{aligned} \tag{2.41a}$$

$$\begin{aligned}(\hat{n}\times\vec{H}_h)_c = \frac{1}{4\pi}[\hat{n}\times\int(1-R_h)\vec{\mathscr{H}}_h ds' + \hat{n}\times\int(1+R_h)\vec{\mathscr{H}}_{ht} ds' \\ +(R_v+R_h)(\hat{n}\times\hat{t})(\hat{n}\times\hat{t})\cdot\hat{n}\times\int(\vec{\mathscr{H}}_h-\vec{\mathscr{H}}_{ht})ds' \quad]\end{aligned} \quad . \tag{2.41b}$$

In the above expressions, we make use of a local coordinate defined by $[\hat{k}_i, \hat{t}, \hat{d}]$ as seen in Fig. 2.3 (Ulaby et al., 1982; Fung, 1994).

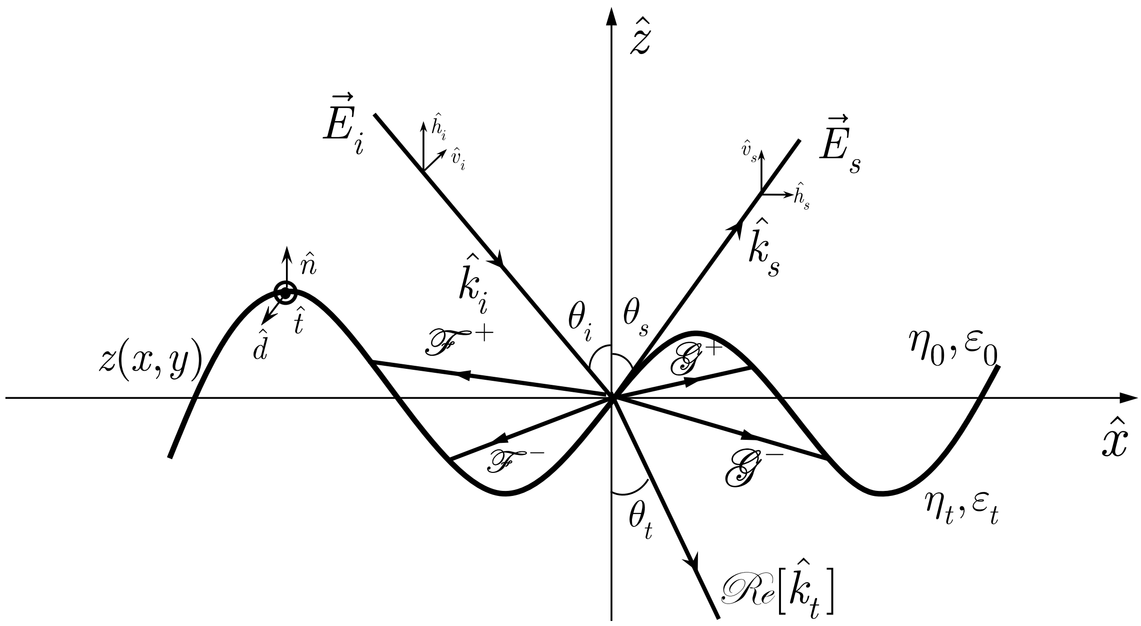

Figure 2.3 Geometry of scattering from a rough surface, where $\mathscr{F}^{\pm}, \mathscr{G}^{\pm}$, respectively, represent the upward re-radiation and downward re-radiation, going through the upper medium and the lower medium.

The unknown electric and magnetic fields that appear inside the integrals above are expressed as:

$$\vec{\mathscr{E}}_p = jk_i\eta(\hat{n} \times \vec{H}_p)G - (\hat{n} \times \vec{E}_p) \times \nabla' G - (\hat{n} \cdot \vec{E}_p)\nabla' G \tag{2.42a}$$

$$\vec{\mathscr{H}}_p = j\frac{k_i}{\eta}(\hat{n} \times \vec{E}_p)G - (\hat{n} \times \vec{H}_p) \times \nabla' G - (\hat{n} \cdot \vec{H}_p)\nabla' G \tag{2.42b}$$

$$\vec{\mathscr{E}}_{pt} = -[jk_t\eta_t(\hat{n} \times \vec{H}_p)G_t - (\hat{n} \times \vec{E}_p) \times \nabla' G_t - \frac{1}{\varepsilon_r}(\hat{n} \cdot \vec{E}_p)\nabla' G_t] \tag{2.43a}$$

$$\vec{\mathscr{H}}_{pt} = -[j\frac{k_t}{\eta_t}(\hat{n} \times \vec{E}_p)G_t - (\hat{n} \times \vec{H}_p) \times \nabla' G_t - \frac{1}{\mu_r}(\hat{n} \cdot \vec{H}_p)\nabla' G_t \tag{2.43b}$$

where η_t is the intrinsic impedance of the lower medium, the wave transmitted region. Note that Eq. (2.42) and (2.43) involve Green's functions G, G_t and their gradients in the upper and lower mediums $\nabla G, \nabla G_t$, respectively.

By substituting the Kirchhoff surface fields in Eq. (2.39a) and (2.39b) into Eq. (2.42) and (2.43), the estimates of the complementary fields of Eq. (2.40) and (2.41) can be obtained. This may be seen as a second iteration of seeking the solution of the integral equations governing the surface fields using Kirchhoff fields as initial guesses, which is indeed a very good choice for fast convergence

Corresponding to the Kirchhoff and the complementary surface fields in Eq (2.39) and (2.40), the far-zone scattered field may be also expressed as a sum of the Kirchhoff and the complementary scattered fields (Fung, 1994; Fung et al., 1992):

$$E_{qp}^{s} = E_{qp}^{k} + E_{qp}^{c} \tag{2.44}$$

where the Kirchhoff field is given by

$$E_{qp}^{k} = \mathbb{C}E_0 \int f_{qp} \exp\{j\Phi\} dxdy \tag{2.45}$$

with the phase term $\Phi = k[(\hat{k}_s - \hat{k}_i) \cdot \vec{r}]$.

The complementary scattered field, propagating upward and downward, may be written as:

$$E_{qp}^{c} = \frac{\mathbb{C}E_0}{8\pi^2} \int \left\{ \boldsymbol{\mathfrak{F}}_{qp} e^{j[\Phi_i + \vec{k}_s \cdot \vec{r} - \vec{k}_i \cdot \vec{r}']} + \boldsymbol{\mathfrak{G}}_{qp} e^{j[\Phi_t + \vec{k}_s \cdot \vec{r} - \vec{k}_i \cdot \vec{r}']} \right\} dudvdxdydx'dy' \quad . \tag{2.46}$$

The Kirchhoff field coefficients f_{qp} appearing in Eq. (2.45) can be explicitly written into the following form:

$$\begin{aligned} f_{vv} &= -[(1 - R_v)\hat{h}_s \cdot (\hat{n} \times \hat{v}_i) + (1 + R_v)\hat{v}_s \cdot (\hat{n} \times \hat{h}_i)]\mathrm{s}_1 \\ &-(R_h + R_v)(\hat{v}_i \cdot \hat{t})[(\hat{h}_s \cdot \hat{d})(\hat{n} \cdot \hat{k}_i) - (\hat{n} \cdot \hat{d})(\hat{h}_s \cdot \hat{k}_i) - (\hat{v}_s \cdot \hat{t})(\hat{n} \cdot \hat{k}_i)]\mathrm{s}_1 \end{aligned} \tag{2.47a}$$

$$\begin{aligned} f_{vh} &= [(1 - R_h)\hat{v}_s \cdot (\hat{n} \times \hat{v}_i) - (1 + R_h)\hat{h}_s \cdot (\hat{n} \times \hat{h}_i)]\mathrm{s}_1 \\ &-(R_h + R_v)(\hat{h}_i \cdot \hat{d})[(\hat{h}_s \cdot \hat{t})(\hat{n} \cdot \hat{k}_i) - (\hat{n} \cdot \hat{d})(\hat{v}_s \cdot \hat{k}_i) + (\hat{v}_s \cdot \hat{d})(\hat{n} \cdot \hat{k}_i)]\mathrm{s}_1 \end{aligned} \tag{2.47b}$$

$$\begin{aligned} f_{hv} &= [(1 - R_v)\hat{v}_s \cdot (\hat{n} \times \hat{v}_i) - (1 + R_v)\hat{h}_s \cdot (\hat{n} \times \hat{h}_i)]\mathrm{s}_1 \\ &-(R_h + R_v)(\hat{v}_i \cdot \hat{t})[(\hat{h}_s \cdot \hat{t})(\hat{n} \cdot \hat{k}_i) - (\hat{n} \cdot \hat{d})(\hat{v}_s \cdot \hat{k}_i) + (\hat{v}_s \cdot \hat{d})(\hat{n} \cdot \hat{k}_i)]\mathrm{s}_1 \end{aligned} \tag{2.47c}$$

$$\begin{aligned} f_{hh} &= [(1 + R_h)\hat{v}_s \cdot (\hat{n} \times \hat{h}_i) + (1 - R_h)\hat{h}_s \cdot (\hat{n} \times \hat{v}_i)]\mathrm{s}_1 \\ &-(R_h + R_v)(\hat{h}_i \cdot \hat{d})[(\hat{h}_s \cdot \hat{d})(\hat{n} \cdot \hat{k}_i) - (\hat{n} \cdot \hat{d})(\hat{h}_s \cdot \hat{k}_i) - (\hat{v}_s \cdot \hat{t})(\hat{n} \cdot \hat{k}_i)]\mathrm{s}_1 \end{aligned} \tag{2.47d}$$

where $\mathrm{s}_1 = \sqrt{1 + z_x^2 + z_y^2}$.

The complementary scattered field is contributed from the re-radiated fields that may propagate through medium 1 and medium 2, represented by upwardly moving and downwardly moving waves. The propagators $\boldsymbol{\mathfrak{F}}_{qp}, \boldsymbol{\mathfrak{G}}_{qp}$ may be decomposed into the upward components designated by $\boldsymbol{\mathfrak{F}}_{qp}^{+}, \boldsymbol{\mathfrak{G}}_{qp}^{+}$ and the downward components designated by $\mathfrak{F}_{qp}^{-}, \mathfrak{G}_{qp}^{-}$, mathematically appearing as the absolute terms in Eq. (2.14), physically denoting the change of propagation velocity at different media. The explicit expressions of the complementary field coefficients are given below:

$$\begin{aligned}\mathfrak{F}_{vv}^{\pm}(u,v) = &-\left(\frac{1-R_v}{\pm q_i}\right)\left(1+R_v\right)\mathrm{C}_1 + \left(\frac{1-R_v}{\pm q_i}\right)\left(1-R_v\right)\mathrm{C}_2 + \left(\frac{1-R_v}{\pm q_i}\right)\left(1+R_v\right)\mathrm{C}_3 \\ &+ \left(\frac{1+R_v}{\pm q_i}\right)\left(1-R_v\right)\mathrm{C}_4 + \left(\frac{1+R_v}{\pm q_i}\right)\left(1+R_v\right)\mathrm{C}_5 + \left(\frac{1+R_v}{\pm q_i}\right)\left(1-R_v\right)\mathrm{C}_6\end{aligned} \tag{2.48a}$$

$$\begin{aligned}\mathfrak{G}_{vv}^{\pm}(u,v) = &\left(\frac{\left(1+R_v\right)\mu_r}{\pm q_t}\right)\left(1+R_v\right)\mathrm{C}_{1t} - \left(\frac{1+R_v}{\pm q_t}\right)\left(1-R_v\right)\mathrm{C}_{2t} - \left(\frac{1+R_v}{\pm q_t\varepsilon_r}\right)\left(1+R_v\right)\mathrm{C}_{3t} \\ &- \left(\frac{\left(1-R_v\right)\varepsilon_r}{\pm q_t}\right)\left(1-R_v\right)\mathrm{C}_{4t} - \left(\frac{1-R_v}{\pm q_t}\right)\left(1+R_v\right)\mathrm{C}_{5t} - \left(\frac{1-R_v}{\pm q_t\mu_r}\right)\left(1-R_v\right)\mathrm{C}_{6t}\end{aligned} \tag{2.48b}$$

$$\begin{aligned}\mathfrak{F}_{hh}^{\pm}(u,v) = &\left(\frac{1-R_h}{\pm q_i}\right)\left(1+R_h\right)\mathrm{C}_1 - \left(\frac{1-R_h}{\pm q_i}\right)\left(1-R_h\right)\mathrm{C}_2 - \left(\frac{1-R_h}{\pm q_i}\right)\left(1+R_h\right)\mathrm{C}_3 \\ &- \left(\frac{1+R_h}{\pm q_i}\right)\left(1-R_h\right)\mathrm{C}_4 - \left(\frac{1+R_h}{\pm q_i}\right)\left(1+R_h\right)\mathrm{C}_5 - \left(\frac{1+R_h}{\pm q_i}\right)\left(1-R_h\right)\mathrm{C}_6\end{aligned} \tag{2.48c}$$

$$\begin{aligned}\mathfrak{G}_{hh}^{\pm}(u,v) = &-\left(\frac{\left(1+R_h\right)\varepsilon_r}{\pm q_t}\right)\left(1+R_h\right)\mathrm{C}_{1t} + \left(\frac{1+R_h}{\pm q_t}\right)\left(1-R_h\right)\mathrm{C}_{2t} - \left(\frac{1+R_h}{\pm q_t\mu_r}\right)\left(1+R_h\right)\mathrm{C}_{3t} \\ &+ \left(\frac{\left(1+R_h\right)\mu_r}{\pm q_t}\right)\left(1-R_h\right)\mathrm{C}_{4t} + \left(\frac{1-R_h}{\pm q_t}\right)\left(1+R_h\right)\mathrm{C}_{5t} - \left(\frac{1-R_h}{\pm q_t\varepsilon_r}\right)\left(1-R_h\right)\mathrm{C}_{6t}\end{aligned} \tag{2.48d}$$

$$\begin{aligned}\mathfrak{F}_{hv}^{\pm}(u,v) = &\left(\frac{1-R}{\pm q_i}\right)\left(1+R\right)\mathrm{B}_1 + \left(\frac{1-R}{\pm q_i}\right)\left(1-R\right)\mathrm{B}_2 - \left(\frac{1-R}{\pm q}\right)\left(1+R\right)\mathrm{B}_3 \\ &+ \left(\frac{1+R}{\pm q_i}\right)\left(1-R\right)\mathrm{B}_4 + \left(\frac{1+R}{\pm q_i}\right)\left(1+R\right)\mathrm{B}_5 - \left(\frac{1+R}{\pm q_i}\right)\left(1-R\right)\mathrm{B}_6\end{aligned} \tag{2.48e}$$

$$\begin{aligned}\mathfrak{G}_{hv}^{\pm}(u,v) = &-\left(\frac{\left(1+R\right)\mu_r}{\pm q_t}\right)\left(1+R\right)\mathrm{B}_{1t} + \left(\frac{1+R}{\pm q_t}\right)\left(1-R\right)\mathrm{B}_{2t} + \left(\frac{1+R}{\pm q_t\varepsilon_r}\right)\left(1+R\right)\mathrm{B}_{3t} \\ &- \left(\frac{\left(1-R\right)\varepsilon_r}{\pm q_t}\right)\left(1-R\right)\mathrm{B}_{4t} + \left(\frac{1-R}{\pm q_t}\right)\left(1+R\right)\mathrm{B}_{5t} + \left(\frac{1-R}{\pm q_t\mu_r}\right)\left(1-R\right)\mathrm{B}_{6t}\end{aligned} \tag{2.48f}$$

$$\begin{aligned}\mathfrak{F}_{vh}^{\pm}(u,v) = &\left(\frac{1+R}{\pm q_i}\right)\left(1-R\right)\mathrm{B}_1 - \left(\frac{1+R}{\pm q_i}\right)\left(1+R\right)\mathrm{B}_2 - \left(\frac{1+R}{\pm q_i}\right)\left(1-R\right)\mathrm{B}_3 \\ &+ \left(\frac{1-R}{\pm q_i}\right)\left(1+R\right)\mathrm{B}_4 + \left(\frac{1-R}{\pm q_i}\right)\left(1-R\right)\mathrm{B}_5 + \left(\frac{1-R}{\pm q_i}\right)\left(1+R\right)\mathrm{B}_6\end{aligned} \tag{2.48g}$$

$$\begin{aligned}\mathfrak{G}_{vh}^{\pm}(u,v) = &-\left(\frac{\left(1-R\right)\varepsilon_r}{\pm q_t}\right)\left(1-R\right)\mathrm{B}_{1t} + \left(\frac{1-R}{\pm q_t}\right)\left(1+R\right)\mathrm{B}_{2t} + \left(\frac{1-R}{\pm q_t \mu_r}\right)\left(1-R\right)\mathrm{B}_{3t} \\ &-\left(\frac{\left(1+R\right)\mu_r}{\pm q_t}\right)\left(1+R\right)\mathrm{B}_{4t} - \left(\frac{1+R}{\pm q_t}\right)\left(1-R\right)\mathrm{B}_{5t} - \left(\frac{1+R}{\pm q_t \varepsilon_r}\right)\left(1+R\right)\mathrm{B}_{6t}\end{aligned} \quad . \tag{2.48h}$$

For self-contained and easy reference, the coefficients C, B, C_t B_t appearing in Eq. (2.48) are given in Appendix 2.A. Note that the coefficients C_t B_t for the lower or transmitted medium have the same forms as C and B, with q simply being replaced by q_t.

With the scattered fields calculated, we perform ensemble averaging to compute the scattered power and the scattering coefficient. To gain more physical insights into the field interactions that produce the average power, the following expression for the incoherent average power is written as a sum of three terms: the Kirchhoff power, the cross power due by the Kirchhoff field and the complementary power:

$$\begin{aligned} P_{qp}^{s} &= \left\langle E_{qp}^{s} E_{qp}^{s*} \right\rangle - \left\langle E_{qp}^{s} \right\rangle \left\langle E_{qp}^{s*} \right\rangle = \left\langle E_{qp}^{k} E_{qp}^{k*} \right\rangle - \left\langle E_{qp}^{k} \right\rangle \left\langle E_{qp}^{k*} \right\rangle \\ &\quad + 2\mathfrak{Re}\left[\left\langle E_{qp}^{c} E_{qp}^{k*} \right\rangle - \left\langle E_{qp}^{c} \right\rangle \left\langle E_{qp}^{k*} \right\rangle \right] + \left\langle E_{qp}^{c} E_{qp}^{c*} \right\rangle - \left\langle E_{qp}^{c} \right\rangle \left\langle E_{qp}^{c*} \right\rangle \\ &\triangleq P_{qp}^{k} + P_{qp}^{kc} + P_{qp}^{c} \end{aligned} \tag{2.49}$$

where < > denotes the ensemble average over the randomly rough surface $z(x,y)$ and * is the complex conjugation operator. The final expression of the scattering coefficient under the AIEM model, a relatively compact form, is given by:

$$\sigma_{qp}^{s} = \frac{k_1^{\,2}}{2} \exp[-\sigma^2 (k_{iz}^2 + k_{sz}^2)] \sum_{n=1}^{\infty} \frac{\sigma^{2n}}{n!} \mid \mathscr{I}_{qp}^{n} \mid^2 W^{(n)}(k_{sx} - k_{ix}, k_{sy} - k_{iy}) \tag{2.50}$$

where

$$\begin{aligned} \mathscr{I}_{qp}^{n} = {} & (k_{sz} + k_{iz})^n f_{qp} \exp(-\sigma^2 k_{iz} k_{sz}) \\ & + \frac{1}{4} \{ \mathscr{F}_{qp}^{+}(-k_{ix}, -k_{iy})(k_{sz} - k_{iz})^n \exp[-\sigma^2 (k_{iz}^2 - k_{iz}(k_{sz} - k_{iz}))] \\ & + \mathscr{F}_{qp}^{-}(-k_{ix}, -k_{iy})(k_{sz} + k_{iz})^n \exp[-\sigma^2 (k_{iz}^2 + k_{iz}(k_{sz} - k_{iz}))] \\ & + \mathscr{F}_{qp}^{+}(-k_{sx}, -k_{sy})(k_{sz} + k_{iz})^n \exp[-\sigma^2 (k_{iz}^2 - k_{iz}(k_{sz} - k_{iz}))] \\ & + \mathscr{F}_{qp}^{-}(-k_{sx}, -k_{sy})(k_{sz} - k_{iz})^n \exp[-\sigma^2 (k_{iz}^2 + k_{iz}(k_{sz} - k_{iz}))] \\ & + \mathscr{G}_{qp}^{+}(-k_{ix}, -k_{iy})(k_{sz} - k_{tz})^n \exp[-\sigma^2 (k_{tz}^2 - k_{tz}(k_{sz} - k_{iz}))] \end{aligned}$$

$$+\mathscr{G}_{qp}^{-}(-k_{ix},-k_{iy})(k_{sz}+k_{tz})^{n}\exp[-\sigma^{2}(k_{tz}^{2}+k_{tz}(k_{sz}-k_{iz}))]$$

$$+\mathscr{G}_{qp}^{+}(-k_{sx},-k_{sy})(k_{sz}+k_{tz})^{n}\exp[-\sigma^{2}(k_{tz}^{2}-k_{tz}(k_{sz}-k_{iz}))]$$

$$+\mathscr{G}_{qp}^{-}(-k_{sx},-k_{sy})(k_{sz}-k_{tz})^{n}\exp[-\sigma^{2}(k_{tz}^{2}+k_{tz}(k_{sz}-k_{iz}))]\} \qquad (2.51)$$

and $W^{(n)}(k_{sx}-k_{ix},k_{sy}-k_{iy})$ is the surface roughness spectrum of the surface related to the n^{th} power of the surface correlation function by the two-dimensional Fourier transform, assuming the surface height is Gaussian distribution.

The Fresnel reflection coefficient for a homogenous rough surface is dependent on the local incidence angle, which is determined by the incident direction and surface unit normal. The Fresnel reflection coefficients for horizontally and vertically polarized waves are, respectively:

$$R_{h}=\frac{\mu_{t}k_{i}\cos\theta_{i}-\mu_{0}k_{tz}}{\mu_{t}k_{i}\cos\theta_{i}+\mu_{0}k_{tz}}, \qquad (2.52a)$$

$$R_{v}=\frac{\varepsilon_{0}k_{tz}-\varepsilon_{t}k_{i}\cos\theta_{i}}{\varepsilon_{t}k_{i}\cos\theta_{i}+\varepsilon_{0}k_{tz}}, \qquad (2.52b)$$

where

$$k_{tz}=\mathscr{Re}\{k_{tz}\}+j\mathscr{Im}\{k_{tz}\} \qquad (2.52c)$$

with

$$\mathscr{Re}\{k_{tz}\}=\frac{1}{\sqrt{2}}\left[\mathscr{Re}\{k_{t}^{2}\}-k_{i}^{2}\sin^{2}\theta_{i}+\sqrt{\left(\mathscr{Re}\{k_{t}^{2}\}-k_{i}^{2}\sin^{2}\theta_{i}\right)^{2}+\left(\mathscr{Im}\{k_{t}^{2}\}\right)^{2}}\right]^{1/2} \qquad (2.52d)$$

and

$$\mathscr{Im}\{k_{tz}\}=-\frac{1}{\sqrt{2}}\left[-\left(\mathscr{Re}\{k_{t}^{2}\}-k_{i}^{2}\sin^{2}\theta_{i}\right)+\sqrt{\left(\mathscr{Re}\{k_{t}^{2}\}-k_{i}^{2}\sin^{2}\theta_{i}\right)^{2}+\left(\mathfrak{I}\{k_{t}^{2}\}\right)^{2}}\right]^{1/2} . \qquad (2.52e)$$

In modelling the wave scattering, it is a common practice, in order to remove the spatial dependence of the reflection coefficient, to approximate the local incident angle either by the incident angle for a slightly rough surface or otherwise by the specular angle. Such approximation, however, leads to an unpredictable error for the local incident angle, which is random in nature across the rough surface. A transition model was proposed by Ulaby et al. (Fung et al., 2002) to fix such a deficiency. It is necessary to generalize the transition function so that the local angle variation is accounted for. This is important for a scattering model to cover a wider range of surface roughness. Recalling that the scattering coefficient may be decomposed into three terms, recognized as the Kirchhoff, cross, and complementary terms: $\sigma_{qp}^{o} = \sigma_{qp}^{k} + \sigma_{qp}^{kc} + \sigma_{qp}^{c}$. The transition model took two extremes of the form (Fung et al., 2002):

$$R_p(T) = R_p(\theta_i) + [R_p(\theta_{sp}) - R_p(\theta_i)]\gamma_p \tag{2.53}$$

where θ_i is the incidence angle and θ_{sp} is the specular angle, and realized that the transition function is defined as:

$$\gamma_p = 1 - \frac{S_p}{S_p^{o}} \tag{2.54a}$$

with

$$S_p = \frac{\sigma_{pp}^{c}\Big|_{R_p = R_p(0)}}{\sigma_{pp}^{o}\Big|_{R_p = R_p(0)}} \quad ; \tag{2.54b}$$

$$S_p^{o} = \lim_{k\sigma \to 0} \frac{\sigma_{pp}^{c}\Big|_{R_p = R_p(0)}}{\sigma_{pp}^{o}\Big|_{R_p = R_p(0)}} \quad . \tag{2.54c}$$

Note that $\lim_{k\sigma \to 0} \sigma_{pp}^{o} = a + b + c$, $\lim_{k\sigma \to 0} \sigma_{pp}^{c} = c$, with the coefficients a, b, c, corresponding to the Kirchhoff, cross and complementary terms, respectively. Under the framework of the AIEM model, the three terms are given in Appendix 2B.

Chapter 3 Comparison of AIEM with numerical simulations and experimental data

3.1 Motivation

The study of microwave scattering has wide applications in telemetry, wireless transform, radar detection and so on. A practical and reliable surface scattering model is required to obtain a good understanding of the surface scattering mechanism. Research into microwave scattering on a random surface has been going on for over forty years. During the years 1960 to 1970, several surface scattering models were developed, including the Small Perturbation Model (SPM) and the Kirchhoff Model. These two models are considered as the preeminent standards within their scope of application. The SPM is capable in the low-frequency and the small-surface-perturbation circumstances, whereas the Kirchhoff model is suitable for high-frequency and large-scale rough surfaces.

Since 1990, Dr A. K. Fung has proposed the Integral Equation Model (IEM) which first solves the limitation of the application scope (Fung 1994). The original IEM was developed based on several simplifying approximations leading to a relatively simple, and yet reasonably accurate, solution of a pair of integral equations governing the surface currents. There has been significant progress in improving the surface current estimate in order to extent its region of validity. For example, the Fresnel reflection coefficients have been generalized by replacing them with a transition reflection coefficient. This allows the argument of the Fresnel reflection coefficients to change from the incident angle to the specular angle as the operating frequency and surface roughness changes from small to large values. However, in the IEM model, the surface height dependence on the phase of the Green’s function was ignored, leading to a significant error away from the backscattering direction.

The advanced IEM model (AIEM) is a physically-based extension of the IEM analytical model. It shows significant improvements for single scattering and emissivity predictions for a wide range of roughness scales, particularly in the intermediate roughness regions (Chen et al., 2003). Furthermore, multiple-surface scattering agrees well with numerical simulation results and controlled laboratory measurements acquired from known surfaces.

The AIEM removed some weak assumptions from the original IEM (Shi et al., 2005). In the expressions of the multiple (Chen et al., 2000) and the single scattering (Chen et al., 2003) terms, the absolute phase terms in the surface Green's function and its gradient were kept, but were rederived by the complementary field.

Although the AIEM is theoretically considered to provide accurate predictions, the accuracy level of its predictions need to be further confirmed. In this research, the AIEM was adopted for analysing the backscattering and the bistatic scattering characteristics of the rough surface, analysis which is covered in the next two chapters. It is very necessary to validate the accuracy of AIEM to draw more reliable conclusions. Thus, in this chapter, we investigate how the AIEM predictions were validated by comparison with numerical simulations and experimental data.

3.2 Comparison with numerical simulations

The Numerical Maxwell Model based on 3-D simulations of Maxwell equations (NMM3D) is a single physical model over a wide frequency range with a single set of physical parameters of RMS height and correlation function (Chen et al., 2014; Huang and Tsang, 2012). It has the advantage of high accuracy of the simulation results (Huang et al., 2010).

3.2.1 Comparison with NMM3D for backscattering

The NMM3D method applies a moment-based algorithm to calculate rough surface scattering. It can be applied in both active and passive remote sensing. When it is applied in the active remote sensing case, NMM3D provides bistatic scattering coefficients and the backscattering coefficients. It provides emissivity when it is applied in the passive remote sensing case, where it can also be used to calculate brightness temperature. Recently, we tried to actualize a near-field precondition to further speed up the convergence as well as simulation time. Although the computation is complex, look-up tables (LUT) were pre-computed for both backscattering coefficients and emissivity.

3.2.1.1 For $\frac{s}{l} = \frac{1}{4}$

Surface roughness plays a significant role in microwave remote sensing of soil. We set our experiments in four different surface roughness conditions, varying from rough to smooth. We first set the RMS height and the correlation length ratio to 1/4. These results are shown in Figs. 3.1 and 3.2. Obviously, all the three predictions are quite close to each other, especially at VV polarization.

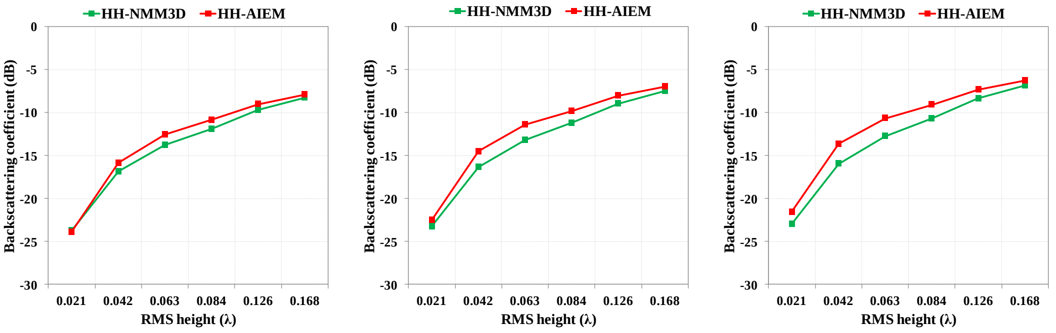

(a) (b) (c)

Figure 3.1 Comparison of backscattering coefficients between AIEM and NMM3D for horizontal polarization for an exponentially correlated surface with incident angle of 40°: (a) εr=15-j3.5, (b) εr=22-j4, and (c) εr=30-j4.5.

In the HH polarization, we can observe that as the dielectric constant increases, the AIEM backscattering coefficient appears to a little bit higher than the NMM3D backscattering coefficient. In addition, as the dielectric constant increases, the divergence of the AIEM and the NMM3D backscattering coefficient becomes larger. The most obviously difference between the two models is around the places where the RMS height is from 0.042λ to 0.063λ.

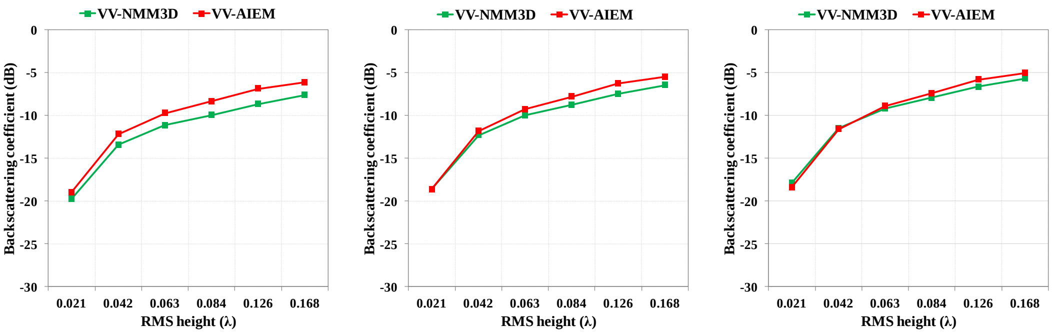

(a) (b) (c)

Figure 3.2 The same as Fig. 3.1 but for vertical polarization.

In the VV polarization, at a large dielectric constant there is essentially no difference between the two models, as was expected. However, results from the AIEM model are also a little bit higher that the NMM3D model, as it was in the HH case. Furthermore, the difference between the two models becomes larger as the RMS height increases. Overall, the two models are in good agreement with each other, especially when the dielectric constant is large and the RMS height is small.

3.2.1.2 For $\frac{s}{l} = \frac{1}{7}$

In the second part, all the settings are the same as in the first part expect the soil roughness is smoother than for the case illustrated in Figs. 3.1 and 3.2. We can see from Fig. 3.3 that the backscattering coefficients predicted by AIEM are also higher than those predicted by NMM3D. When the soil moisture is higher, the difference between the two models increases.

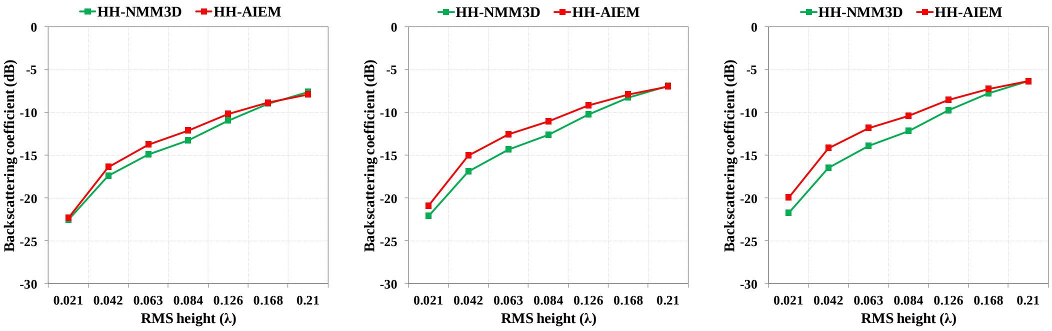

(a) (b) (c)

Figure 3.3 Comparison of backscattering coefficients between AIEM and NMM3D for horizontal polarization for an exponentially correlated surface with incident angle of 40°: (a) εr=15-j3.5, (b) εr=22-j4, and (c) εr=30-j4.5.

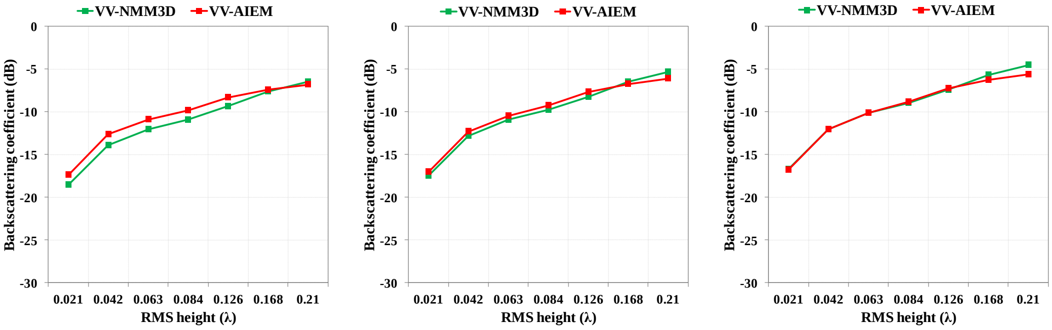

(a) (b) (c)

Figure 3.4 The same as Fig. 3.3 but for vertical polarization.

Also it is clear that in Figure 3.4, in the transition model, more consistencies can be found in the vertical polarization case than in the horizontal polarization case. With the decrease of the surface roughness, the behaviour follows perfectly, as we observed in Fig. 3.2, but the conformance has grown slightly.

3.2.1.3 For $\frac{s}{l} = \frac{1}{10}$

In the third experiment, the surface roughness was smoothed further. As seen in Fig. 3.5, the trends by three predictions are similar to those in Figs. 3.1 and 3.3. With increase of the RMS height, the divergence between the two models disappears.

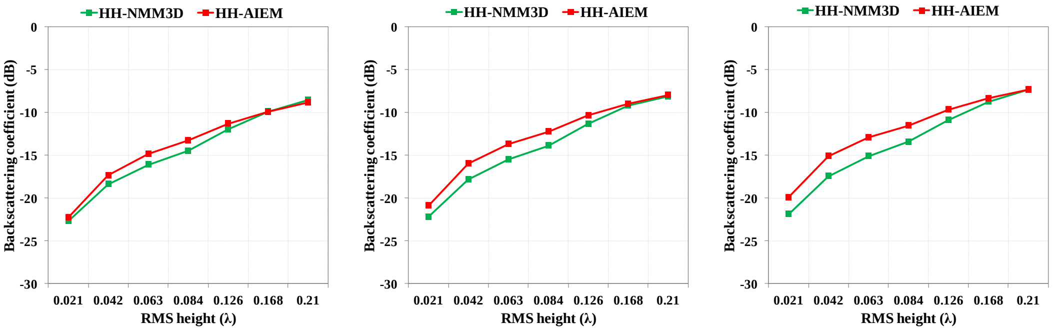

(a) (b) (c)

Figure 3.5 Comparison of backscattering coefficients between AIEM and NMM3D for horizontal polarization for an exponentially correlated surface with incident angle of 40°: (a) εr=15-j3.5, (b) εr=22-j4, and (c) εr=30-j4.5.

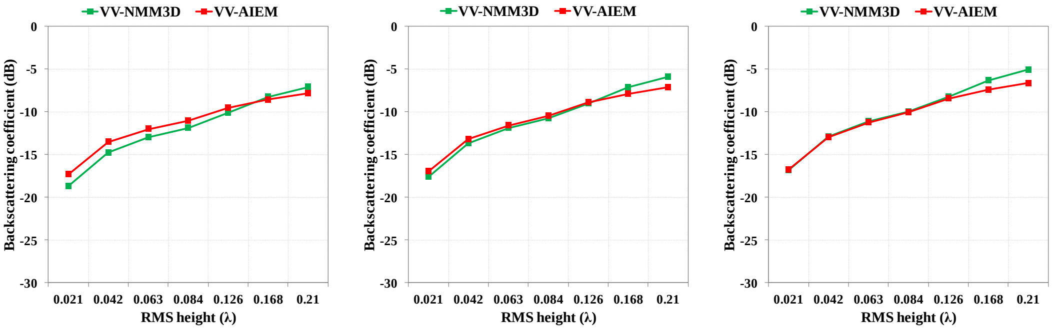

(a) (b) (c)

Figure 3.6 The same as Fig. 3.5 but for vertical polarization.

Like shown in Figs 3.6, similar behaviour can be observed in Figs. 3.2 and 3.4. With the decreases in surface roughness, agreement between the AIEM and the NMM3D increased. As the RMS height rose, the divergence decreased in the low soil moisture situation (a), which is opposite from the results for the situations (b) and (c).

3.2.1.4 For $\frac{s}{l}=\frac{1}{15}$

As shown in Figure 3.7 and Figure 3.5, in the fourth part of the comparison between the AIEM and the NMM3D, we can conclude that, in HH polarization, the difference between the two models increases with decreasing surface roughness. In general, the AIEM model and the NMM3D show a good consensus in the HH polarizations. In VV polarizations, when the RMS height is less than 0.084λ, especially in the case of low surface roughness, the two models have an excellent agreement.

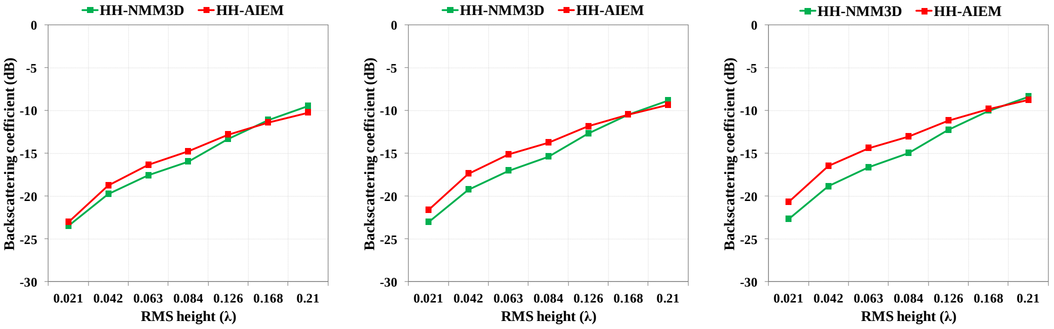

(a) (b) (c)

Figure 3.7 Comparison of backscattering coefficients between AIEM and NMM3D for horizontal polarization for an exponentially correlated surface with incident angle of 40°: (a) εr=15-j3.5, (b) εr=22-j4, and (c) εr=30-j4.5.

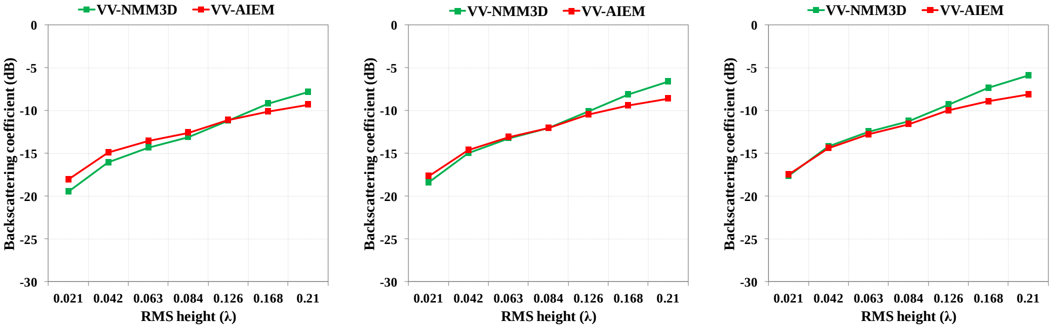

(a) (b) (c)

Figure 3.8 The same as Fig. 3.7 but for vertical polarization.

3.2.2 Comparison with MoM and SSA for bistatic scattering

To illustrate the accuracy of bistatic scattering coefficients predicted by AIEM, comparisons were made between numerical methods and other physical surface scattering models. Results of these comparisons are offered in this section.

The Fresnel reflection coefficient is a function of the surface permittivity and surface local incidence angle. In modelling the wave scattering, it is significant to reproduce the spatial dependence. Wu et al. (2001) have proposed a transition model to fix its deficiency in bistatic scattering.

Comparison of the prediction of scattering coefficients in the scattering plane from the AIEM model with numerical results from the SSA (Small Slope Approximation) and from the MoM (method of moment) methods are shown in Figs. 3.9. and 3.10. A Gaussian correlated surface with complex dielectric constant 4-*j*1 is used. A moderate rough surface with parameters *kσ*=0.5 and *kl*=3.0 was set. The incident angle is 30 °.

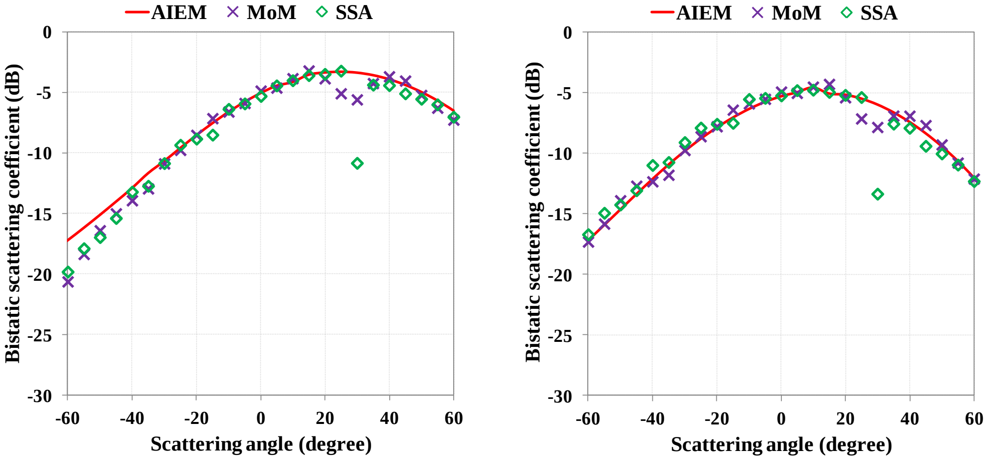

(a) (b)

Figure 3.9 Comparison of bistatic scattering coefficients between AIEM and numerical results of MoM and SSA for a Gaussian correlated surface with εr=4-j1, kσ=0.5, kl=3.0, and incident angle of 30°: (a) horizontal polarization and (b) vertical polarization.

In Fig. 3.9 we can observe that all the three predictions agree very well with each other except at larger backscattering angles. The largest divergence of the three models appears around the point where the scattering angle varies from 20 ° to 40 °. There is dip in specular direction shown by MoM and SSA, but not by AIEM. In HH polarization, the AIEM backscattering coefficient is higher than the MOM and the SSA at scattering angles from -60 ° to -20 °. The predictions at VV polarization have a better agreement between the three models.

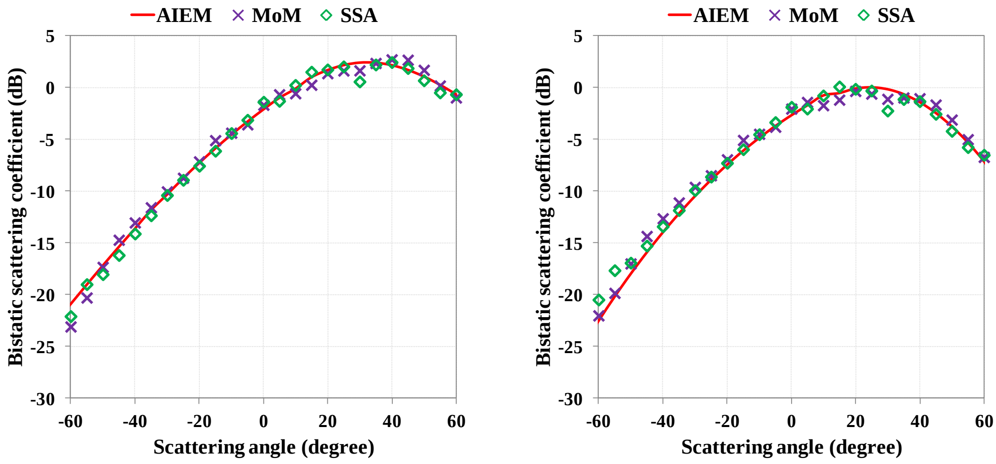

(a) (b)

Figure 3.10 Comparison of bistatic scattering coefficients between AIEM model and numerical results of MoM and SSA for a Gaussian correlated surface with εr=4-j1, kσ=1.0, kl=6.0, and incident angle of 30°: (a) horizontal polarization and (b) vertical polarization.

Compared with Fig. 3.9, the results shown in Fig. 3.10 has a different setting of *kσ*=1.0, *kl*=6.0, which means rougher surface conditions. The rougher surface roughness slightly decreases the divergence between the three models. Generally, the three models are quite close to each other.

3.3. Comparisons with measurement data

3.3.1 Comparison with UM data for backscattering

The University of Michigan's LCX POLASCAT scatter meter (Tassoudji et al., 1989) was designed with the capability of measuring the scattering matrix of point or distributed targets at the L, C, and X bands (with centre frequencies at 1.5, 4.75, and 9.5 GHz, respectively). To verify the validity of the AIEM model, we compared the AIEM backscattering coefficients with measurement data provided by the LCX POLASCAT. These experiments were under three kinds of the frequencies at the L, C, and X bands (the frequencies at 1.5, 4.75, 9.5GHz, respectively) and three kinds of the surface roughness. These conditions are shown below.

3.3.1.1 For Surface 1 (S1)

In the first part, we validated the AIEM under moderate surface roughness conditions. In this case, the RMS height σ was 0.4 cm, and the correlation length l was 8.4 cm. Three different frequencies (1.5, 4.75, and 9.5 GHz) were examined in this part. Each was measured under two different moisture conditions, wet and dry, relatively.

L band:

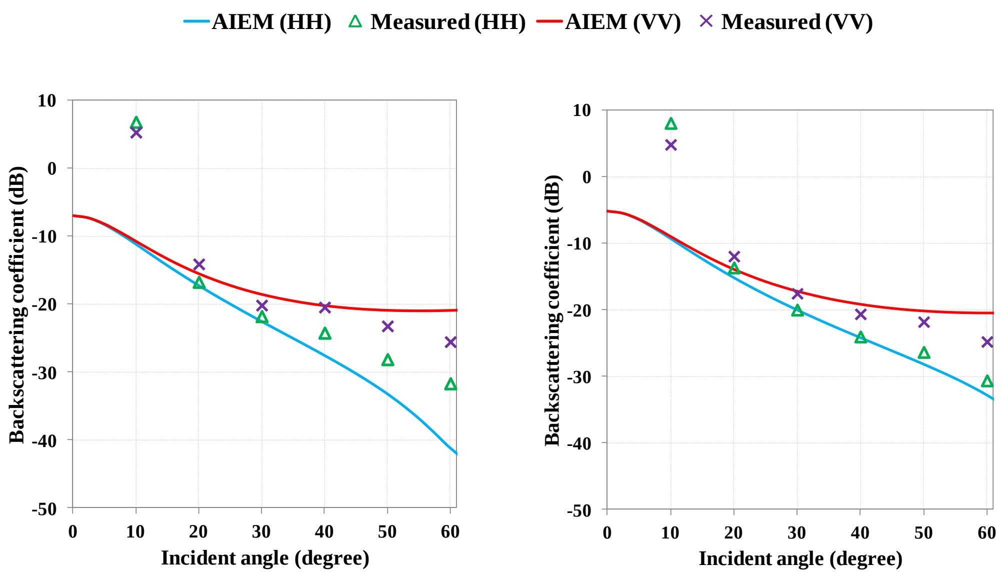

(a) (b)

Figure 3.11 Comparison of backscattering coefficients between AIEM and UM measurements for an exponentially correlated surface with σ=0.4 cm and l=8.4 cm at 1.5 GHz: (a) dry soil (εr=7.99-j2.02), and (b) wet soil (εr=15.57-j3.71).

In Fig. 3.11 we can observe that, for dry soils at HH polarization, as the incident angle varies from 20 ° to 30 ° excellent agreement between measurement and AIEM can be seen. The maximal error appears at the low incident angle. In the dry condition, backscattering coefficients at HH polarization are smaller than the measurement data. However, the backscattering coefficients at VV polarization are larger than the measurement data. In the wet soil condition, the comparison results show a good agreement, better than in the dry soil condition.

C band:

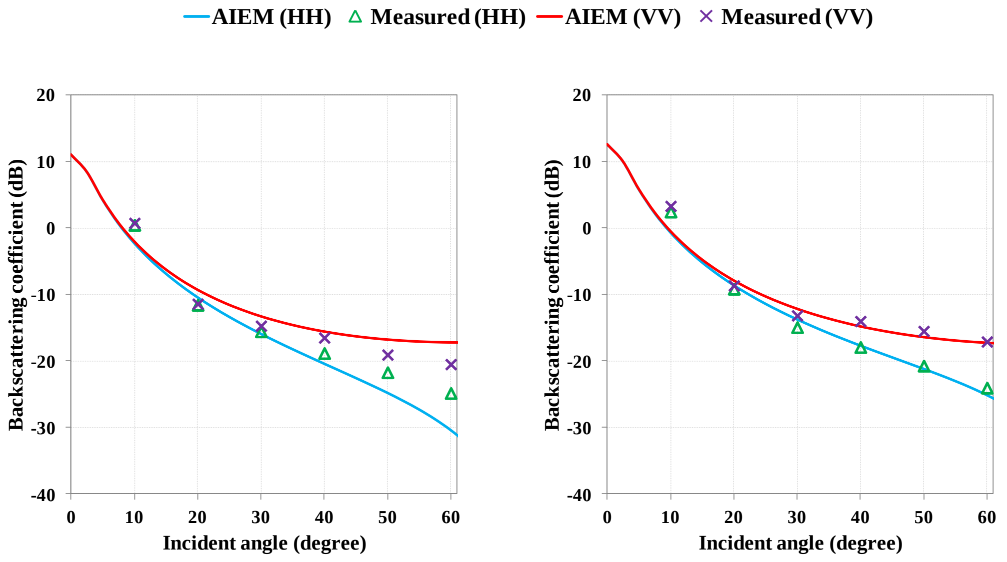

(a) (b)

Figure 3.12 Comparison of backscattering coefficients between AIEM and UM measurements for an exponentially correlated surface with σ=0.4 cm and l=8.4 cm at 4.75 GHz: (a) dry soil (εr=8.77-j1.04), and (b) wet soil (εr=15.42-j2.15).

We can see that results with the C band are similar with the L band results like shown in Figure 3.12. The largest divergence also appears at 10°, but the error is, obviously, smaller. In the dry condition at HH polarization, the measurement data is larger than the HH AIEM data, but smaller than the VV AIEM data. The predictions of AIEM in the wet soil condition also present a better accuracy than at the dry surface condition.

X band:

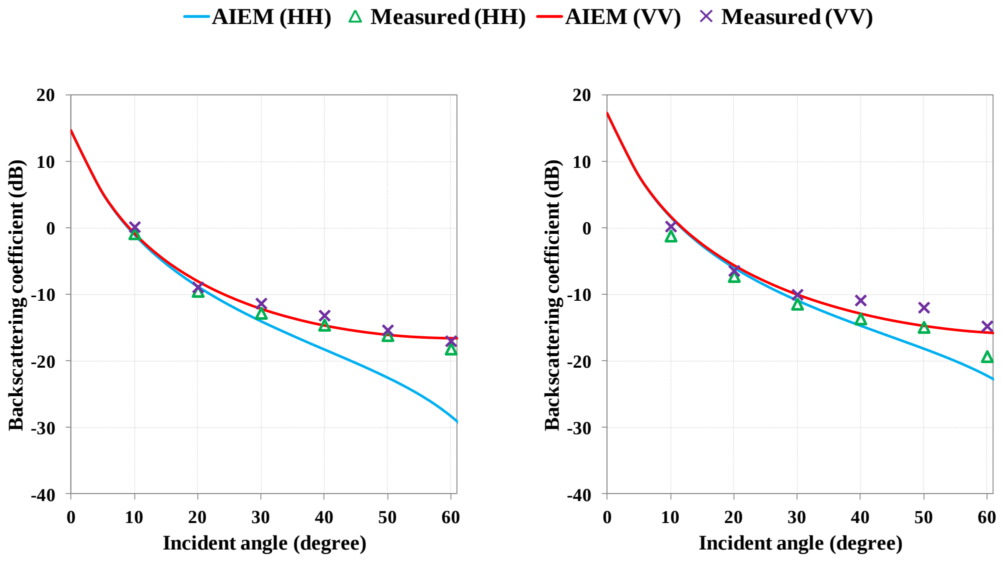

(a) (b)

Figure 3.13 Comparison of backscattering coefficients between AIEM and UM measurements for an exponentially correlated surface with σ=0.4 cm and l=8.4 cm at 9.5 GHz: (a) dry soil (εr=5.70-j1.32), and (b) wet soil (εr=12.31-j3.55).

Fig. 3.13 displays the comparisons at the X band. In the dry condition, the VV polarization shows a good agreement when the incident angle is less than 60 °. In HH polarization, the large divergence occurs when the incident angle is between 30 ° and 70 °. In the wet condition, the divergence stayed between 1dB to 3dB when the incident angle was less than 60 °. In sum, we can conclude the model agrees well at the X band.

3.3.1.2 For Surface 2 (S2)

In the second part, we decreased the soil roughness to illustrate the effect of soil roughness on the accuracy of the AIEM.

L band:

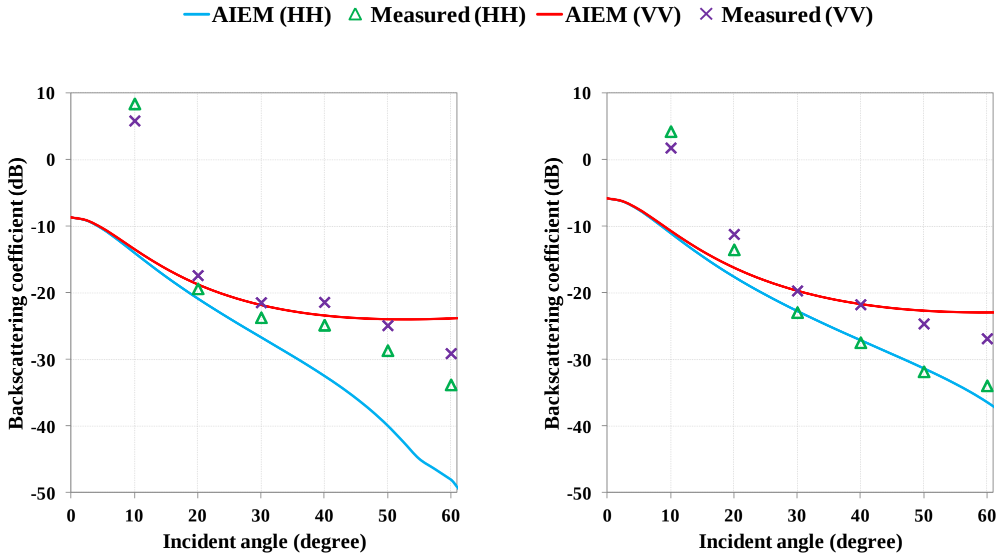

(a) (b)

Figure 3.14 Comparison of backscattering coefficients between AIEM and UM measurements for an exponentially correlated surface with σ=0.32 cm and l=9.9 cm at 1.5 GHz: (a) dry soil (εr=5.85-j1.46), and (b) wet soil (εr=14.43-j3.47).

Compared the Figure 3.14 with the Fig. 3.11, the divergence increases with the incident coefficient at 30 ° in the dry condition at both HH and VV polarizations. With the decrease of surface roughness, the error increases in the dry condition. In the wet condition, change of surface roughness does not cause obvious differences between AIEM predictions and the measurement data.

C band:

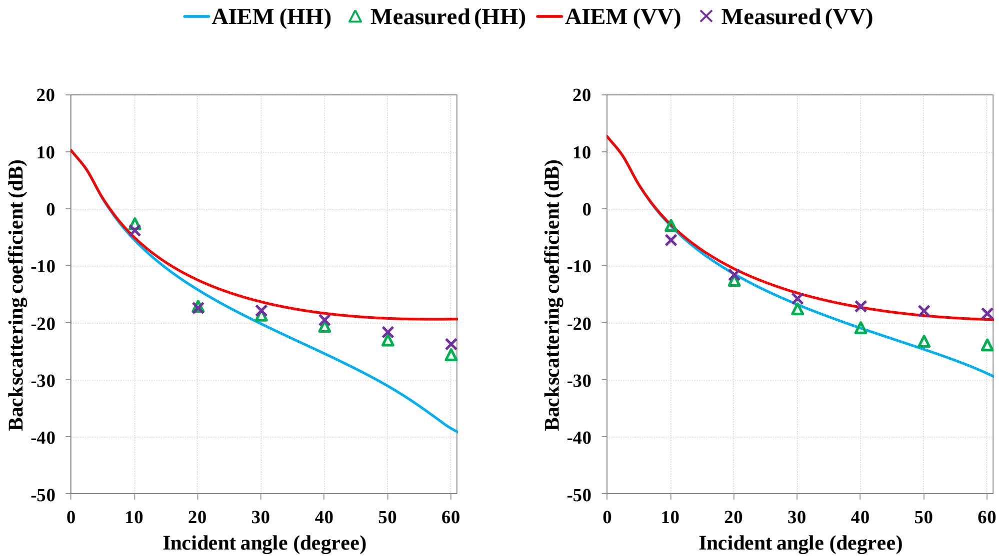

(a) (b)

Figure 3.15 Comparison of backscattering coefficients between AIEM and UM measurements for an exponentially correlated surface with σ=0.32 cm and l=9.9 cm at 4.75 GHz: (a) dry soil (εr=6.66-j0.68), and (b) wet soil (εr=14.47-j1.99).

As shown in Figure 3.15, at the C band, with the decrease of surface roughness, the divergence between the measurements and the AIEM increased in the dry condition compared to results shown in Fig. 3.12, especially in the HH polarization. However, in the wet condition the difference between the AIEM and the measurement data did not change a lot compared with results shown in Fig. 3.12.

X band:

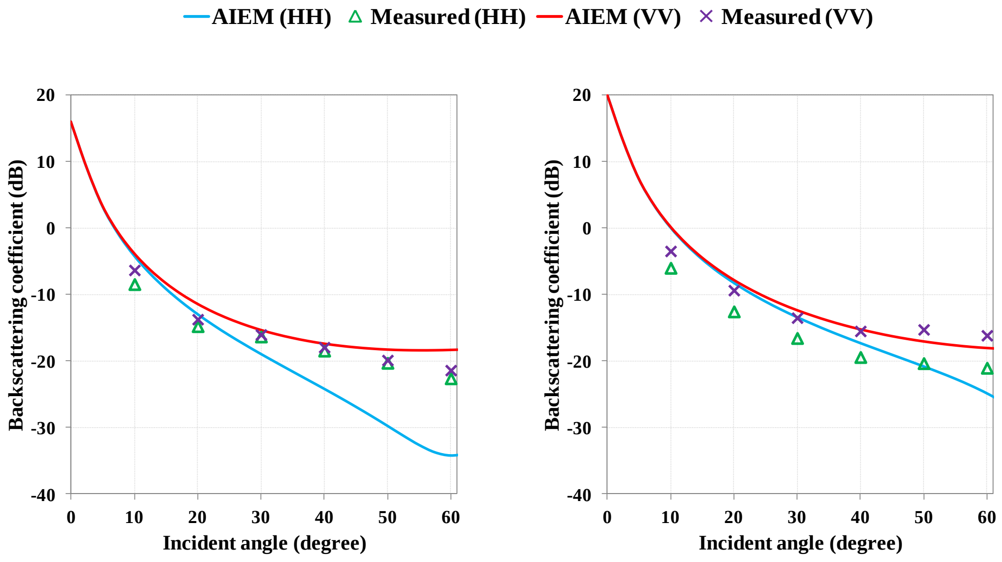

(a) (b)

Figure 3.16 Comparison of backscattering coefficients between AIEM and UM measurements for an exponentially correlated surface with σ=0.32 cm and l=9.9 cm at 9.5 GHz: (a) dry soil (εr=4.26-j0.76), and (b) wet soil (εr=12.64-j3.69).

In the above illustrations, we have shown the effect of decreasing the soil roughness on the accuracy of AIEM. As shown in Fig. 3.16, at the X band, in the dry condition, the divergence increased as the incident angle increased. It is obvious that the results from the wet condition agree better with measurement data than do those from the dry condition.

3.3.1.3 For Surface 3 (S3)

In the third part we continue comparing the AIEM predictions with the measurement data. In this case, the RMS height *σ* is 1.12 cm and the correlation length *l* is 8.4 cm, which corresponds to the roughest surface among the three experiments.

L band:

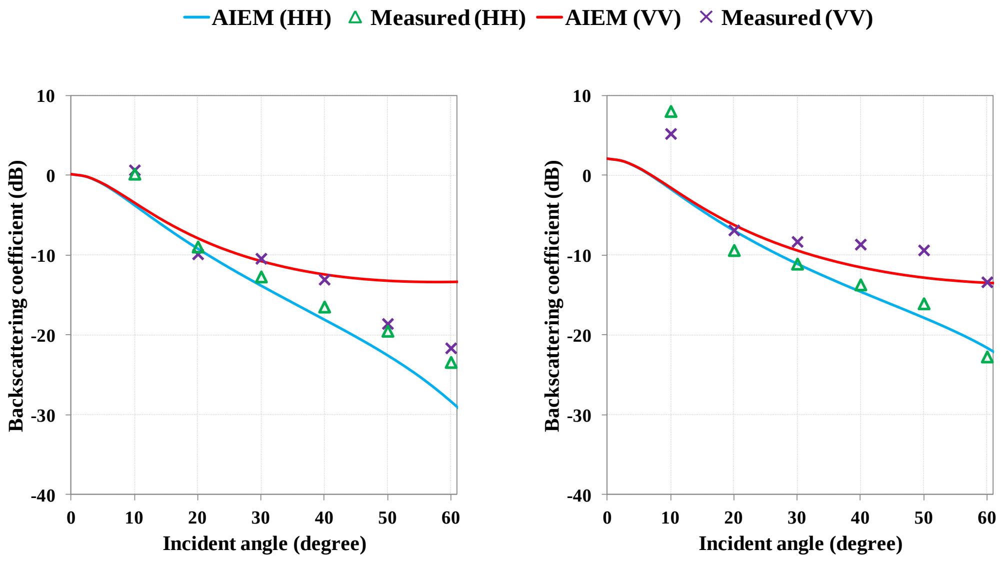

(a) (b)

Figure 3.17 Comparison of backscattering coefficients between AIEM and UM measurements for an exponentially correlated surface with σ=1.12 cm and l=8.4 cm at 1.5 GHz: (a) dry soil (εr=7.70-j1.95), and (b) wet soil (εr=15.34-j3.66).

At the L band, the best agreement of HH polarization and the largest disagreement of VV polarization all occurred in the dry condition. This can be seen in Fig. 3.17(a). The largest error also followed by the incident angle equal to 10 degrees.

C band:

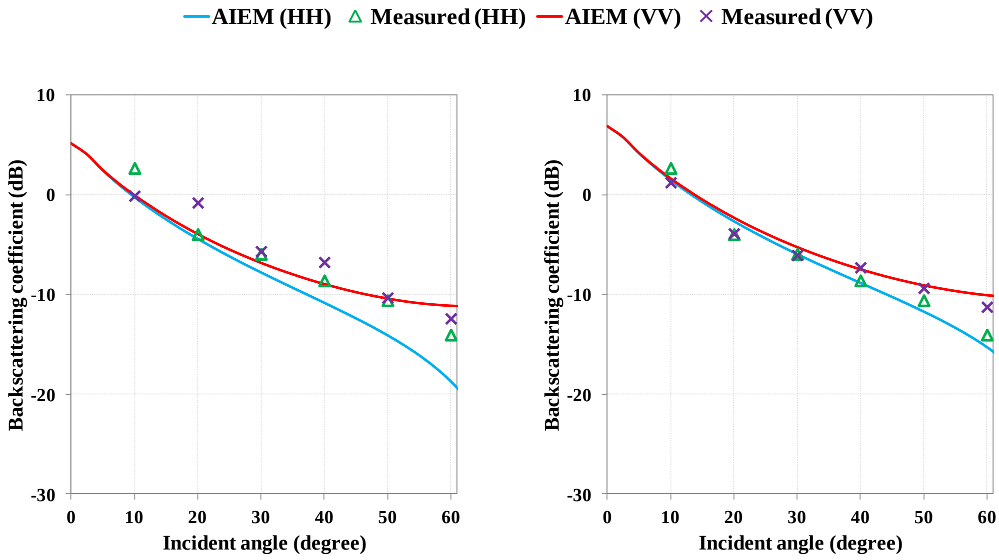

(a) (b)

Figure 3.18 Comparison of backscattering coefficients between AIEM and UM measurements for an exponentially correlated surface with σ=1.12 cm and l=8.4 cm at 4.75 GHz: (a) dry soil (εr=8.50-j1.00), and (b) wet soil (εr=15.23-j2.12).

In Figure 3.18 we can observe that under the surface condition 3, we continuous comparing the AIEM predictions with the measurement data. In vertical polarization, the accuracy decreased with the increase of the incident angle. Compare with the dry soil, the accuracy is large when the soil moisture is large both in vertical and horizontal polarizations.

X band:

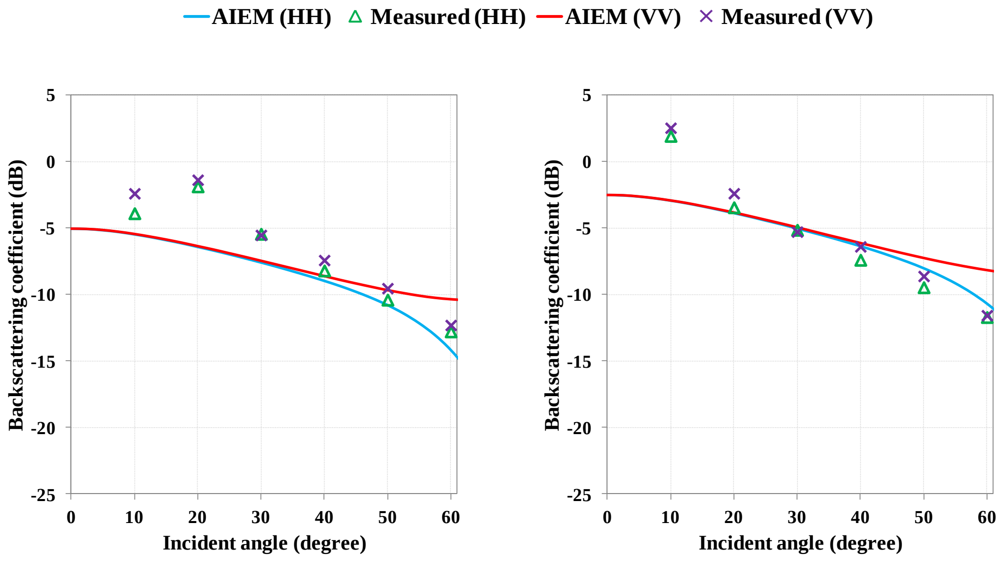

(a) (b)

Figure 3.19 Comparison of backscattering coefficients between AIEM and UM measurements for an exponentially correlated surface with σ=1.12 cm and l=8.4 cm at 9.5 GHz: (a) dry soil (εr=6.07-j1.46), and (b) wet soil (εr=13.14-j3.85).

In the Figure 3.19 we can conclude that in this experiment in X band, the divergence of the AIEM data and the measurement data increases with the surface roughness. Also the accuracy is increasing with the incident angle. The error between the different soil moisture conditions is very little.

3.3.1.4 Conclusions

For the same set of the surfaces, different measurements over a wider frequency are compared to the model predictions. There are three different fields examined in this part. Each was measured under the dry and the wet soil conditions, respectively. It is of interest to know that different soil roughness will cause different results, but the trends are always similar with the same frequency. One peculiar point is that there is a jump in the measurements at the L band when the incident angle is 10°. This phenomenon does not show for the case at the X band. Overall, the AIEM predictions matched well with the POLASCAT measurement data.

3.3.2 Comparison with EMSL data for bistatic scattering

The bistatic scattering measurement data used here was acquired by the European Microwave Signature Laboratory (EMSL). The EMSL is a facility which provides unique measurement capabilities in the field of microwave remote sensing and Radio Frequency (RF) compatibility. While the laboratory was originally designed to perform wide-band polarimetric radar measurements, it has been successfully used in many other research fields such as antenna measurements, material testing through microwaves, and detection of buried objects.

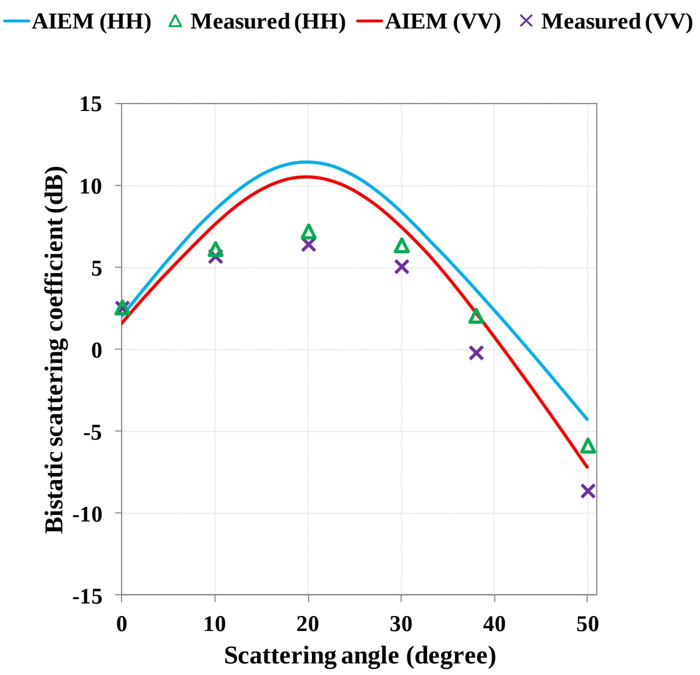

Figure 3.20 Comparison of bistatic scattering coefficients between AIEM and EMSL measurements for a Gaussian correlated surface with εr=5.5-j2.1, σ=0.4 cm, l=6 cm, and incident angle of 20° at 11 GHz.

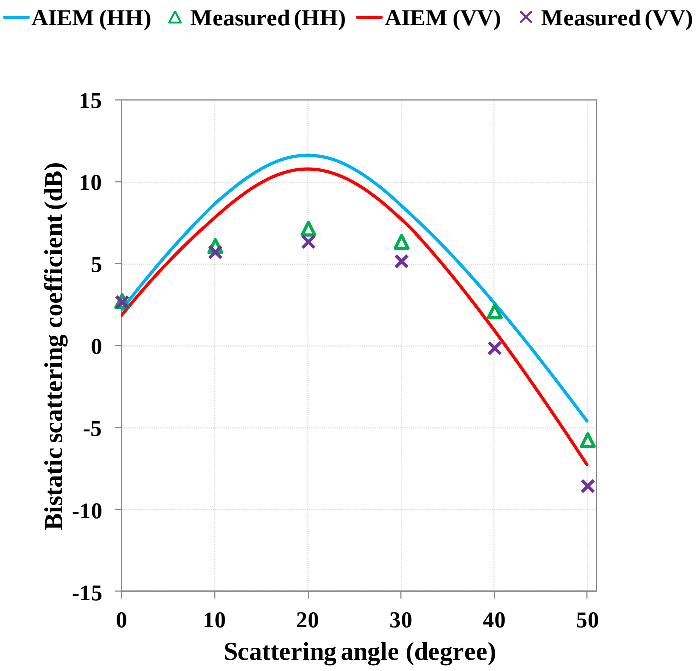

Figure 3.21 Comparison of bistatic scattering coefficients between AIEM and EMSL measurements for a Gaussian correlated surface with εr=5.5-j2.1, σ=0.4 cm, l=6 cm, and incident angle of 20° at 13 GHz.

An experimental data set for the purpose of this comparison was adopted for a Gaussian correlated surface with σ=0.4 cm and l=6 cm. The scattering coefficient was measured at the incident angle of 20°; the dielectric constant was ε_r=5.5-j2.1; and the frequencies used were 11 GHz and 13 GHz, resulting in two different roughness scales with the same surface slope. Fig. 3.20 shows the bistatic scattering behaviour from the AIEM and EMSL data at 11 GHz. The AIEM agrees well with the measurement data except at scattering angles near 20°. Measurements at the frequency of 13 GHz are presented in Fig. 3.21, where similar results can be observed. The bistatic scattering coefficients predicted by AIEM are a little bit higher than the EMSL data. At the frequency of 13 GHz, the AIEM model shows a better accuracy than for 11 GHz shown in Fig. 3.20.

3.4 Conclusions

A practical and reliable surface scattering model is required to achieve a good understanding of the surface scattering mechanism. To demonstrate the applicability of the AIEM, which is considered to have a much wider valid range for surface roughness conditions as compared to conventional models such as SPM and the geometric optics model, we validated the AIEM by comparison with numerical simulations and experimental data. In the first part, we compared AIEM with numerical simulations for both backscattering and bistatic scattering. For the backscattering, we compared AIEM with the 3D Numerical Method of Maxwell's equations (NMM3D). Under four different surface roughness conditions, the AIEM showed good agreement with the NMM3D, especially at VV polarization. In the bistatic conditions, we compared AIEM with the numerical results of SSA and the MoM in the scattering plane. The results showed that, compared with the numerical simulations data, all the predictions were quite close to each other except at a large scattering angle.

In the second part, we compared the AIEM predictions with measurement data in the backscattering and bistatic scattering conditions. The University of Michigan's LCX POLASCAT data was adopted in the backscattering comparison part under three kinds of surface roughness. The data sets were measured under two different moisture conditions, namely relatively wet and relatively dry. The surface roughness parameters, such as the RMS height, correlation length, and RMS slope, were calculated from the measured surface height profiles. The results show that the AIEM is generally in good agreement with the measured data in all cases. In bistatic scattering, data was acquired over known randomly rough surfaces by the European Microwave Signature Laboratory. When compared with this EMSL measurement data, AIEM also showed a good agreement although the predictions of the AIEM were on the high side at large scattering angles and there was not enough separation between the polarizations, especially when the scattering angle varied from 30 to 50 degrees.

In sum, the AIEM model matches well with both the numerical simulations and experimental data. Thus it is proven that the AIEM has a high level of accuracy in both the backscattering and bistatic scattering simulations over a wide valid range of surface roughness conditions and soil moisture conditions. For this reason, the numerical analysis of scattering behaviour in this research, as outlined in the next two chapters, was based on the AIEM.

Chapter 4 Sensitivity analysis of bistatic scattering to soil moisture and surface roughness of rough soils

4.1 Motivation

Soil moisture plays a significant role in the surface energy balance at the soil–atmosphere interface. A good knowledge of the spatiotemporal dynamics of soil moisture has proven to be particularly important in various environmental applications (Brocca et al., 2012; Miralles et al., 2011). On account of its strong sensitivity to the soil permittivity, active microwave remote sensing has a good physical basis for soil moisture estimation. Synthetic Aperture Radar (SAR) is particularly attractive for remote sensing of soil moisture at finer resolutions; it provides a measure of the absolute soil moisture contents that are spatially averaged, and it has the advantages of large-scale coverage and all-weather operation. Consequently, active microwave remote sensing, especially SAR, is considered as one of the most effective means for surface soil moisture monitoring in the present day (Baghdadi et al., 2016; El Hajj et al., 2016; Zribi et al., 2014b).

The traditional active radar system detects soil moisture almost entirely based on the backscattering coefficients. However, setting the transmitter and receiver in the same direction has apparent theoretical drawbacks, because only the signal from the backward direction can be obtained. One of the critical issues in estimation of surface parameters from radar backscattering signals is that the surface parameters, including statistical surface roughness (root-mean-square height s and correlation length l) and dielectric constant are strongly coupled under a certain set of radar parameters (frequency, incidence angle, and polarization) (Chen et al., 2001). This fact greatly hinders the capability of microwave sensing of soil moisture even for bare surfaces. Thus, it is of interest to understand the characteristics of bistatic scattering (which are much less understood as compared to backscattering) in order to find out an appropriate transmitter-receiver configuration for decoupling, to an optimal level, the surface roughness and dielectric constant. However, in bistatic configuration, there are numerous scenarios to be designed. Hence, it is essential to conduct a parameter sensitivity analysis to determine an optimal configuration which can maximize the information content of the parameters of interest while minimizing the contribution of undesired parameters.

Accordingly, estimating soil moisture in a bistatic mode has attracted increasing attention in the last few years. In some of the studies (e.g. Pierdicca et al., 2008; M. Brogioni et al., 2010), the researchers have found that, in comparison with traditional monostatic observation, using bistatic geometries can obtain more information to retrieve soil moisture. However, limited literature is available for purposes of soil moisture sensing with bistatic configuration. Hence, more work should be carried out to fully explore bistatic scattering behaviours with soil parameters under diverse ground conditions, which is of both theoretical and practical interest.

Several factors affect soil roughness characterization. In addition to correlation length and root-mean-square height (RMS height), the surface auto correlation function (ACF) also has an important influence (Davidson et al., 2000). In practical situations, the ACFs are hard to determine. Consequently, the effect of the ACFs is usually ignored or simply assumed a priori (e.g. Gaussian or Exponential) to simplify the inversion problem in the inversion process (Joseph et al., 2010; Shi et al., 2006). Therefore, how to suppress the effect of the ACFs for more reliable soil moisture estimation is also an attractive challenge.

The objective of this chapter is to describe our search for the optimal bistatic observation configuration for soil moisture estimation. To achieve this purpose, in this study, we investigated the sensitivity of bistatic scattering to soil moisture and surface roughness of bare soil surfaces. The AIEM was selected as the working model. Furthermore, in this study, we focused on the L-band (i.e. 1.26 GHz) as it shows good sensitivity to soil moisture, and the effects of vegetation and atmosphere can be minimized. The potential of both polarized and angular scattering coefficients, and their combinations for soil moisture sensing, were evaluated in detail.

4.2 Method

We investigated the bistatic scattering behaviour of soil moisture and surface roughness of bare soil surfaces. We generated our database by using the AIEM. For better understanding of the bistatic scattering characteristics of bare soil surfaces, we adopted single polarized simulations, a combination of dual polarized simulations, and a combination of dual angular simulations. To explore the sensitivity of bistatic scattering to soil moisture, we applied a defined sensitivity index (Brogioni et al., 2010).

Fig. 4.1 shows the bistatic scattering geometry. The incident angle θ_i represents the transmitter's angle, which is not necessarily co-located with the receiver. The scattering angle θ_s varies from 0° to 90°. The scattering azimuth angle φ_s flexibly changes from 0° to 360°. The incident azimuth angle is 0°.

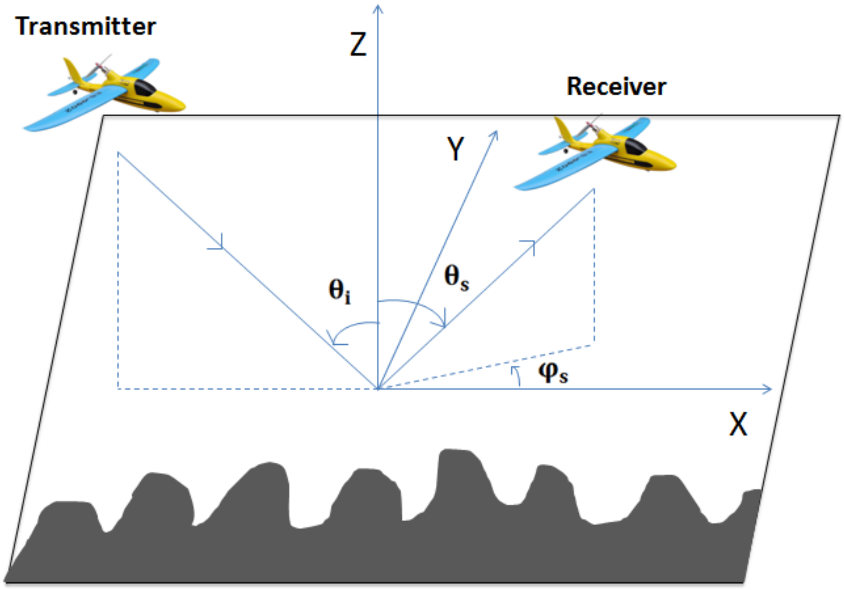

Figure 4.1 Geometry of bistatic scattering.

4.2.1 Random rough autocorrelation functions

The surface roughness is one of the main factors that affect the scattering of radar signals. A surface can be decomposed to a number of small-scale geometries.

Normally, we describe the small-scale geometry by the correlation length in the horizontal direction and the RMS height in the vertical direction. However, in addition to its correlation length and RMS height, the surface roughness is also characterized by an autocorrelation function (ACF). ACFs describe the interconnect degree between two points on the ground. In this study, we used three common correlation functions, namely the Gaussian, the 1.5-Power and the Exponential, to analyse the effect of ACFs on the bistatic scattering. These three ACFs can be expressed as:

I. Gaussian

$$W^{(n)}(k_{ix},k_{iy}) = \frac{s^2l^2}{4\pi n}\exp(-\frac{[k_{ix}^2+k_{iy}^2]l^2}{4n}) \tag{4.9}$$

II. 1.5-Power

$$W^{(n)}(k_{ix},k_{iy}) = \frac{s^2l^2(k_{ix}^2+k_{iy}^2)^{\frac{1.5n-1}{2}} J_{(1.5n-1)}(\sqrt{k_{ix}^2+k_{iy}^2})}{2\pi\cdot 2^{1.5n-1}\Gamma(1.5n)} \tag{4.10}$$

III. Exponential

$$W^{(n)}(k_{ix},k_{iy}) = \frac{s^2l^2}{2\pi n^2}(1+\frac{[k_{ix}^2+k_{iy}^2]l^2}{n^2})^{-1.5} \tag{4.11}$$

where J_n is the n^{th} order Bessel function, and Γ is the gamma function.

4.2.2 Sensitivity index

The sensitivity index used in our study is used to describe the sensitivity of the bistatic scattering coefficients to soil moisture as well as the surface roughness. The sensitivity index is defined below (Brogioni et al., 2010):

$$I_{sm} = \frac{\Delta\sigma_{sm}^{0}}{\Delta\sigma_{sm}^{0} + \Delta\sigma_{roughness}^{0}} \tag{4.12}$$

where $\Delta\sigma_{\mathrm{sm}}^{0}$ and $\Delta\sigma_{\mathrm{roughness}}^{0}$ represent the change of the absolute scattering coefficient caused by the change of soil moisture and surface roughness, respectively. I_{sm} is the sensitivity index, and its value is from 0 to 1. When the $\Delta\sigma_{\mathrm{roughness}}^{0}$ is far less than $\Delta\sigma_{\mathrm{sm}}^{0}$, then the I_{sm} is close to 1, which means the sensitivity of the bistatic scattering signals to soil moisture reaches its maximum. Where $\Delta\sigma_{\mathrm{sm}}^{0}$ and $\Delta\sigma_{\mathrm{roughness}}^{0}$ represent the change of absolute scattering coefficient caused by the change of soil moisture and surface roughness, respectively. I_{sm} is the sensitivity index, and its value is from 0 to 1. When the $\Delta\sigma_{\mathrm{roughness}}^{0}$ is far less than $\Delta\sigma_{\mathrm{sm}}^{0}$, then the I_{sm} is close to 1 which means the sensitivity of bistatic scattering signals to soil moisture reaches maximum. When I_{sm} is close to 0, that means the sensitivity is down to the minimum.

4.3 Results and discussions

In order to explore the response and sensitivity of bistatic scattering to soil moisture and surface roughness, we conducted an analysis in three parts, described in Sections 4.3.2 to 4.3.4. In addition, we fixed the correlation length (l=λ) in all cases owing to its lesser effect on the scattering coefficients as compared to the soil moisture and RMS height (Pierdicca et al., 2008). Furthermore, in the study, we focussed on the L-band (i.e. 1.26 GHz) as it shows good sensitivity to soil moisture, and the effects of vegetation and atmosphere can be minimized (Zeng et al., 2016b).

In the first part, we investigated the sensitivity of the co-polarized scattering to soil moisture and surface roughness. Firstly we investigated the changes in the bistatic pattern caused by soil moisture alone, with roughness remaining constant. Then, the converse was shown, where roughness changed while soil moisture remained constant. Last, a sensitivity index of soil moisture was developed based on the previous two steps. In the second part, we adopted a new scattering coefficient group (i.e.

combination of dual polarized simulations) to explore the sensitivity of the bistatic scattering to soil moisture and surface roughness. In the third part, we used a dual angle group to analyse the bistatic scattering characteristics.

4.3.1 Choice of polarization

Firstly, we investigated the sensitivity of HH and VV polarized scattering coefficients to soil moisture. The maximum bistatic scattering values (dB) of the co-polarization caused by the change of soil moisture are presented in Fig. 4.2. From Fig. 4.2 we can see that when the soil moisture changes by 2%, from wet to dry conditions, the radar responses are different. In the dry conditions, the radar signal varies much more than it does in the wet conditions. In addition, the differences between the HH and VV polarized scattering coefficients are larger for the rougher surface (*s*=λ/5).

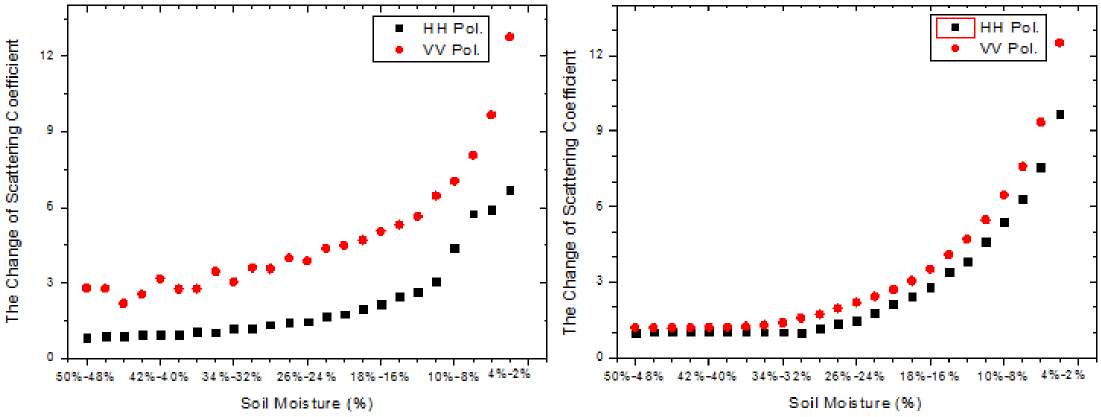

Figure 4.2 Variations of HH and VV polarized scattering coefficients with soil moisture for θ_i=40°, *l*=λ/2, and Exponential ACF (in the left s=λ/5, in the right *s*=λ/20).

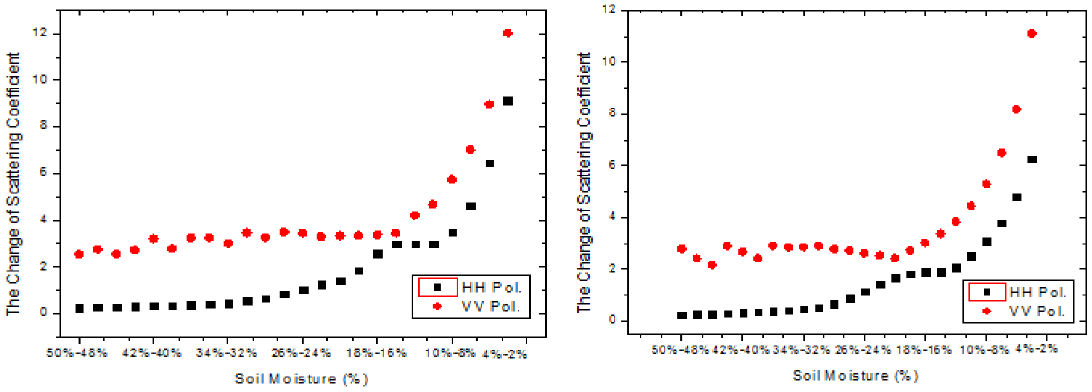

Figure 4.3 Variations of HH and VV polarized scattering coefficients with soil moisture for θ_i=40°, *s*=λ/10, and Exponential ACF (in the left *l*=λ/4, in right *l*=λ).

Meanwhile, we can see in Figure 4.2, we change the RMS height *s* from left figure to right figure, with cause an oblivious difference result between the two figures. However, in Figure 4.3, we also change the correlation length *l* , the differences between the left and right figure is minor. So that compare with Figure 4.2 and Figure 4.3, we can find out the RMS height *s* is more sensitive to the soil moisture change than the correlation length *l*.

In general, the bistatic scattering signals of VV polarization were found to be more sensitive to soil moisture than those of the HH polarization. The bistatic scattering signals of RMS height *s* also were found to be more sensitive to soil moisture than the correlation length *l*. Therefore, the following parts we all set the correlation length fixed and focus on the VV polarization.

4.3.2 Single polarized simulations

4.3.2.1 Sensitivity of HH and VV polarized scattering coefficient to soil moisture

As shown in Fig. 4.4, we investigated the bistatic sensitivity of different soil moisture levels of 5%, 25%, and 45%. In this case, the surface roughness was set as $s=\lambda/20$, $l=\lambda/2$ with Exponential ACF (corresponding to a smooth surface), and the incident angle was 40°. We can observe that with the increase of soil moisture, the scattering coefficients in the forward direction and the backward direction all increased. In the relatively dry conditions, the change of the scattering coefficients was larger than in the wet conditions.

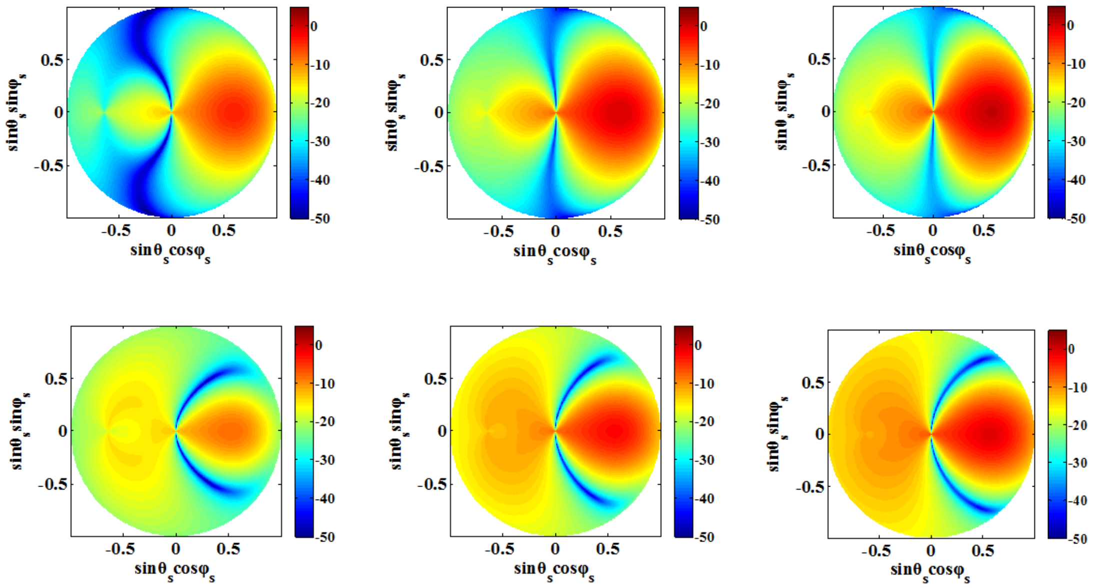

Figure 4.4 Bistatic scattering hemispherical plots of different soil moisture levels under smooth soil roughness conditions. The first row shows the HH polarization; the second row shows the VV polarization, all in dB. From left to right the soil moisture level is 5%, 25%, and 45%, respectively. All: L band (1.26 GHz), $s=\lambda/20$, $l=\lambda/2$, $\theta_i=40°$, Exponential ACF.

As shown in Fig. 4.5, we investigated the bistatic scattering response at different soil moisture levels (5%, 25%, and 45%). The difference between results illustrated in Fig. 4.4 and Fig. 4.5 is that in Fig. 4.4, the experiments were conducted under a smooth surface roughness condition, but in Fig. 4.5, the experiments were conducted under a rough surface roughness condition ($s=\lambda/5$, $l=\lambda/2$). Results show that, for both HH and VV polarizations, the scattering coefficient in the forward direction and the backward direction all increase with an increase in soil moisture. In general, the results of Fig. 4.5 are similar as those of Fig. 4.4, expect for increased scattering signals over the whole upper half space due to the rougher surface.

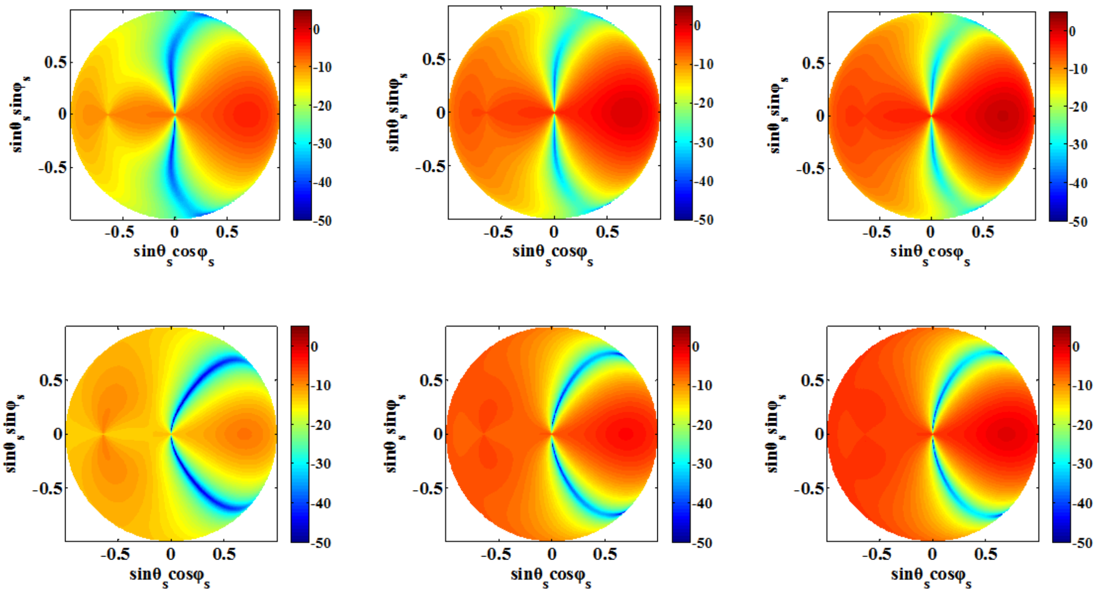

Figure 4.5 Bistatic scattering hemispherical plots of different soil moisture under rough soil roughness conditions. The first row shows the HH polarization; the second row shows the VV polarization, all in dB. From left to right the soil moisture level is 5%, 25%, and 45%, respectively. All: L band (1.26 GHz), *s*=λ/5, *l*=λ/2, *θi*=40°, Exponential ACF.

4.3.2.2 Sensitivity of HH and VV polarized scattering coefficient to soil roughness

We next investigated the bistatic scattering response with different RMS height (i.e. *s*=λ/20, *s*=λ/10, and *s*=λ/5), shown in Figure 4.6. In this case, the soil moisture was set as *mv*=5% (corresponding to a dry soil condition), *l*=λ/2 with Exponential ACF, and the incident angle was 40°. Results show that, for both HH and VV polarizations, the scattering coefficient in the forward direction and the backward direction all increased with the increase of the soil roughness. Different from the results shown in Figs. 4.4 and 4.5 where the scattering signals were nearly saturated under the wet soil condition, in this case the scattering coefficient does not reach saturation from the smooth surface to the rough surface.

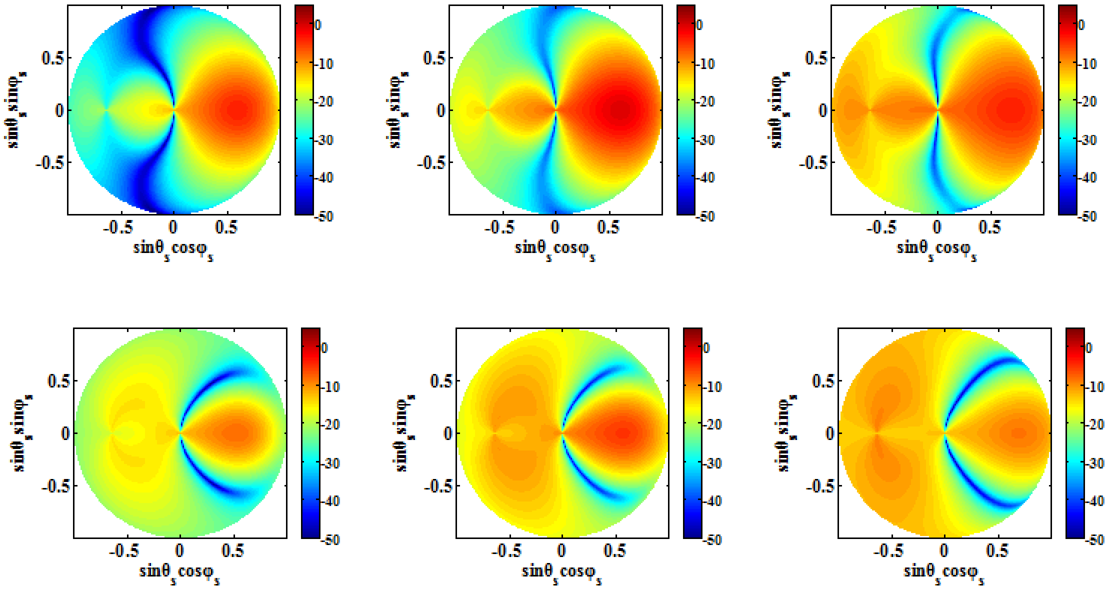

Figure 4.6 Bistatic scattering hemispherical plots of different soil roughness in dry soil moisture conditions. The first row shows the HH polarization; the second row shows the VV polarization, all in dB. From left to right the RMS height is $s=\lambda/20$, $s=\lambda/10$, and $s=\lambda/5$, respectively. All: L band (1.26 GHz), $mv=5\%$, $l=\lambda/2$, $\theta i=40°$, Exponential ACF.

As shown in Fig. 4.7, we investigated the bistatic scattering response at different levels of soil roughness in a manner similar to the situation illustrated in Fig. 4.6 except under wet rather than the dry soil conditions. A similar bistatic scattering behaviour can be observed in Fig. 4.7. However, under the relatively wet soil conditions, the changes in the scattering coefficient caused by the surface roughness are not as large as those of the scattering coefficient under the dry soil conditions.

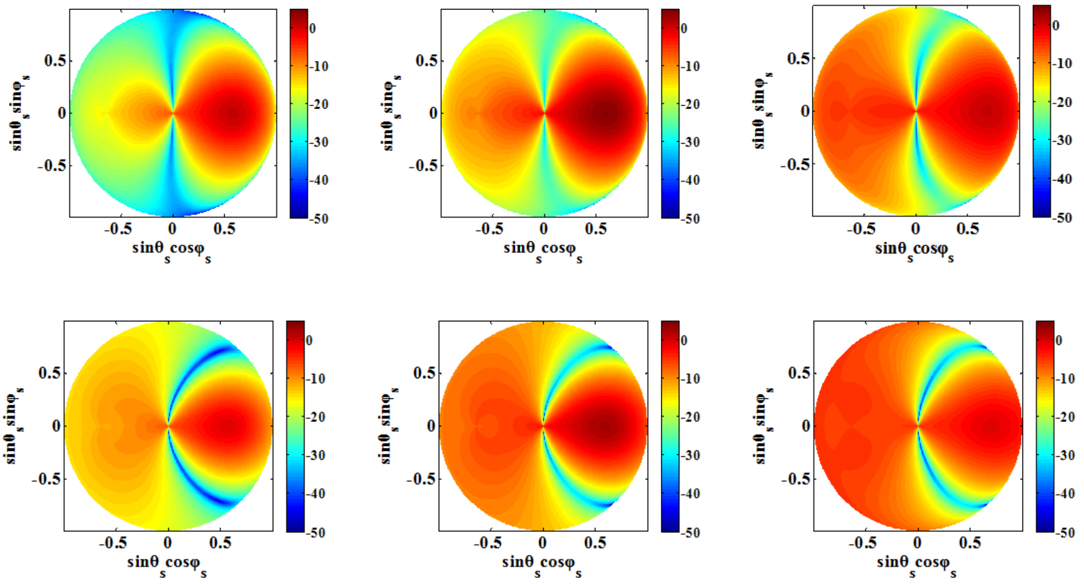

Figure 4.7 Bistatic scattering hemispherical plots of different soil roughness under wet soil conditions. The first row shows the HH polarization; the second row shows the VV polarization, all in dB. From left to right the RMS height is $s=\lambda/20$, $s=\lambda/10$, and $s=\lambda/5$, respectively. All: L band (1.26 GHz), mv=45%, $l=\lambda/2$, $\theta i=40°$, Exponential ACF.

4.3.2.3 Sensitivity of single polarized scattering coefficient to soil moisture and soil roughness

Firstly, we investigated the changes in absolute values of the scattering coefficients caused by changes in soil moisture ($\triangle\sigma_{pp} = |\sigma_{pp}(mv=45\%)-\sigma_{pp}(mv=5\%)|$), as shown in Fig. 4.8. It can be clearly seen that with the change of soil moisture, the bistatic scattering pattern is nearly the same under the different ACFs. For HH polarizations, the bistatic scattering signal changes a lot in the backward directions. For VV polarizations, the most sensitive region for soil moisture is in the forward direction.

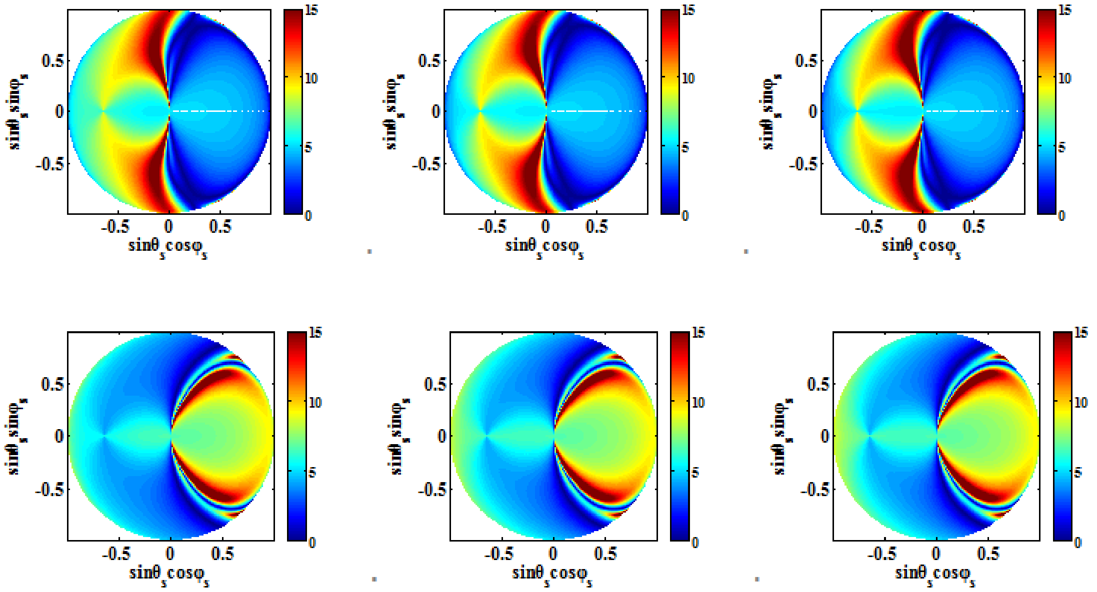

Figure 4.8 Bistatic scattering hemispherical plots of variations of σ^0_{HH} and σ^0_{VV} with soil moisture ranging from 5% to 45%. The first row shows the HH polarization; the second row shows the VV polarization, all in dB. Gaussian, 1.5-Power and Exponential ACF results are shown from left to right, respectively. All: L band (1.26 GHz), RMS height $s=\lambda/10$, $l=\lambda/2$, $\theta i=40°$.

As shown in Figure 4.9, we investigated the changes in absolute values of the scattering coefficients caused by changes in soil roughness ($\triangle\sigma_{pp} = |\sigma_{pp}(s=\lambda/5)-\sigma_{pp}(s=\lambda/20)|$). It can be seen that when the soil roughness changes, the bistatic scattering pattern is different under different ACFs. This is more evident with the Gaussian correlated surface than with the Exponential or the 1.5-Power correlated surface in this case. For HH polarizations, the bistatic scattering signal changes a lot in the backward directions. For VV polarizations, the bistatic scattering signal is not sensitive to the change of soil roughness especially in the forward direction.

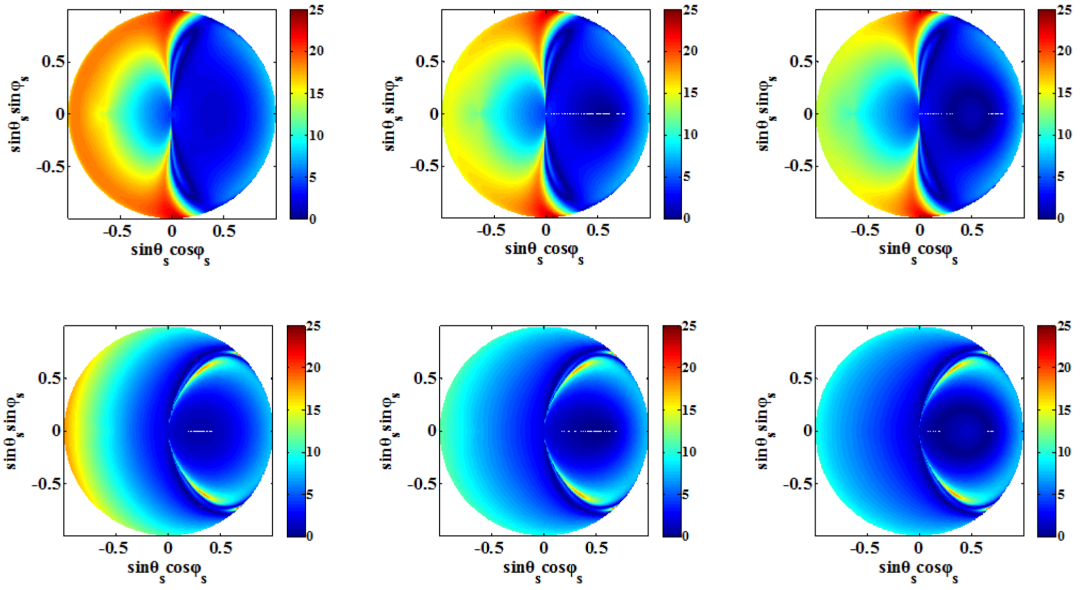

Figure 4.9 Bistatic scattering hemispherical plots of variations of σ^0_{HH} and σ^0_{VV} with soil roughness change from with RMS height from $s=\lambda/5$ to $s=\lambda/20$. The first row shows the HH polarization; the second row shows the VV polarization, all in dB. Gaussian, 1.5-Power and Exponential ACF results are shown from left to right, respectively. All: L band (1.26 GHz), mv=0.25, $l=\lambda/2$, θi=40°.

4.3.2.4 Analysis of sensitivity index of soil moisture

As previously discussed in Section 4.2.1, we obtained a sensitivity index of soil moisture. The results are shown in Fig. 4.10. We can observe that, for both HH and VV polarizations, the area that is most sensitive to soil moisture is in the forward direction. However, the general pattern of the sensitivity index is different with the different ACFs. This indicates that the influence of the ACF cannot be ignored when using single polarized scattering coefficients for soil moisture estimation.

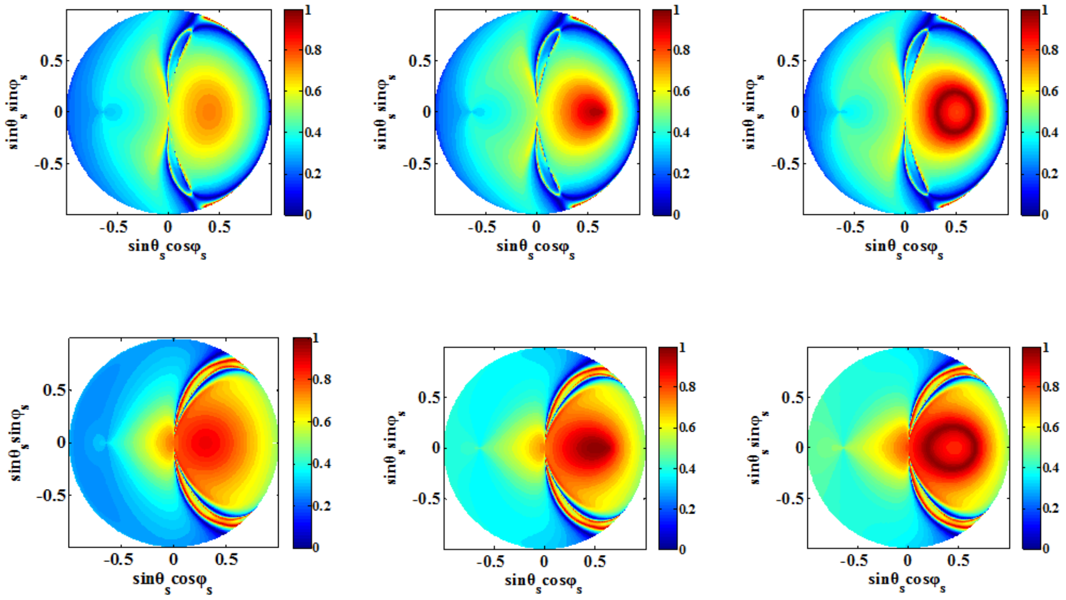

Figure 4.10 Bistatic scattering hemispherical plots of sensitivity index of soil moisture. The first row shows the HH polarization; the second row shows the VV polarization, all in dB. Gaussian, 1.5-Power and Exponential ACF results are shown from left to right, respectively. All: L band (1.26 GHz), $l=\lambda/2$, $\theta i=40°$.

4.3.3 Combination of dual polarized simulations

4.3.3.1 Dual polarized simulations of soil moisture

In previous studies, some researchers (Brogioni et al., 2010; Zeng et al., 2016) adopted a combination of dual polarized simulations to investigate the radar response of bistatic scattering to soil moisture and surface roughness. To further investigate the potential of combining dual polarized measurements for soil moisture estimation, a sensitive analysis similar to that illustrated in Fig. 4.8, but for the ratio $\sigma^0_{HH}/\sigma^0_{VV}$ (i.e. $\sigma^0_{HH}-\sigma^0_{VV}$ in dB), was conducted such that ($\triangle\sigma_{HH/VV} = |\triangle\sigma_{HH/VV}$ (mv=45%)-$\triangle\sigma_{HH/VV}$ (mv=5%)|. These results are shown in Fig. 4.11 where it can be seen that the scattering coefficient is very sensitive to the soil moisture in both the backward and forward directions. Moreover, the bistatic scattering pattern is very similar under different ACFs.

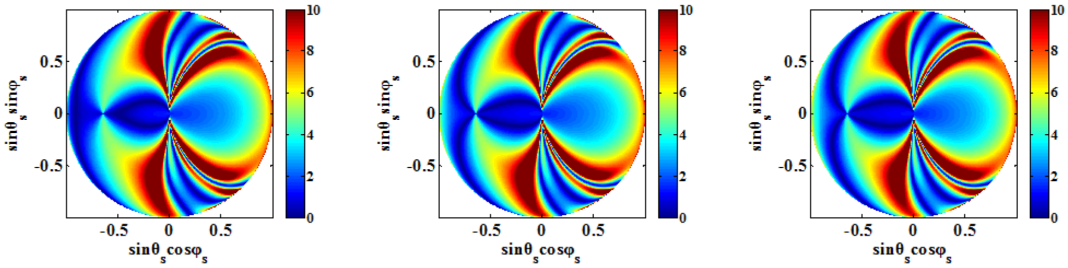

Figure 4.11 Bistatic scattering hemispherical plots of variations of $\sigma^0_{\mathrm{HH}}(\mathrm{dB}) - \sigma^0_{\mathrm{VV}}(\mathrm{dB})$ with soil moisture ranging from 5% to 45%. Gaussian, 1.5-Power and Exponential ACF results are shown from left to right, respectively. All: L band (1.26 GHz), l=λ/2, θi=40°. The colorbar is in dB.

4.3.3.2 Dual polarized simulations of surface roughness

Similar to the results shown in Fig. 4.10, we also investigated the variations of σ^0_{VV} (dB)-σ^0_{HH} (dB) with surface roughness ranging from λ/20 to λ/5 (σ $_{\mathrm{HH/VV}}$ = |σ $_{\mathrm{HH/VV}}$ (s=λ/5) - σ $_{\mathrm{HH/VV}}$ (s=λ/20)). These results are shown in Fig. 4.12. It can be clearly observed that the scattering coefficients are not sensitive to the surface roughness in the forward direction. In addition, the influence of ACFs on the dual polarized simulation are well suppressed.

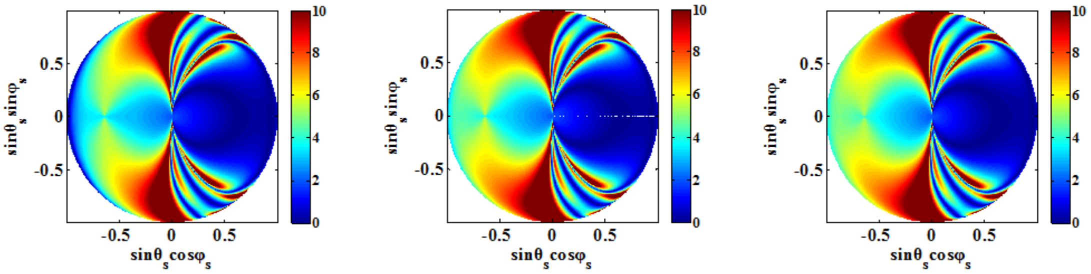

Figure 4.12 Bistatic scattering hemispherical plots of s variations of $\sigma^0_{\mathrm{HH}}(\mathrm{dB}) - \sigma^0_{\mathrm{VV}}(\mathrm{dB})$ with surface roughness ranging from $\lambda/20$ to $\lambda/5$. Gaussian, 1.5-Power and Exponential ACF results are show from left to right, respectively. All: L band (1.26 GHz), l=λ/2, θi=40°. The colorbar is in dB.

4.3.3.3 Dual angular simulations of sensitivity index

In this part, we obtained the sensitivity index of soil moisture (index$_{sm}$= σ $_{HH/VV}$ (△SM) / (σ $_{HH/VV}$ (△SM) + σ $_{HH/VV}$ (△Roughness))). These results are shown in Fig. 4.13. Here we see that the most sensitive area is in the forward direction. Moreover, using the combined dual polarized measurements suppressed the influence of the ACFs. Although the index is high, we should note that the scattering coefficient changes by the soil moisture are not large, as can be seen in Fig. 4.10.

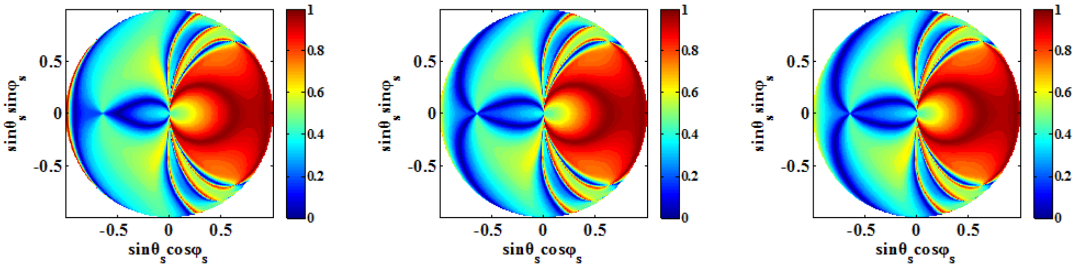

Figure 4.13 Bistatic scattering hemispherical plots of sensitivity of $\sigma^0_{HH}(\mathrm{dB}) - \sigma^0_{VV}(\mathrm{dB})$ to soil moisture. Gaussian, 1.5-Power and Exponential ACF results are shown from left to right, respectively. All: L band (1.26 GHz), $l=\lambda/2$, $\theta i=40°$.

4.3.4 Dual angular simulations analysis

4.3.4.1 Dual angular simulations of soil moisture

In previous studies, Zeng et al. (2016b) found that a combination of dual angular measurements shows good sensitivity to soil moisture, while the influence from the ACF is well suppressed. In order to find the optimal bistatic angular combination for soil moisture sensing, we conducted four groups of combined dual angle which were as follows: θ_i=20° and θ_i=30°, θ_i=20° and θ_i=40°, θ_i=20° and θ_i=50°, and θ_i=20° and θ_i=60°. An example of the combination of dual angular scattering is the ratio $\sigma^0_{VV,\theta_i=20i}/\sigma^0_{VV,\theta_i=30i}$.

In addition, from Sections 4.3.1 and 4.3.2, we found that the bistatic scattering signals of VV polarization were more sensitive to soil moisture than those of the HH polarization. Therefore the following parts all focus on the VV polarization. Fig. 4.14 shows that when the soil moisture changes from 5% to 45% in VV polarization, the forward direction is more sensitive to changes in soil moisture.

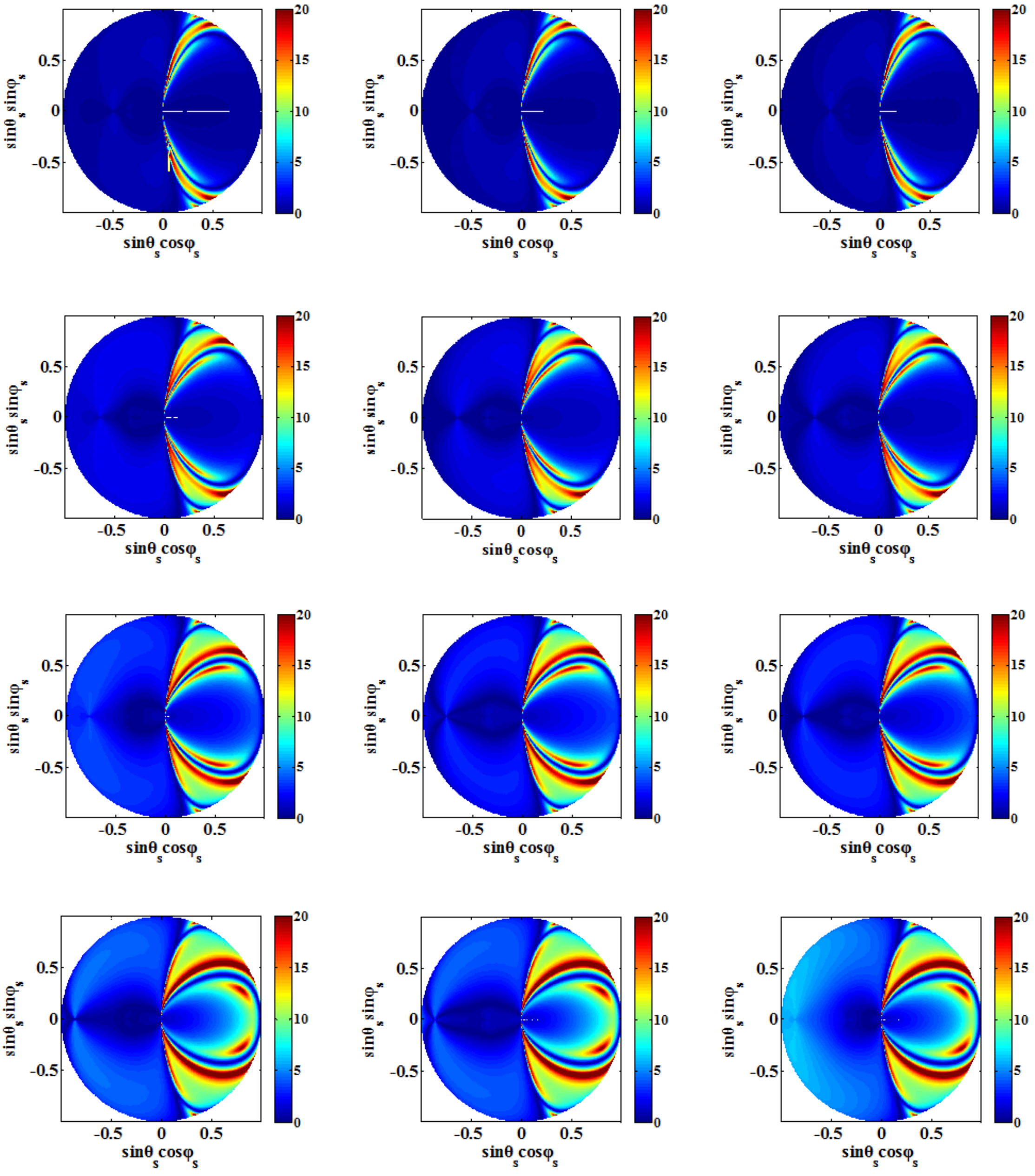

Figure 4.14 Bistatic scattering hemispherical plots of variations of $\sigma^0_{VV,\theta_{i1}}/\sigma^0_{VV,\theta_{i2}}$ with soil moisture ranging from 5% to 45%. Gaussian, 1.5-Power and Exponential ACF receptivity results are shown from left to right, respectively. All: $s=\lambda/10$, $l=\lambda/2$. The colorbar is in dB.

We can see that the patterns of bistatic scattering as soil moisture changes are nearly the same under the three kinds of ACF. Moreover, it can be observed that as the difference of the dual angle increases, the sensitivity of the combined angular measurements to soil moisture also increases.

4.3.4.2 Dual angular simulations of soil roughness

In this part, we investigated the response of dual angular simulations to the soil roughness. Here we changed the RMS height from λ/5 to λ/20 while keeping the remaining parameters fixed (soil moisture=25%, l=λ/2). Results are shown in Fig. 4.15. It can be easily seen that the influences of the ACF on the dual angular simulation were well suppressed. This indicates that the combined scattering measurements can be approximately treated as independent of the ACFs. From Fig. 4.15 we can see that, compared to the soil moisture, the bistatic scattering responses are less sensitive to the surface roughness, which is useful information for soil moisture estimation. Furthermore, it can be seen that as the difference of the dual angle increases, the sensitivity of combined angular measurements to surface roughness is almost the same or even decreases.

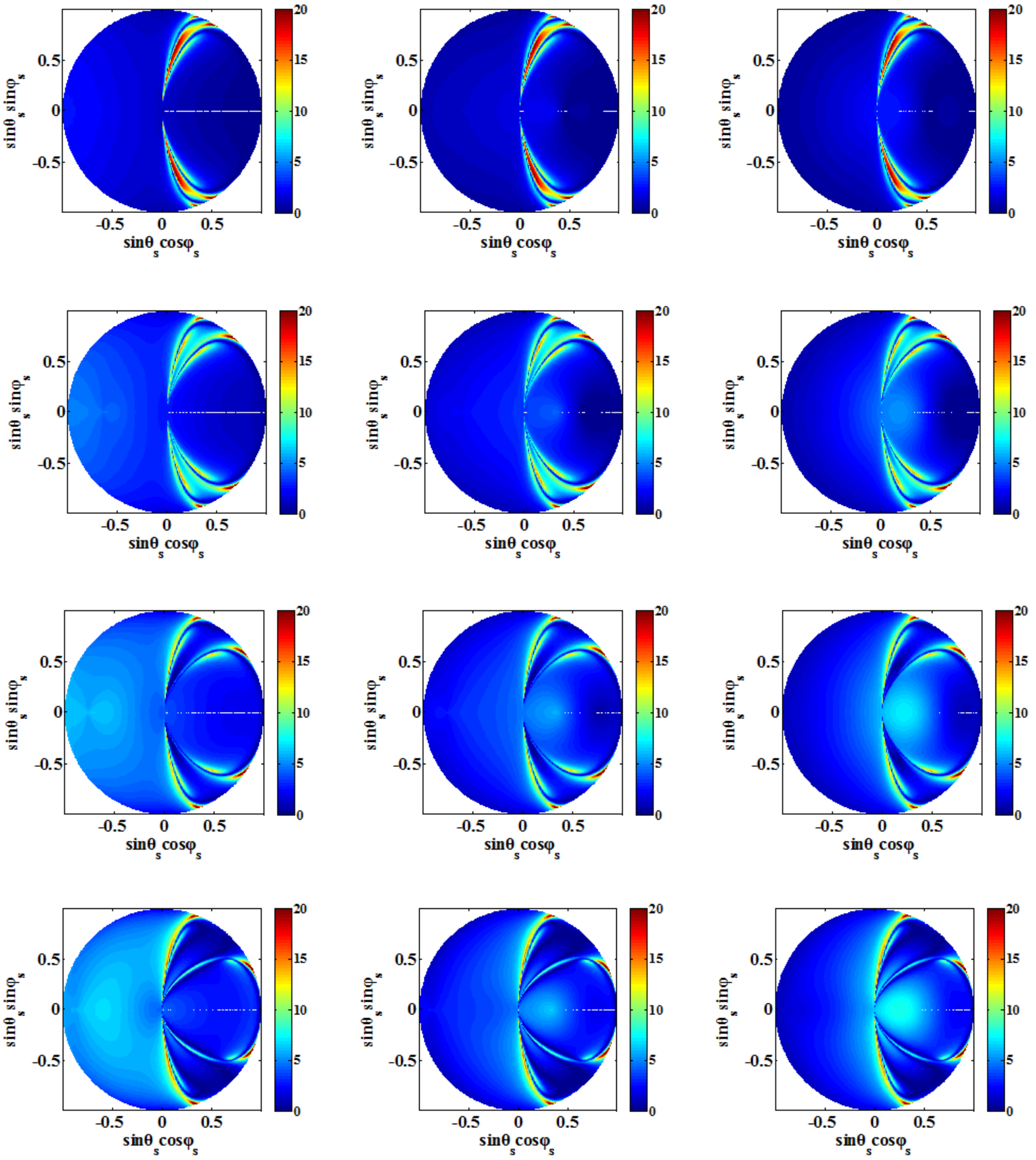

Figure 4.15 Bistatic scattering hemispherical plots of variations of $\sigma^0_{VV,\theta_{i1}}/\sigma^0_{VV,\theta_{i2}}$ with RMS height ranging from $\lambda/5$ to $\lambda/20$. Gaussian, 1.5-Power and Exponential ACF receptivity results are shown from left to right, respectively. All: soil moisture=25%, $l=\lambda/2$. The colorbar is in dB.

4.3.4.3 Dual angular simulations of sensitivity index

In Sections 4.3.4.1 and 4.3.4.2 we investigated the sensitivity of bistatic scattering to soil moisture and soil roughness, respectively. As we stated in the beginning, the aim of this study is to predict the suitable bistatic radar configuration for soil moisture retrieval. So we adopted the sensitivity index in our study. The results are shown in Fig. 4.16.

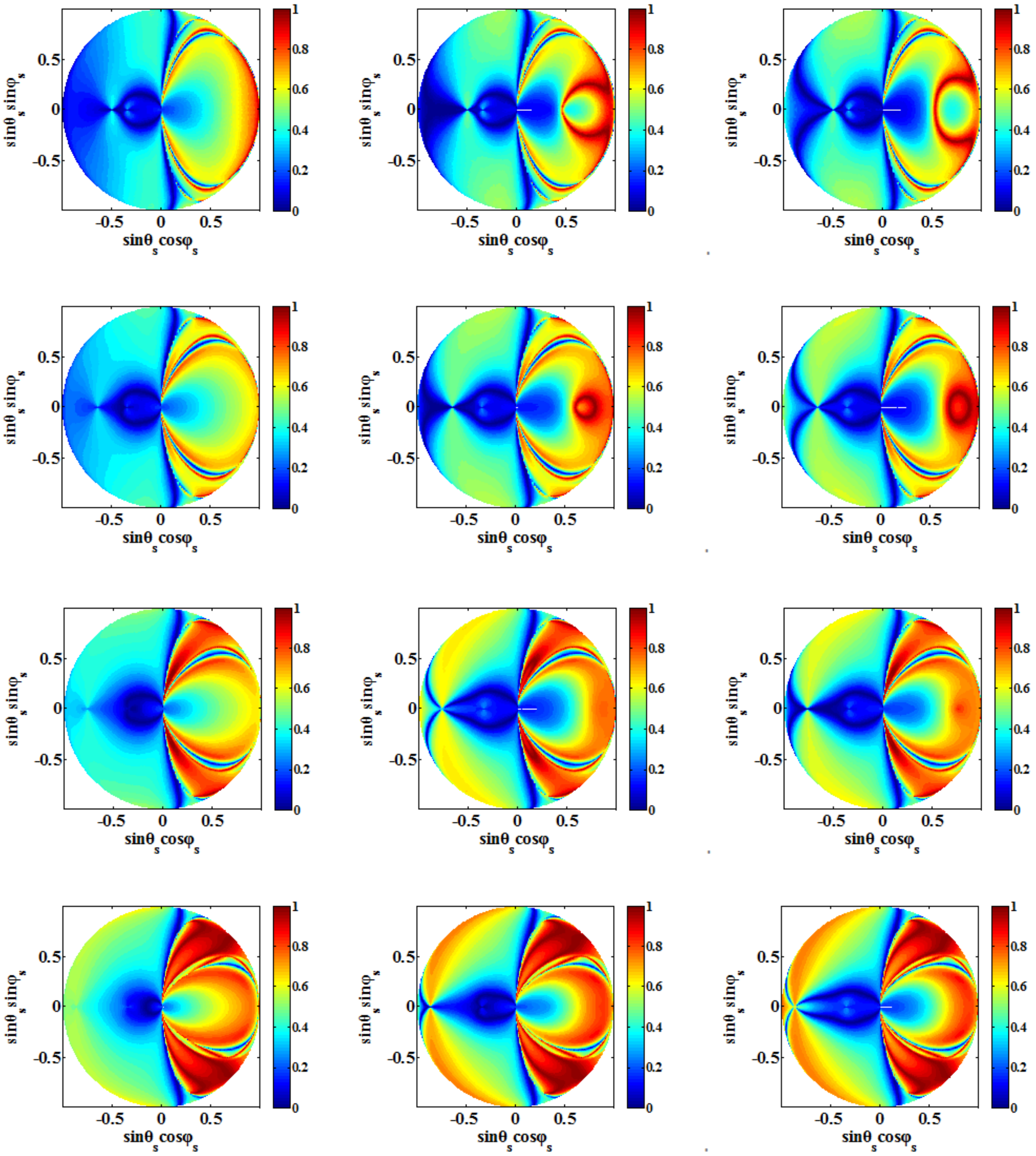

Figure 4.16 Bistatic scattering hemispherical plots of sensitivity of $\sigma^0_{VV,\theta_{i1}}/\sigma^0_{VV,\theta_{i2}}$ to soil moisture ranging between 5% and 45%. Gaussian, 1.5-Power and Exponential ACF receptivity results are shown from left to right, respectively. All: $l=\lambda/2$. The colorbar is in dB.

From Fig. 4.16, we can observe that the bistatic patterns of different combinations are generally similar. It is clearly shown that, in the forward region, there are large areas where the value is close to 1. In addition, with the increase of the difference between the two incident angles, the sensitive area becomes larger, and the effects of the three ACFs on the bistatic scattering coefficients are further suppressed. This indicates that, in our experiments, the 20° and 60° group is the most suitable angular combination compared with the other three groups.

4.4 Conclusions

Remote sensing of soil moisture in a bistatic mode has attracted increasing attention in recent years. Systematic simulation of bistatic scattering behaviours from a rough surface offers physical insights into designing bistatic radar configurationes and field campaigns. The research reported in this chapter investigated the radar response of bistatic scattering to soil moisture and surface roughness by using the AIEM. In order to find the optimal bistatic configuration for soil moisture estimation, we adopt a sensitivity index. The results show that the VV polarized scattering coefficient is more sensitive to soil moisture than that of the HH polarized scattering coefficient. The most sensitive area to soil moisture under a bistatic configuration is in the forward direction. Compared to the results from single polarized and combined dual polarized data, the combination of dual angular observation proves to be a good choice for soil moisture estimation since it suppresses the influence of thee ACF while maintaining a good sensitivity to soil moisture. Furthermore, it seems that as the difference of the dual angle increases, the sensitivity of combined angular measurements to the soil moisture also increases.

Chapter 5 Development of a recurrent Kalman filter-based neural network for soil moisture retrieval using ALOS-2 satellite data

5.1. Motivation

Radar remote sensing is a kind of active microwave remote sensing technology for detecting and ranging. It uses radio electromagnetic waves, which applies to the microwave spectrum: The usage range is between 1 cm and 100 cm. The earliest radar system of this type was used for military research to detect hard targets (usually a metal point target). While these radar systems couldn't produce images, following radar remote sensing systems of earth observation were able to rank surface features and landforms as detecting targets. Real aperture radar (RAR) is the earliest imaging radar system and its azimuth resolution is limited by antenna size. With deeper explorations through theoretical research, signal processing, antenna design, and the development of computer software and hardware, the synthetic aperture radar (SAR) was developed, which gradually replaced RAR. SAR is a kind of high-resolution coherent combination imaging radar. It combines pulse compression technology with synthetic aperture technology through information processing technology. Specifically, this means that it uses space borne aircraft and precession of planes to create synthetic apertures. SAR takes advantage of various antenna echo signals for various positions during flight to make large-aperture antenna systems with finer resolution (Argenti et al., 2013; Moreira et al., 2013).

This dissertation research used microwave bands to study soil features. Its mechanism was self-rotation and rotation of molecules of matter, and the interaction between self-rotation of electron and transmitted electromagnetic waves which decides the inherent interaction mechanism between surface features and the imaging radar used in the microwave spectrum. A radar image reflects the interaction between electromagnetic waves transmitted by radar and surface feature objectives. The electromagnetic waves transmitted by the radar sensors reveal electrical currents on the surface of targets. Through radiation, incidence electromagnetic waves and detecting targets interact in the far-field region of the antenna, which produces scattering electromagnetic waves and which changes amplitude, frequency, phase position, polarization mode and other parameters of echo. The quality of a scattering wave is different from that of an incidence wave: It includes physical structure information about targets, which is a carrier of target information. This is caused by the modulation effect of targets on incidence electromagnetic waves. The modulation effect is decided by the physical structure features of targets. Different targets have different modulation features on the same incidence wave. Radar remote sensing extracts feature parameters of detecting targets according to modulation feature variance, i.e. that different targets affect electromagnetic waves differently. The basic measured value of each pixel for an image is a pair of voltage values. These measured values indicate the impact of surface information on the transmitted wave, which essentially describes Maxwell space spread and the equation of scattering characteristic equation. The radar equation can show the relationships among radar system, detecting target and received signals.

Some typical surface microwave scattering models are the Oh model, the Dubois model and the AIEM. However, the Oh model is not recommended as it has large errors in the analogue value of co-polarization scattering data, although it can simulate the cross-polarization scattering characteristics. The Dubois model has a different response to the actual situation (change of incident angle and the dielectric constant) because it is a kind of empirical model that lacks physical theory support. As we introduced in the previous chapters, the AIEM has high accuracy compared to simulations and field measurements and thus was adopted as a working model in this research. Analysing the radar characteristics by AIEM could help us better understand the radar backscattering features.

In the research reported in this chapter, we analysed the radar backscattering response of soil moisture and, to test with real-world data, developed a method for retrieving soil moisture from Advanced Land Observing Satellite-2 (ALOS-2) imagery. However, retrieval of soil moisture from SAR data is not as straightforward as it might be, since it is profoundly affected by surface roughness, vegetation cover, and soil texture, among other factors. The AIEM was again used to simulate the radar scattering characteristics of the soil surface to analyse the coupling effects of the surface parameters, including the RMS height, correlation length, and soil moisture as well as the radar system parameters, including the incident angle and polarization. Furthermore, in order to retrieval soil moisture from SAR images, we developed a recurrent Kalman filter-based neural network and tested this method by using the ALOS-2 data. The details are described below.

5.2 Sensitivity analysis of forward model parameters

To gain a good understanding of the surface scattering mechanism, we analysed the backscattering properties of bare surfaces by using the AIEM. The surface roughness is usually described with the correlation function and two parameters: root-mean-square (RMS) height (*s*) and the correlation length (*l*). In this section, our investigation of the radar response of backscattering coefficients to the geophysical parameters (e.g. soil moisture, RMS height and correlation length) and radar system parameters (e.g. frequency and incident angle) is discussed.

5.2.1. Scattering signal changes by various of frequencies

In this part, the radar response of backscattering signals to soil moisture at different frequencies is investigated. Results are shown in Fig. 5.1. In this case using the Exponential ACF the incident angle is 40°, the RMS height is 1 cm, the correlation length is 5 cm, and the soil moisture changes from 1% to 50%.

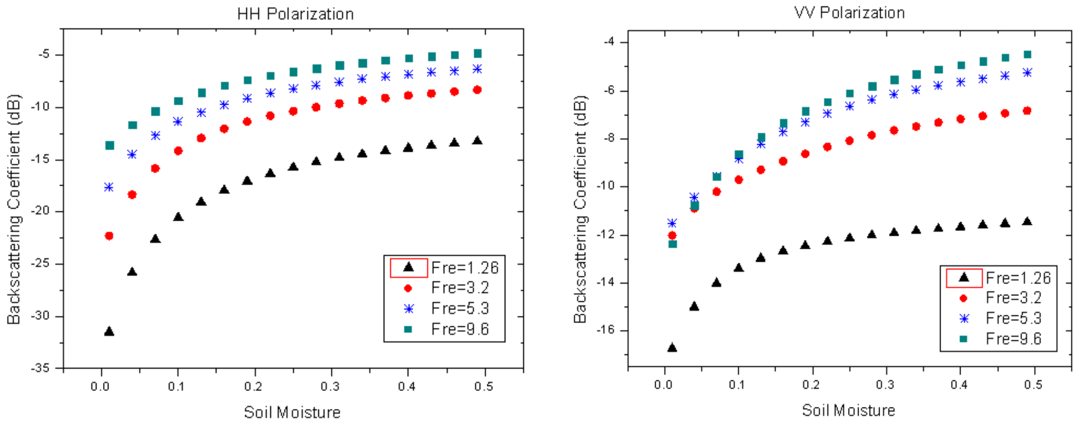

Figure 5.1 Backscattering behaviour of different frequencies with HH and VV polarizations for s=1 cm, l=5 cm, θi=40°, Exponential ACF.

As can be seen from Fig. 5.1, the backscattering coefficient changed the most with the changes of soil moisture at the L-band (i.e. 1.26 GHz). As the soil moisture increased, the backscattering coefficient monotonically increased. To sum up, the backscattering coefficient at 1.26 GHz shows the most sensitivity to soil moisture than at other frequencies. Thus, we fixed the frequency as 1.26 GHz in the following parts.

5.2.2. Scattering signal changes by various of angles

The different SARs usually configure diverse observation angles. The same SAR may also observe the target with different incident angles. Even in one radar image the incident angle along the direction of the distance also can be different.

In this part, we analysed the relationship between the backscattering coefficient and the incident angle as the soil moisture changed.

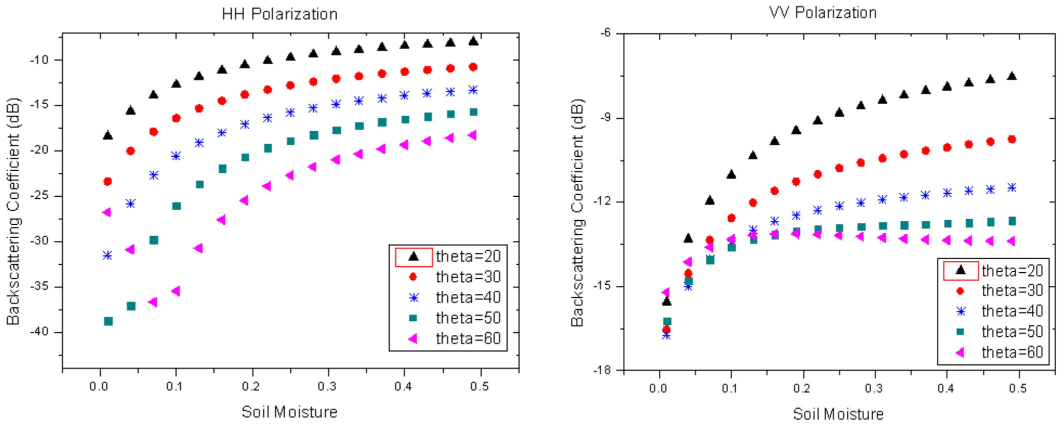

Figure 5.2 Backscattering behaviour of different incident angles with HH and VV polarizations for L band (1.26 GHz), s=1 cm, l=5 cm, Exponential ACF.

We can see from Fig. 5.2 that when the soil moisture changed from 1% to 20%, the backscattering coefficient appears as a different trend, as a change of incident angle. When the incident angle was less than 60 degrees, the backscattering coefficient increased as the soil moisture increased at both HH and VV polarizations. Thus, generally, the backscattering coefficient is larger when the incident angle is smaller.

5.2.3. Scattering signal changes by various of RMS height

In this section and the next section, we present the backscattering behaviour of various surface roughness conditions. In order to evaluate the impact of the RMS height on backscattering signals, we set the RMS height to five different levels: s=0.1, 0.5, 1, 1.5, and 2 cm while fixing the frequency at 1.26 GHz, correlation length equal to 5 cm with Exponential ACF, and soil moisture changes from 1% to 50%. Results are shown in Fig. 5.3.

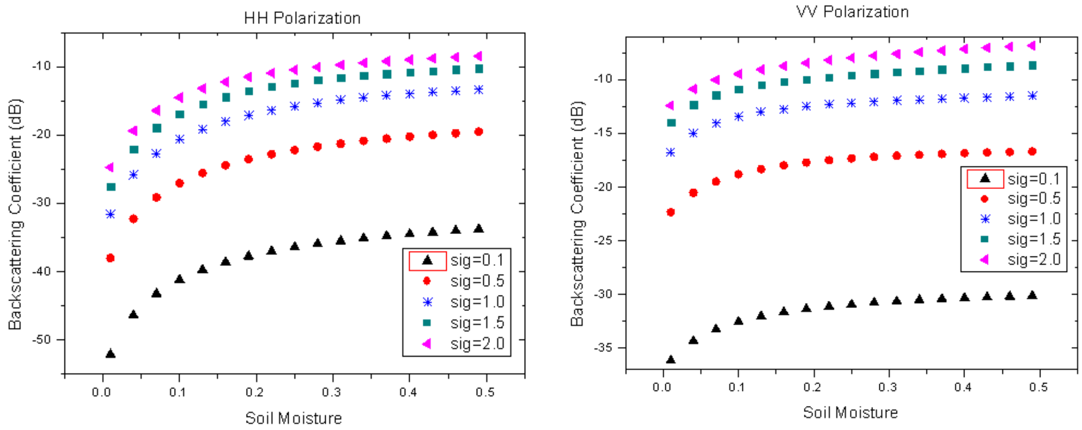

Figure 5.3 Backscattering behaviour of different RMS height with HH and VV polarizations for L band (1.26 GHz), *l*=5 cm, *θi*=40°, Exponential ACF.

In Fig. 5.3, all the curves have a similar trend at both HH and VV polarizations. With increase of the soil moisture, the backscattering coefficient increased under different RMS heights. It can also be observed that when the RMS height increased, the differences of the backscattering coefficient became smaller.

5.2.4 Scattering signal changes by various of correlation length

Fig. 5.4 illustrates the effect of different correlation lengthes on the backscattering coefficient as soil moisture increases. In this case, we set the frequency at 1.26 GHz, RMS height equal to 1 cm with Exponential ACF, and soil moisture changes from 1% to 50%. The general trends were found to be similar for both HH and VV polarizations. We can see that large correlation length caused few differences for the backscattering coefficient; when the correlation length was greater than 3 cm, the curves became almost indistinguishable. Thus, we can conclude that the sensitivity of the backscattering coefficients to the correlation length is larger when the correlation length is smalleer.

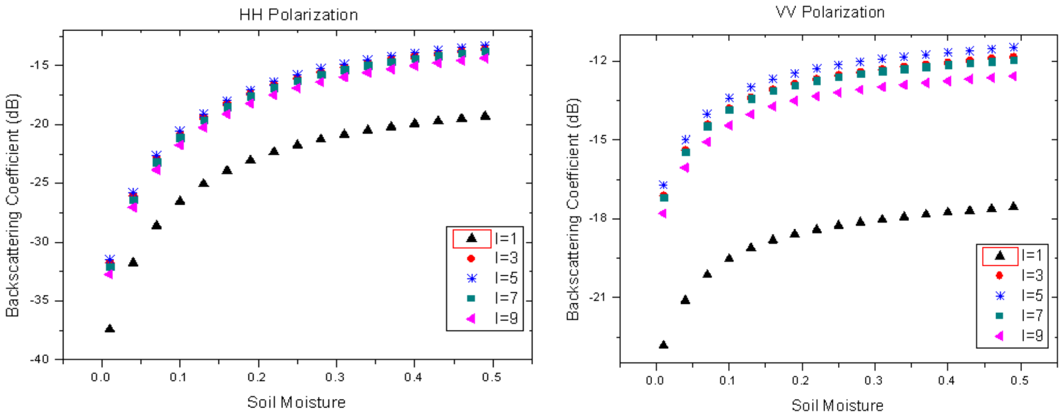

Figure 5.4 Backscattering behaviour of different correlation length with HH and VV polarizations for L band (1.26 GHz), *s*=1 cm, *θi*=40°, Exponential ACF.

5.3 Methodology

5.3.1 The retrieval method

In this research, we used a retrieval method based on a dynamic learning neural network and the AIEM to build the relationship between the soil moisture, surface roughness and the backscattering coefficient. Inversion methods commonly used, such as those discussed above, have been developed to extract only a single parameter. However, the return signals from a natural soil surface are affected simultaneously by many surface parameters, such as RMS height, correlation length, and dielectric constant of soil. To solve the problems of multidimensional retrieval, a recurrent Kalman filter-based neural network method was developed due to its ability to adapt the high geophysical dimensions, its robustness to noise in realistic remote sensors, and, most importantly, is capability of handling nonlinear mapping. Fig. 5.5 shows a flowchart of this recurrent Kalman filter-based neural network method.

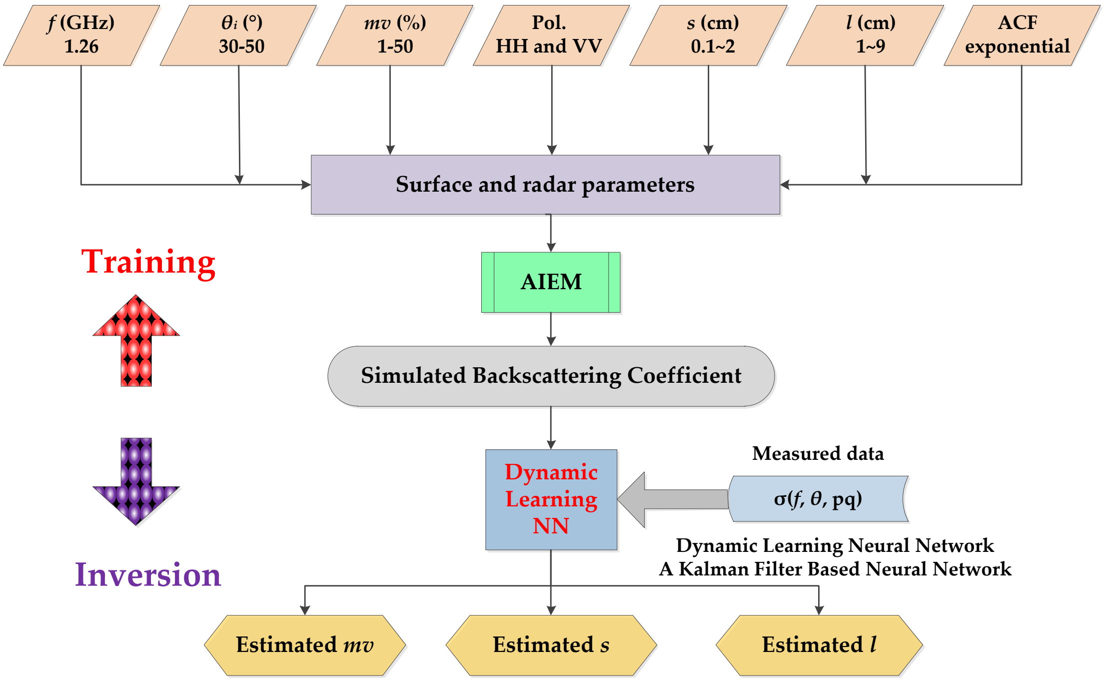

Figure 5.5 Flowchart of the recurrent Kalman filter-based neural network method.

Essentially, the operation could be divided into two phases. The first phase was network training – to build the mapping function. We used the AIEM model to generate a training database by configuring radar parameters (i.e. frequency, incident angle, and polarization) and setting surface parameters (i.e. soil moisture, RMS height, correlation function, and correlation length) confined in a practical range. After completing the network training, we proceeded to the second phase, relevant neural network operations, namely the retrieval of soil moisture. By using the generated database to train the Kalman filter-based neural network, we obtained the relationship between the backscattering coefficients and the soil moisture, correlation length and RMS height. For the retrieval process in this work, the outputs of the neural network were the roughness parameters (correlation length and the RMS height) and the soil moisture. The inputs of the neural network were the backscattering coefficients at both HH and VV polarizations (σ^{0}_{hh} and σ^{0}_{vv}). Furthermore, we verified the retrieval results with simulated data, which were not included in the training database. Finally, we applied our method to SAR images to retrieve the soil moisture.

5.3.2 Generation of DLNN training data using AIEM

5.3.2.1 Dynamic learning neural network

Tzeng et al. (1994) proposed a dynamic learning neural network (DLNN) to reduce the drawbacks of the slow learning process that was inherently associated with the above training schemes. A dynamic learning neural network has the advantages of greatly reduced training times and increased accuracy. This has been demonstrated in many applications (Chen et al., 1995). A neural network has the advantage of inverting the surface parameters effectively (Dawson et al., 1992; Tsang et al., 1992). The objective of our study was to simultaneously retrieve surface roughness and soil moisture, as shown in Fig. 5.6, so we exploited the Kalman filter-based dynamic learning algorithm (Tzeng et al., 1994). The Kalman filter theory is a procedure that recursively estimates the minimum mean square (Brown and Hwang, 1983).

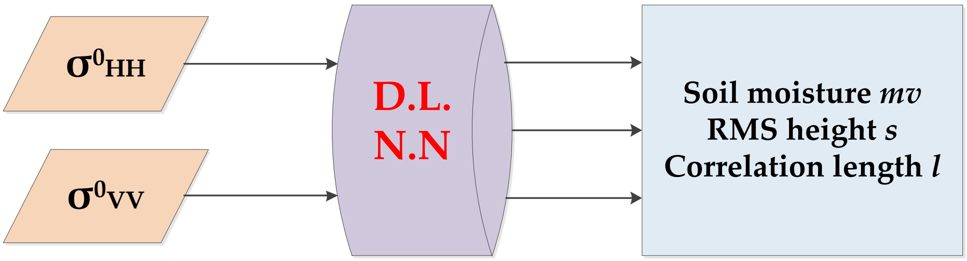

Figure 5.6 Input and output of the neural network for the inversion process.

5.3.2.2 The results of fixing the incident angle

Parameters which needed to be estimated included surface roughness in both the horizontal and vertical scales (i.e. RMS height and correlation length) and the dielectric constant which, in turn, were related to other geophysical quantities of interest such as the moisture content of the soil. The co-polarized backscattering coefficients were used as the inputs of the inversion scheme.

The training of a neural network begins by defining the network inputs and outputs that are controlled by the type of applications. For the inversion problem shown in this work, the output of the network should be the soil moisture and the two roughness parameters, i.e. *l* (the correlation length) and *s* (the RMS height). The range of each parameter used to generate training database is shown in Table 5.1.

Table 5.1 The range of each parameter used to generate the training database for the single incident angle case

Theta (°)	Correlation Length (cm)	RMS Height (cm)	Soil Moisture (%)	Correlation Functions	Polarizations
40	1-9	0.1-2	1-40	Exponential	HH, VV

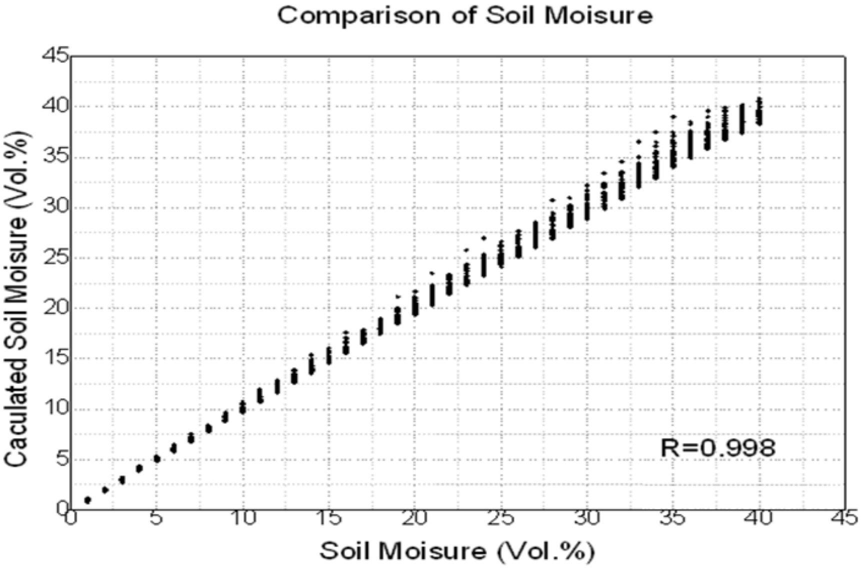

Figure 5.7 The comparison results of the estimated and simulated soil moisture from DLNN for the single incident angle case.

First, we used the 5000 of the samples generated from Table 5.1 to train the neural network and then retrieve the soil moisture. Second, we used the remaining 1000 samples, which are not included in the training database, to validate the retrieval results. Results are shown in Fig. 5.7. We can see from Fig. 5.7 that the correlation between the estimated soil moisture and simulated soil moisture is 0.998, which means that the accuracy of the soil moisture retrievals is very high. The results of the RMS height retrievals are similar. However, the correlation between the estimated correlation length and simulated correlation length is far from satisfactory. The same problem also emerges in the multi-incident angle case.

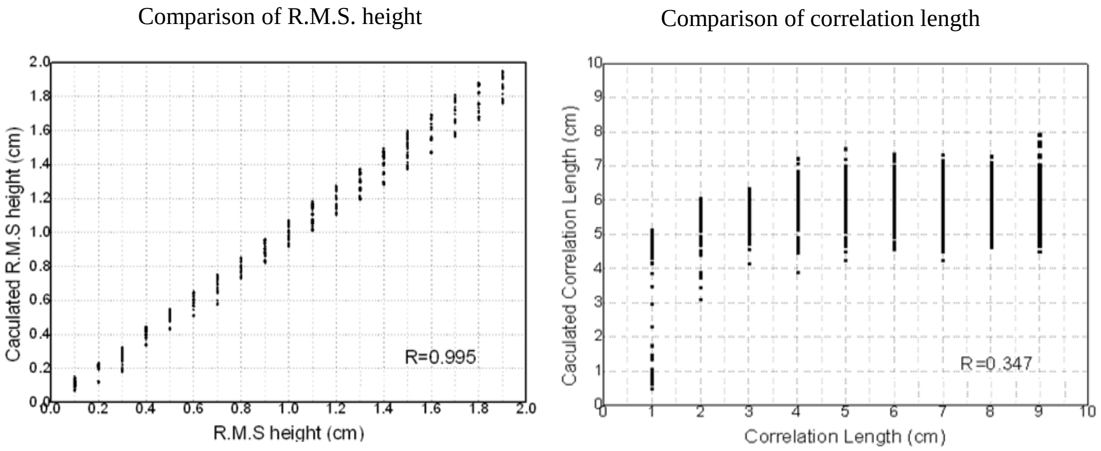
Comparison of R.M.S. height

Comparison of correlation length

Figure 5.8 Comparison results of the estimated and the simulated RMS height (left) and correlation length (right) from DLNN for the single incident angle case.

5.3.2.2 The results of not fixing the incident angle

In this part, we generated the training database by not setting the incident angle as a constant value, and then we tested the retrieval results. First, we define the range of each parameter used to generate the training database, see Table 5.2. We generated a total of 30,000 samples for training from our data. Second, we determined the input and the output of the DLNN, which depends on the application. In our case, the tested ALOS-2 SAR images have an incident angle varying from 38 to 43 degrees, so we set the incident angles to be the same as our data. The frequency was set to the L band (1.25 GHz), also the same as our test data. The outputs were the correlation length, the RMS height, and the soil moisture.

Table 5.2 The range of each parameter used to generate the training database for the multiple incident angle case

Theta(°)	Correlation Length (cm)	RMS height (cm)	Soil Moisture (%)	Correlation Functions	Polarizations
38-43	1-9	0.1-2	1-40	Exponential	HH,VV

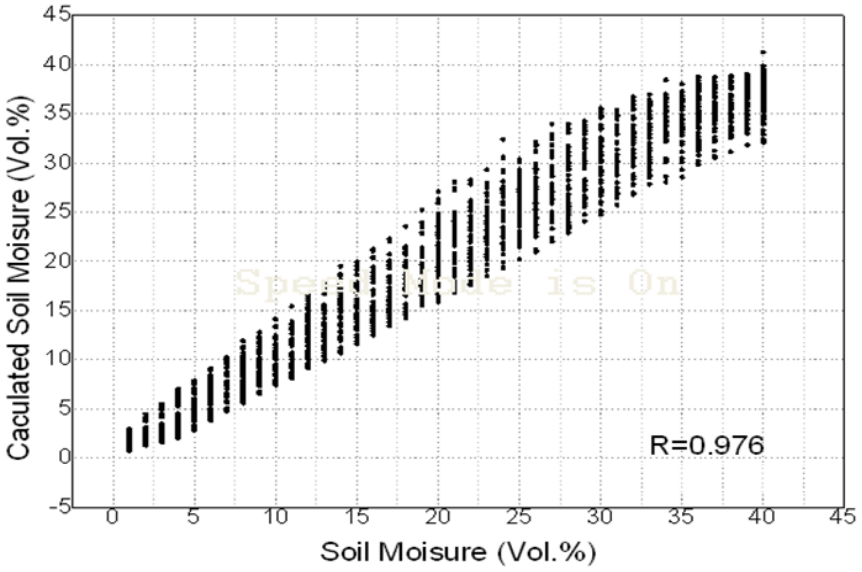

Figure 5.9 The comparison results of the estimated and the simulated soil moisture from DLNN for the multiple incident angle case.

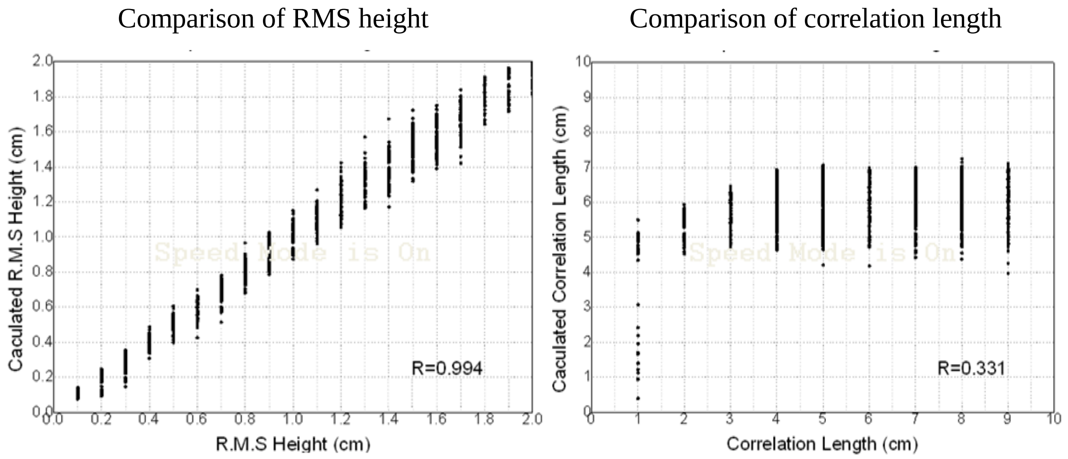

Figure 5.10 Comparison results of the estimated and the simulated RMS height (left) and correlation length (right) from DLNN for the multiple incident angle case.

5.4 Mapping of soil moisture change

5.4.1 Research area

The study area was the Yellow River Delta (YRD), located in Shandong Province from 13°21′-38°12′ N and 118°07′-119°10′E, with an area of 5450 km^2 is one of the largest deltas in China. It was formed by silt from the Yellow River. In the historical period, the Huang He River flowed through North Jiangsu into the Huanghai Sea for nearly 700 years. The location of the Yellow River Delta is shown in Fig. 5.11.

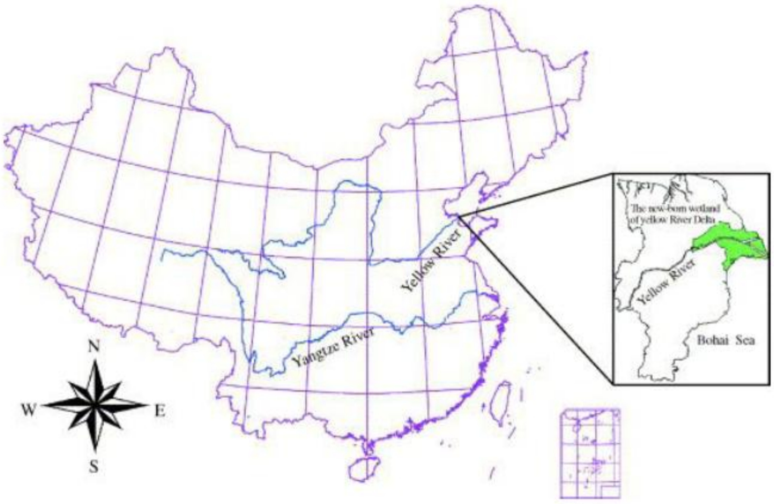

Figure 5.11 The location of the Yellow River Delta, Shandong Province, China.

The Yellow River Delta is located in the temperate zone and is characterized by a monsoon climate. It is rich in natural resources, such as crude oil, natural gas, chemical industry and crude salt. Of primary importance are the mechanical and chemical industries, food processing, the pulp industry, electricity and biology. Details of YRD’s climatic conditions are shown in Table 5.3.

Table 5.3 Climatic conditions of the YRD

Temperature(℃)	**Annual mean**	**12.3**
	Extreme high	41.9
	Extreme low	-23.3
	Degree-days(>0 ℃)	4783.5
	Degree-days(>0 ℃)	4183
Annual radiation ($MJ.m^{-2}$)	5146-5411	
Annual sunshine time(h)	2682	
Frost-free season(d)	210	
Annual mean precipitation(mm)	542.3-842	
Evaporation(mm)	1962	

5.4.2 ALOS-2 data

The Advanced Land Observing Satellite-2 “DAICHI-2” (ALOS-2) is a follow-on mission from the “Daichi” (ALOS). The ALOS satellite had contributed to cartography, regional observation, disaster monitoring, and resource surveys since its launch in 2006. ALOS-2 succeeded this mission with enhanced capabilities. In our study, we used two Level 1.0 ALOS-2 images: one was obtained on 13 November 2014, and the other was obtained on 20 December 2014. The frequency of the ALOS-2 data is 1.2 GHz, and the observation band is 25 km with 3-meter resolution in the “spotlight mode”. The observation mode and basic information of these ALOS-2 images are shown in Table 5.4 and Table 5.5, respectively. Both images were located in the YRD area and have a substantial area of overlap. We selected a bare soil region, shown in Fig. 5.12, to test our method.

Table 5.4 The observation mode of the ALOS-2 data

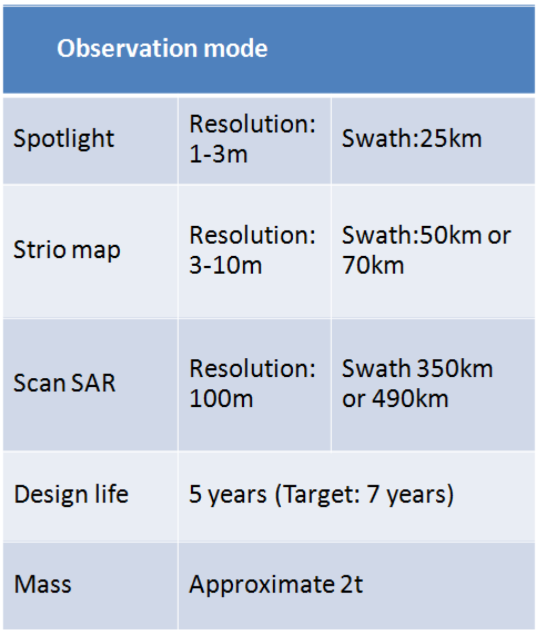

Observation mode		
Spotlight	Resolution: 1-3m	Swath:25km
Strio map	Resolution: 3-10m	Swath:50km or 70km
Scan SAR	Resolution: 100m	Swath 350km or 490km
Design life	5 years (Target: 7 years)	
Mass	Approximate 2t	

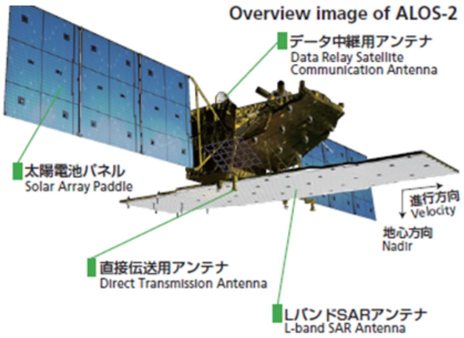

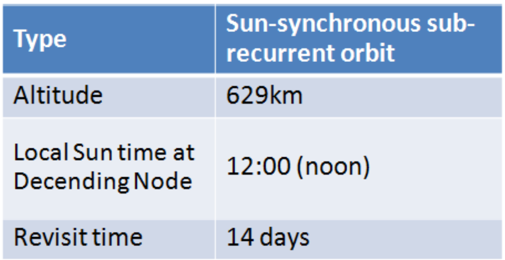

Type	Sun-synchronous sub-recurrent orbit
Altitude	629km
Local Sun time at Decending Node	12:00 (noon)
Revisit time	14 days

Table 5.5 The basic information of the two ALSO-2 images used in this study

Time	2014.11.13 16:01	The locations of the ALOS-2 data
latitude	37.253-37.964	
longitude	118.392-119.269	
Observation mode	Spotlight	
Polarization	HH,HV	
Frequency	1.2GHz	
Time	2014.12.06 15:54	
latitude	37.032-37.762	
longitude	118.616-119.559	
Observation mode	Spotlight	
Polarization	HH,HV	
Frequency	1.2 GHz	

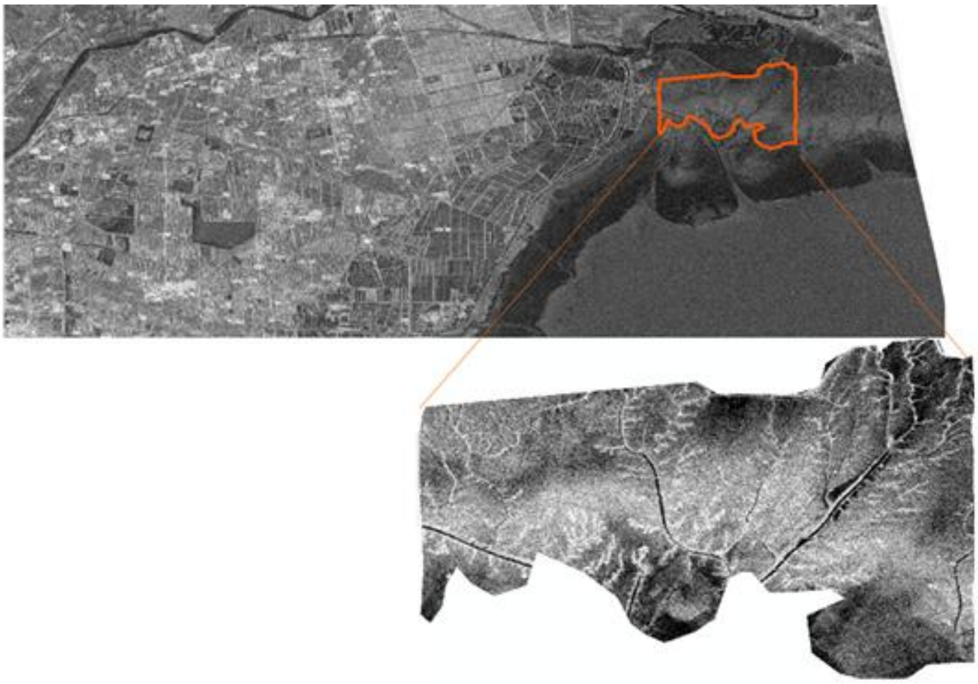

Figure 5.12 The research area cut from the overlapping area of the two ALOS-2 images.

5.4.3 Results and discussions

After applying the developed inversion method by using data from the two ALOS-2 images, we obtained the relative soil moisture changes within the research area. Fig. 5.13 shows the soil moisture changes in the research area nearly one month. From the results, we can see that the spatial distribution of the soil moisture change is relatively uniform. In most of the area, the soil moisture was drying up. The relatively larger changes of soil moisture occurred in the southern boundary. The boundary was wet down, presumably due to its closeness to the sea. In general, the spatial distribution of the soil moisture variation was reasonable, demonstrating the effectiveness of our method.

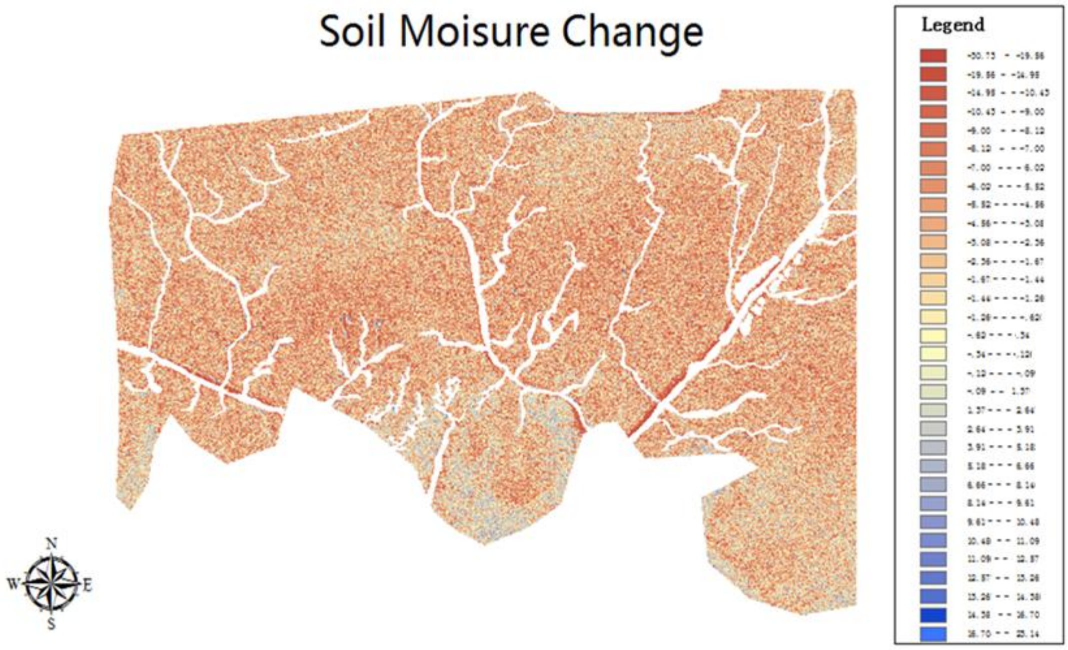

Figure 5.13 The soil moisture changes derived from the two ALOS-2 images.

5.5 Conclusions

This chapter presents our developed framework for soil moisture retrieval from radar measurements using a recurrent Kalman filter-based neural network. The network training and data inversion steps are described in detail. By using a generated database to train the Kalman filter-based neural network, we verified the retrieval results with the simulated data (excluding the training data). Results showed that the accuracy of the soil moisture and RMS height estimates was better than that of the correlation length, but all were generally satisfactory. Then it came to testing with real-world data. The relative soil moisture content was derived from ALOS-2 data by using the developed recurrent Kalman filter-based neural network. Overall, the spatial distribution of the soil moisture variation was reasonable, which demonstrated the effectiveness of our method. In a future stage, we will collect measurement data to validate our method.

Chapter 6 Conclusions and perspectives

Soil moisture is a crucial link between the land surface and the atmosphere, which directly affects the energy and hydrology exchange between the earth's surface and the atmospheric cycle. Active microwave remote sensing, especially SAR, is particularly attractive for remote sensing of soil moisture since it provides a measure of the absolute soil moisture content that are spatially averaged. It also has the advantages of large-scale coverage and all-weather operation. Therefore, in this dissertation research, we mainly focussed on sensitivity analysis and estimation of soil moisture from radar responses. In addition, a practical and reliable surface scattering model is often required to obtain a good understanding of the surface scattering mechanism. Thus, this dissertation research started from a study of the theoretical surface scattering model. We validated a well-established model, the AIEM, by extensive comparison with numerical simulations and experimental data. Then, based on the AIEM, we investigated in detail the sensitivity of bistatic scattering and backscattering to soil moisture and surface roughness of soil surfaces, respectively. Finally, in order to retrieval soil moisture from SAR images, we developed a recurrent Kalman filter-based neural network and tested this method in the Yellow River Delta (YRD) area by using ALOS-2 satellite data.

6.1 Main conclusions

The main conclusions of this dissertation research are as follows.

(1) Extensive experimental data and numerical simulation data were both used to fully evaluate the reliability of the AIEM. Firstly, we compared AIEM with numerical simulations for both backscattering and bistatic scattering. In the backscattering, we compared AIEM with the NMM3D; in the bistatic conditions, we compared AIEM with the numerical results of SSA and the MoM in the scattering plane. The results show that, when compared with the numerical simulations, all the predictions were quite close to each other except at a large incident/scattering angle. There is a dip at specular direction shown by MoM and SSA, but not by AIEM. Then, we compared AIEM with the experimental measurement data, also in both the backscattering and bistatic scattering conditions. We can conclude that in the backscattering condition,

the AIEM is generally in good agreement with the measured data at all cases, though it predicts the backscattering coefficients more accurately in the wet soil condition than in the dry soil condition. In the bistatic scattering condition, compared with the EMSL measurement data, AIEM also showed a good agreement although the predictions of the AIEM were on the high side at large scattering angles and there is not enough separation between the polarizations. In sum, the AIEM model matches well with both the numerical simulations and experimental data.

(2) Through a parameter sensitivity analysis for bistatic scattering of the rough surface, we obtained several findings. We investigated the bistatic radar response of soil moisture and surface roughness of bare soil surfaces at the L-band by using the AIEM model. The results show that higher sensitivity of radar scattering to the soil moisture can be achieved by configuring the bistatic observation rather than using the monostatic observation, from which only backscattering coefficients can be obtained. In a bistatic mode, the scattering coefficients of VV polarization are generally more sensitive to soil moisture than those of HH polarization. Unlike using only a single polarized or single angular scattering coefficient, the influence correlation function (an undesirable effect) can be considerably suppressed by a combination of dual polarized or dual angular measurements. Compared to the results of single polarized or combined dual polarized data, it seems that a combination of dual angular measurements achieved the most reliable soil moisture estimation since it could suppress the influence of surface roughness while maintaining a reasonably good sensitivity to soil moisture. Equally important to note is that the forward region is preferable for soil moisture sensing regardless of the type of correlation function: this is a quite attractive feature – useful and usable. Furthermore, it seems that as the difference between the dual angle increases, the sensitivity of the combined angular measurements to the soil moisture increases. It should be noted that although the out-of-plane bistatic radar configurations show great potential for soil moisture monitoring, the limitations imposed by the narrow angular window of maximum moisture sensitivity and the low signal level in these out-of-plane configurations would likely make the use of these configurations challenging.

(3) We analysed the radar backscattering response of soil moisture and, to test the real world, developed a method for retrieving soil moisture from ALOS-2 satellite

image data. From the sensitivity of backscattering coefficients to soil moisture under different frequencies, we found that the changes in the backscattering coefficients were larger in the L-band as soil moisture changed. We observed that the sensitivity of backscattering signals to soil moisture was high when the incident angle was relatively small at VV polarization. The sensitivity of backscattering signals to soil moisture decreased as the RMS height increased. Besides, we found that the influence of the correlation length on backscattering signals is much less than that of the RMS height. For the purposes of estimating soil moisture and solving the problems of multidimensional retrieval, a recurrent Kalman filter-based neural network method was developed, due to its ability to adapt the high geophysical dimensions. Essentially, the operation could be divided into two phases. The first phase was network training. We used the AIEM model to generate a training database by configuring radar parameters and setting surface parameters confined to the eligible research area. After completing the network training, we proceeded to the second phase, neural network operation. By using the generated database to train the Kalman filter-based neural network, we verified the retrieval results with the simulated data (excluding the training data). Results showed that the accuracy of the soil moisture and the RMS height estimations was better than that for the correlation length, and all were generally satisfactory. We also selected a bare soil region of the Yellow River Delta area to test our method. After applying the developed inversion method by using data from two ALOS-2 images, we obtained the relative soil moisture changes over the research area. From the results, we could see that the spatial distribution of the soil moisture changes was relatively uniform. In general, the spatial distribution of the soil moisture variation was reasonable, demonstrating the effectiveness of our method.

6.2 Perspectives

In this dissertation research, we developed a systematic analysis of bistatic radar scattering from randomly rough surfaces based on the AIEM which was fully validated by using both numerical simulations and experimental measurements. Subsequently, sensitivity analysis was carried out to explore the complex process and nonlinear coupling of wave-matter interactions, of which the soil moisture content is the major interest. Then moving forward from that problem, we proceeded to the inversion problem – retrieval of soil moisture from radar measurements. Future work would proceed in the following aspects.

(1) Although this dissertation research focuses on estimation of soil moisture from radar responses based on a high-precision theoretical model (i.e. the AIEM), all the research was only carried out in the bare soil surface situation. The retrieval of soil moisture in vegetated areas needs to be studied in the future.

(2) In this dissertation research we develop a recurrent Kalman filter-based neural network method to retrieve the soil moisture. This method successfully settles the problem that the surface parameters are strongly coupled and the relationship between them is nonlinear. The retrieved change of soil moisture estimates present a reasonable spatial distribution. However, this method should be tested with measurement data to further demonstrate its effectiveness. Currently new data acquisition is in progress to do this.

(3) The optimal bistatic configuration for soil moisture sensing was investigated in this study. We found that the combination of dual angular measurements achieved the most reliable soil moisture estimation since it could suppress the influence of surface roughness while maintaining a reasonably good sensitivity to soil moisture. However, on account of the geometric complexity of bistatic configuration, as well as the diversity of surface conditions, more extensive theoretical and experimental studies should be conducted to find the optimal bistatic angle range for soil moisture sensing by considering the signal-to-noise ratio (SNR) limitation.

References

Argenti, F., Lapini, A., Bianchi, T., & Alparone, L. (2013). A tutorial on speckle reduction in synthetic aperture radar images. *IEEE Geoscience and remote sensing magazine*, 1(3), 6-35.

Baghdadi, N., Holah, N., & Zribi, M. (2006). Soil moisture estimation using multi-incidence and multi-polarization ASAR data. *International Journal of Remote Sensing*, 27(10), 1907-1920.

Baghdadi, N. N., El Hajj, M., Zribi, M., & Fayad, I. (2016). Coupling SAR C-band and optical data for soil moisture and leaf area index retrieval over irrigated grasslands. *IEEE Journal of Selected Topics in Applied Earth Observations and Remote Sensing*, 9(3), 1229-1243.

Baghdadi, N., Saba, E., Aubert, M., Zribi, M., & Baup, F. (2011). Evaluation of radar backscattering models IEM, Oh, and Dubois for SAR data in X-band over bare soils. *IEEE Geoscience and Remote Sensing Letters*, 8(6), 1160-1164.

Bahar, E., & Chakrabarti, S. (1987). Full-wave theory applied to computer-aided graphics for 3D objects. *IEEE Computer Graphics and Applications*, 7(7), 46-60.

Barrett, B. W., Dwyer, E., & Whelan, P. (2009). Soil moisture retrieval from active spaceborne microwave observations: An evaluation of current techniques. *Remote Sensing*, 1(3), 210-242.

Bi, H., Ma, J., Zheng, W., & Zeng, J. (2016). Comparison of soil moisture in GLDAS model simulations and in - situ observations over the Tibetan Plateau. *Journal of Geophysical Research: Atmospheres*, 121, 2658–2678

Brocca, L., Moramarco, T., Melone, F., Wagner, W., Hasenauer, S., & Hahn, S. (2012). Assimilation of surface-and root-zone ASCAT soil moisture products into rainfall–runoff modeling. *IEEE Transactions on Geoscience and Remote Sensing*, 50(7), 2542-2555.

Brogioni, M., Pettinato, S., Macelloni, G., Paloscia, S., Pampaloni, P., Pierdicca, N., & Ticconi, F. (2010). Sensitivity of bistatic scattering to soil moisture and surface roughness of bare soils. *International Journal of Remote Sensing*, 31(15), 4227-4255.

Brown, R. G. and Hwang, P. Y.e C. (1983) Introduction to Random Signals and Applied Kalman Filtering. 2nd Ed. New York Wiley.

Bryant, R., Moran, M. S., Thoma, D. P., Holyfield Collins, C. D. H., Skirvin, S., Rahman, M., Slocum, K., Starks, P., Bosch, D., & Gonzalez Dugo, M. P. (2007). Measuring surface roughness height to parameterize radar backscatter models for retrieval of surface soil moisture. *IEEE Geoscience & Remote Sensing Letters*, 4(1), 137-141.

Carlson, T. N., Gillies, R. R., & Perry, E. M. (1994). A method to make use of thermal infrared temperature and NDVI measurements to infer surface soil water content and fractional vegetation cover. *Remote sensing reviews*, 9(1-2), 161-173.

Chang, W., & Tsang, L. (2012). A partial coherent physical model of third and fourth stokes parameters of sastrugi snow surfaces over layered media with rough surface boundary conditions of conical scattering combined with vector radiative transfer theory. *Progress in Electromagnetics Research B,* 45(45), 57-82.

Chen, K. S., Kao, W. L., & Tzeng, Y. C. (1995). Retrieval of surface parameters using dynamic learning neural network. *Remote Sensing*, 16(5), 801-809.

Chen, K. S., Li, Z. L., & Liu, Y. (2015). Model analysis of bistatic scattering from randomly rough surfaces. *Journal of Beijing University of Aeronautics and Astronautics*, 41(10): 1765-1776

Chen, K. S., Tsang, L., Chen, K. L., Liao, T. H., & Lee, J. S. (2014). Polarimetric simulations of SAR at L-band over bare soil using scattering matrices of random rough surfaces from numerical three-dimensional solutions of Maxwell equations. *IEEE Transactions on Geoscience and Remote Sensing*, 52(11), 7048-7058.

Chen, K. S., Wu, T. D., & Shi, J. C. (2001). A model-based inversion of rough soil surface parameters from radar measurements. *Journal of electromagnetic waves and applications*, 15(2), 173-200.

Chen, K. S., Wu, T. D., Tsang, L., Li, Q., Shi, J., & Fung, A. K. (2003). Emission of rough surfaces calculated by the integral equation method with comparison to three-dimensional moment method simulations. *IEEE Transactions on Geoscience and Remote Sensing*, 41(1), 90-101.

Chen, K. S., Wu, T. D., Tsay, M. K., & Fung, A. K. (2000). Note on the multiple scattering in an IEM model. *IEEE Transactions on Geoscience and Remote Sensing,* 38(1), 249-256.

Church, E. L., & Takacs, P. Z. (1995). Surface scattering. Handbook of Optics, 1, 7-1.

Davidson, M. W., Le Toan, T., Mattia, F., Satalino, G., Manninen, T., & Borgeaud, M. (2000). On the characterization of agricultural soil roughness for radar remote sensing studies. *IEEE Transactions on Geoscience and Remote Sensing, 38*(2), 630-640.

Dawson, M. S., Olvera, J., Fung, A. K., & Manry, M. T. (1992). Inversion of Surface Parameters Using Fast Learning Neural Networks. *International Geoscience and Remote Sensing Symposium, 1992. IGARSS '92.* (Vol.2, pp.910-912).

De Jeu, R. A. M., Holmes, T. R. H., Panciera, R., & Walker, J. P. (2009). Parameterization of the Land Parameter Retrieval Model for L-Band Observations Using the NAFE'05 Data Set. *IEEE Geoscience and Remote Sensing Letters,* 6(4), 630-634.

Dubois, P. C., Van Zyl, J., & Engman, T. (1995). Measuring soil moisture with imaging radars. *IEEE Transactions on Geoscience & Remote Sensing*, 33(4), 915-926.

El Hajj, M., Baghdadi, N., Zribi, M., Belaud, G., Cheviron, B., Courault, D., & Charron, F. (2016). Soil moisture retrieval over irrigated grassland using X-band SAR data. *Remote Sensing of Environment*, 176, 202-218.

Entekhabi, D., Njoku, E. G., O'Neill, P. E., Kellogg, K. H., Crow, W. T. et al. (2010). The soil moisture active passive (SMAP) mission. *Proceedings of the IEEE*, 98(5), 704-716.

Entekhabi, D., Yueh, S., O’Neill, P. E., Kellogg, K. H., Allen, A., Bindlish, R., et al. (2014). SMAP Handbook Soil Moisture Active Passive, Mapping Soil Moisture Freeze/Thaw from Space. Jet Propulsion Laboratory, National Aeronautics and Space Administration.

Fung, A. K. (1994). Microwave Scattering and Emission Models and Their Applications. Microwave scattering and emission models and their applications. Artech House.

Fung, A. K., & Chen, K. S. (2010). Microwave scattering and emission models for users. Artech House.

Fung, A. K., Li, Z., & Chen, K. S. (1992). Backscattering from a randomly rough dielectric surface. *IEEE Transactions on Geoscience & Remote Sensing*, 30(2), 356-369.

Gao, B. C. (1997). NDWI — a normalized difference water index for remote sensing of vegetation liquid water from space. *Remote Sensing of Environment*, 58(3), 257-266.

Goward, S. N., Cruickshanks, G. D., & Hope, A. S. (1985). Observed relation between thermal emission and reflected spectral radiance of a complex vegetated landscape. *Remote Sensing of Environment*, 18(2), 137-146.

Goward, S. N., Xue, Y., & Czajkowski, K. P. (2002). Evaluating land surface moisture conditions from the remotely sensed temperature/vegetation index measurements: an exploration with the simplified simple biosphere model. *Remote Sensing of Environment*, 79(2–3), 225-242.

Holah, N., Baghdadi, N., Zribi, M., Bruand, A., & King, C. (2005). Potential of ASAR/ENVISAT for the characterization of soil surface parameters over bare agricultural fields. *Remote sensing of environment*, 96(1), 78-86.

Huang, S., & Tsang, L. (2012). Electromagnetic scattering of randomly rough soil surfaces based on numerical solutions of Maxwell equations in three-dimensional simulations using a hybrid UV/PBTG/SMCG method. *IEEE Transactions on Geoscience and Remote Sensing*, 50(10), 4025-4035.

Huang, S., Tsang, L., Njoku, E. G., & Chan, K. S. (2010). Backscattering coefficients, coherent reflectivities, and emissivities of randomly rough soil surfaces at L-band for SMAP applications based on numerical solutions of Maxwell equations in three-dimensional simulations. *IEEE Transactions on Geoscience and Remote Sensing*, 48(6), 2557-2568.

Hush, D. R., & Horne, B. G. (1993). Progress in supervised neural networks. *IEEE signal processing magazine*, 10(1), 8-39.

Ishimaru, A. (1978). Wave propagation and scattering in random media (Vol. 2, pp. 349-351). New York: Academic Press.

Jackson, R. D., Idso, S. B., Reginato, R. J., & Pinter, P. J. (1981). Canopy temperature as a crop water stress indicator. *Water Resources Research*, 17(4), 1133-1138.

Jackson, T. J. (1993). Measuring surface soil moisture using passive microwave remote sensing. *Hydrological Processes*, 7(2), 139-152.

Johnson, J. T. (1998). A numerical study of low-grazing-angle backscatter from ocean-like impedance surfaces with the canonical grid method. *IEEE Transactions on Antennas & Propagation*, 46(1), 114-120.

Johnson, J. T., & Ouellette, J. D. (2014). Polarization features in bistatic scattering from rough surfaces. *IEEE Transactions on Geoscience and Remote Sensing*, 52(3), 1616-1626.

Johnson, J. T., Shin, R. T., Kong, J. A., & Tsang, L. (1996). A numerical study of the composite surface model for ocean backscattering. *IEEE Transactions on Geoscience & Remote Sensing*, 36(1), vol.2, 1401-1403.

Joseph, A. T., van der Velde, R., O'Neill, P. E., Lang, R., & Gish, T. (2010). Effects of corn on C-and L-band radar backscatter: A correction method for soil moisture retrieval. *Remote Sensing of Environment*, 114(11), 2417-2430.

Jung, M., Reichstein, M., Ciais, P., Seneviratne, S. I., Sheffield, J., Goulden, M. L., et al. (2010). Recent decline in the global land evapotranspiration trend due to limited moisture supply. *Nature*, 467(7318), 951-954.

Kerr, Y. H., Waldteufel, P., Richaume, P., Wigneron, J. P., Ferrazzoli, P., Mahmoodi, A., Al Bitar, A., Cabot, F., Gruhier, C., Juglea, S. E., Leroux, D., Mialon, A., & Delwart, S. (2012). The SMOS soil moisture retrieval algorithm. *IEEE Transactions on Geoscience and Remote Sensing*, 50(5), 1384-1403.

Kogan, F. N. (1998). Global drought and flood-watch from NOAA polar-orbiting satellites. *Advances in Space Research*, 21(3), 477-480.

Koike, T., Nakamura, Y., Kaihotsu, I., Davva, G., Matsuura, N., Tamagawa, K., & Fujii, H. (2004). Development of an Advanced Microwave Scanning Radiometer (AMSR-E) algorithm of soil moisture and vegetation water content. *Annual Journal of Hydraulic Engineering, JSCE*, 48, 217–222.

Kornelsen, K. C., & Coulibaly, P. (2013). Advances in soil moisture retrieval from synthetic aperture radar and hydrological applications. *Journal of Hydrology*, 476, 460-489.

Koster, R. D., Dirmeyer, P. A., Guo, Z., Bonan, G., Chan, E., Cox, P., et al. (2004). Regions of strong coupling between soil moisture and precipitation. *Science*, 305(5687), 1138–1140.

Kurt, M., & Edwards, D. (2009). A survey of BRDF models for computer graphics. *ACM SIGGRAPH Computer Graphics*, 43(2), 1-7.

Lasne, Y., Paillou, P., August-Bernex, T., & Ruffie, G. (2004). A phase signature for detecting wet subsurface structures using polarimetric L-band SAR. *IEEE Transactions on Geoscience & Remote Sensing*, 42(8), 1683-1694.

Li, L., Chan, C. H., & Tsang, L. (1994). Numerical simulation of conical diffraction of tapered electromagnetic waves from random rough surfaces and applications to passive remote sensing. *Radio Science*, 29(3), 587-598.

Li, X. H., Song, X. N., & Zhou, X. (2010). Study on methods of monitoring soil moisture by remote sensing in semi-arid areas. *Geography and Geo-Information Science*, 26(1), 90-90.

Liang, D., Xu, P., Tsang, L., Gui, Z., & Chen, K. S. (2009). Electromagnetic scattering by rough surfaces with large heights and slopes with applications to microwave remote sensing of rough surface over layered media. *Progress in Electromagnetics Research*, 95(4), 199-218.

Lin, D. S., Wood, E. F., Beven, K., & Saatchi, S. (1994). Soil moisture estimation over grass-covered areas using AIRSAR. *International journal of remote sensing*, 15(11), 2323-2333.

Miralles, D. G., Holmes, T. R. H., de Jeu, R. A. M., Gash, J. H., Meesters, A. G. C. A., & Dolman, A. J. (2011). Global land-surface evaporation estimated from satellite-based observations. *Hydrology and Earth System Sciences*, 15(2), 453-469.

Miralles, D. G., Van den Berg, M. J., Gash, J. H., Parinussa, R. M., De Jeu, R. A.M., Beck, H. E., et al. (2014). El Niño–La Niña cycle and recent trends in continental evaporation. *Nature Climate Change*, 4(2), 122–126.

Moreira, A., Prats-Iraola, P., Younis, M., Krieger, G., Hajnsek, I., & Papathanassiou, K. P. (2013). A tutorial on synthetic aperture radar. *IEEE Geoscience and Remote Sensing Magazine*, 1(1), 6-43.

Nie, D., Zhang, M., Wang, C., & Yin, H. C. (2012). Study of microwave backscattering from two-dimensional nonlinear surfaces of finite-depth seas. *IEEE Transactions on Geoscience and Remote Sensing*, 50(11), 4349-4357.

Njoku, E. G., & Chan, S. K. (2006). Vegetation and surface roughness effects on AMSR-E land observations. *Remote Sensing of Environment*, 100(2), 190-199.

Oh, Y., Sarabandi, K., & Ulaby, F. T. (1992). An empirical model and an inversion technique for radar scattering from bare soil surfaces. *IEEE transactions on Geoscience and Remote Sensing*, 30(2), 370-381.

Owe, M., de Jeu, R. A. M., & Holmes, T. R. H. (2008). Multisensor historical climatology of satellite-derived global land surface moisture. *Journal of Geophysical Research: Earth Surface*, 113, F01002, doi:10.1029/2007JF000769.

Parinussa, R. M., Wang, G., Holmes, T. R. H., Liu, Y. Y., Dolman, A. J., de Jeu, R. A. M., Jiang, T., Zhang, P., & Shi, J. (2014). Global surface soil moisture from the Microwave Radiation Imager onboard the Fengyun-3B satellite. *International Journal of Remote Sensing*, 35(19), 7007-7029.

Pierdicca, N., Pulvirenti, L., Ticconi, F., & Brogioni, M. (2008). Radar bistatic configurations for soil moisture retrieval: a simulation study. *IEEE Transactions on Geoscience and Remote Sensing*, 46(10), 3252-3264.

Rahman, M. M., Moran, M. S., Thoma, D. P., Bryant, R., Collins, C. H., Jackson, T., Orr, B. J., & Tischler, M. (2008). Mapping surface roughness and soil moisture using multi-angle radar imagery without ancillary data. *Remote Sensing of Environment*, 112(2), 391-402.

Rao, K. S., Raju, S., & Wang, J. R. (1993). Estimation of soil moisture and surface roughness parameters from backscattering coefficient. *IEEE Transactions on Geoscience & Remote Sensing*, 31(5), 1094-1099.

Saleh, K., Kerr, Y. H., Richaume, P., Escorihuela, M. J., Panciera, R., Delwart, S., Boulet, G., Maisongrande, P., Walker, J. P., Wursteisen, P., & Wigneron, J. P. (2009). Soil moisture retrievals at L-band using a two-step inversion approach (COSMOS/NAFE'05 Experiment). *Remote Sensing of Environment*, 113(6), 1304-1312.

Sandholt, I., Rasmussen, K., Andersen, J.(2002). A simple interpretation of the surface temperature/vegetation index space for assessment of surface moisture status[J]. *Remote Sensing of Environment*, 79(2-3): 213-224.

Shao, M. A., Wang, Q. J., & Huang, M. B. (2006). Soil Physics. Higher Education Press.

Shi, J., Jiang, L., Zhang, L., Chen, K. S., Wigneron, J. P., & Chanzy, A. (2005). A parameterized multifrequency-polarization surface emission model. *IEEE Transactions on Geoscience and Remote Sensing*, 43(12), 2831-2841.

Shi, J., Wang, J., Hsu, A. Y., O'Neill, P. E., & Engman, E. T. (1997). Estimation of bare surface soil moisture and surface roughness parameter using L-band SAR image data. *IEEE Transactions on Geoscience and Remote Sensing*, 35(5), 1254-1266.

Shi, J. C., Jiang, L. M., Zhang, L. X., Chen, K. S., Wigneron, J. P., Chanzy, A., & Jackson, T. J. (2006). Physically based estimation of bare-surface soil moisture with the passive radiometers. *IEEE Transactions on Geoscience and Remote Sensing*, 44(11), 3145–3153.

Spizzichino, A., & Beckmann, P. (1963). *The Scattering of Electromagnetic Waves from Rough Surfaces*. New York, Paris.

Srivastava, H. S., Patel, P., Sharma, Y., & Navalgund, R. R. (2009). Large-area soil moisture estimation using multi-incidence-angle RADARSAT-1 SAR data. *IEEE Transactions on Geoscience and Remote Sensing*, 47(8), 2528-2535.

Tassoudji, M. A., Sarabandi, K., & Ulaby, F. T. (1989). Design consideration and implementation of the LCX polarimetric scatterometer (POLARSCAT). University of Michigan, College of Engineering, Department of Electrical Engineering & Computer Science, Radiation Laboratory.

Taylor, C. M., De Jeu, R. A.M., Guichard, F., Harris, P. P., & Dorigo, W. A. (2012). Afternoon rain more likely over drier soils. *Nature*, 489(7416), 282–286.

Tian, G. (1991). Methods for monitoring soil moisture using remote sensing technique. *Remote Sensing of Environment*, Vol.6, No. 2, 89-99

Tsang, L., Chan, C. H., Pak, K., & Sangani, H. (1995). Monte-Carlo simulations of large-scale problems of random rough surface scattering and applications to grazing incidence with the BMIA/canonical grid method. *IEEE Transactions on Antennas & Propagation*, 43(8), 851-859.

Tsang, L., Chen, Z., Oh, S., Marks, R. J., & Chang, A. T. (1992). Inversion of snow parameters from passive microwave remote sensing measurements by a neural network trained with a multiple scattering model. *IEEE Transactions on Geoscience and Remote Sensing*, 30(5), 1015-1024.

Tsang, L., Ding, K. H., Huang, S., & Xu, X. (2012). Electromagnetic computation in scattering of electromagnetic waves by random rough surface and dense media in microwave remote sensing of land surfaces. *Proceedings of the IEEE*, 101(2), 255-279.

Tsang, L., Koh, I. S., Liao, T. H., Huang, S., Xu, X., & Njoku, E. G., et al. (2013). Active and passive vegetated surface models with rough surface boundary conditions from NMM3D. *IEEE Journal of Selected Topics in Applied Earth Observations & Remote Sensing*, 6(3), 1698-1709.

Tsang, L., Kong, J. A., & Ding, K. H. (2000). Scattering of electromagnetic waves, *Theories and Applications*. 18(11), 445.

Tsang, L., Kong, J. A., & Shin, R. T. (1985). Theory of microwave remote sensing. Wiley-Interscience, New York

Tsang, L., Xu, P., & Chen, K. S. (2008). Third and fourth stokes parameters in polarimetric passive microwave remote sensing of rough surfaces over layered media. *Microwave & Optical Technology Letters*, 50(12), 3063-3069.

Tzeng, Y. C., Chen, K. S., Kao, W. L., & Fung, A. K. (1994). A dynamic learning neural network for remote sensing applications. *IEEE Transactions on Geoscience and Remote Sensing*, 32(5), 1096-1102.

Ulaby, F. T., & Batlivala, P. P. (1976). Optimum radar parameters for mapping soil moisture. *IEEE Transactions on Geoscience Electronics*, 14(2), 81-93.

Ulaby, F. T., Batlivala, P. P., & Dobson, M. C. (1978). Microwave backscatter dependence on surface roughness, soil moisture, and soil texture: Part I-bare soil. *IEEE Transactions on Geoscience Electronics*, 16(4), 286-295.

Ulaby, F. T., Long, D. G., Blackwell, W. J., Elachi, C., Fung, A. K., & Ruf, C., et al. (2014). Microwave radar and radiometric remote sensing. The University of Michigan Press.

Ulaby, F. T., Moore, R. K., & Fung, A. K. (1982). Radar remote sensing and surface scattering and emission theory. Microwave *Remote Sensing Active & Passive, ii*.

Voronovich, A. G. (2013). Wave scattering from rough surfaces (Vol. 17). Springer Science & Business Media.

Wang, L., & Qu, J. J. (2009). Satellite remote sensing applications for surface soil moisture monitoring: A review. *Frontiers of Earth Science in China*, 3(2), 237-247.

Wang, S. F., Zhang, Z. Y., Duan, A. W., & Gao, Y. (2008). Time sequence characteristic analysis of precipitation in north area of Henan province. *China Rural Water & Hydropower*. (3), 13-16

Wigneron, J. P., Calvet, J. C., Pellarin, T., Van de Griend, A. A., Berger, M., & Ferrazzoli, P. (2003). Retrieving near-surface soil moisture from microwave radiometric observations: current status and future plans. *Remote Sensing of Environment*, *85*(4), 489-506.

Wigneron, J. P., Kerr, Y., Waldteufel, P., Saleh, K., Escorihuela, M. J., Richaume, P., Ferrazzoli, P., de Rosnay, P., Gurney, R., Calvet, J. C., Grant, J. P., Guglielmetti, M., Hornbuckle, B., Mätzler, C., Pellarin, T., & Schwank, M. (2007). L-band Microwave Emission of the Biosphere (L-MEB) Model: Description and calibration against experimental data sets over crop fields. *Remote Sensing of Environment*, 107(4), 639-655.

Wu, T. D., Chen, K. S., Shi, J., & Fung, A. K. (2001). A transition model for the reflection coefficient in surface scattering. *IEEE Transactions on Geoscience and Remote Sensing*, 39(9), 2040-2050.

Wu, T. D., Chen, K. S., Shi, J., Lee, H. W., & Fung, A. K. (2008). A study of an AIEM model for bistatic scattering from randomly rough surfaces. *IEEE Transactions on Geoscience and Remote Sensing*, 46(9), 2584-2598.

Xu, P., Chen, K., & Tsang, L. (2010). Analysis of Microwave Emission of Exponentially Correlated Rough Soil Surfaces from 1. 4 GHz to 36. 5 GHz. *Progress In Electromagnetics Research*, 108, 205-219.

Xu, P., & Tsang, L. (2007). Bistatic scattering and emissivities of lossy dielectric surfaces with exponential correlation functions. *IEEE Transactions on Geoscience & Remote Sensing*, 45(1), 62-72.

Xu, P., Tsang, L., & Chen, K. (2012). Fourth stokes parameter in polarimetric passive remote sensing from two-layer rough surfaces. *Progress In Electromagnetics Research*, 129, 125-141.

Yang, G., & Du, Y. (2013). An optimized Monte Carlo procedure and its application in electromagnetic scattering from rough surfaces. *IEEE Transactions on Geoscience & Remote Sensing*, 52(5), 470-472.

Zahn, D., Sabet, K. F., & Sarabandi, K. (2000). Numerical simulation of scattering from rough surfaces: a wavelet-based approach. *IEEE Antennas and Propagation Society International Symposium, 1997.* (Vol.48, pp.246-253).

Zeng, J., Chen, K. S., Bi, H., & Chen, Q. (2016a). A Preliminary Evaluation of the SMAP Radiometer Soil Moisture Product Over United States and Europe Using Ground-Based Measurements. *IEEE Transactions on Geoscience and Remote Sensing*, 54(8), 4929-4940.

Zeng, J., Chen, K. S., Bi, H., & Chen, Q. (2016b) “Radar response of off-specular bistatic scattering to soil moisture and surface roughness at L-band,” *IEEE Geoscience and Remote Sensing Letters* 2016, in revision.

Zeng, J., Li, Z., Chen, Q., & Bi, H. (2014). A simplified physically-based algorithm for surface soil moisture retrieval using AMSR-E data. *Frontiers of Earth Science*, 8(3), 427-438.

Zeng, J. Y., Li, Z., Chen, Q., & Bi, H. Y. (2015a). Method for soil moisture and surface temperature estimation in the Tibetan Plateau using spaceborne radiometer observations. *IEEE Geoscience and Remote Sensing Letters*, 12(1), 97–101.

Zeng, J. Y., Li, Z., Chen, Q., Bi, H. Y., Qiu, J. X., & Zou, P. F. (2015b). Evaluation of remotely sensed and reanalysis soil moisture products over the Tibetan Plateau using in-situ observations. *Remote Sensing of Environment*, 163, 91–110.

Zhang, Y. J., Wang, J. Z., & Bao, Y. S. (2010). Soil moisture retrieval from multi-resource remotely sensed images over a wheat area. *Advances in Water Science*, 21(2), 222-228.

Zribi, M., Gorrab, A., & Baghdadi, N. (2014a). A new soil roughness parameter for the modelling of radar backscattering over bare soil. *Remote Sensing of Environment*, 152, 62-73.

Zribi, M., Gorrab, A., Baghdadi, N., Lili-Chabaane, Z., & Mougenot, B. (2014b). Influence of radar frequency on the relationship between bare surface soil moisture vertical profile and radar backscatter. *IEEE Geoscience and Remote Sensing Letters*, 11(4), 848-852.

Appendix

I Coefficients B and C

In this appendix, we give the explicit expressions of the upward and downward re-radiation coefficients used in Eq. (18a)-(18d).

$$\mathrm{C}_1 = \cos\left(\phi_s - \phi\right)\left[1 - \frac{\left(k_{sx} + u\right)\left(k_x + u\right)}{\left(k_{sz} - q\right)\left(k_z + q\right)}\right] - \sin\left(\phi_s - \phi\right)\frac{\left(k_z + u\right)\left(k_{sy} + v\right)}{\left(k_{sz} - q\right)\left(k_z - q\right)} \tag{A1}$$

$$\begin{aligned}\mathrm{C}_2 = {} & -\cos\left(\phi_s - \phi\right)\left[-q\cos\theta + \frac{u\cos\theta\left(k_{sx} + u\right)}{k_{sz} - q} - \frac{q_1\sin\theta\left(k_x + u\right)}{k_z + q} + \frac{u\sin\theta\left(k_{sx} + u\right)\left(k_x + u\right)}{\left(k_{sz} - q\right)\left(k_z + q\right)}\right. \\ & \left. - \frac{v\cos\theta\left(k_y + v\right)}{k_z + q} + \frac{v\sin\theta\left(k_{sx} + u\right)\left(k_y + v\right)}{\left(k_{sz} - q\right)\left(k_z + q\right)}\right] \\ & + \sin\left(\phi_s - \phi\right)\left[-\frac{u\cos\theta\left(k_{sy} + v\right)}{k_{sz} - q} - \frac{u\sin\theta\left(k_x + u\right)\left(k_{sy} + v\right)}{\left(k_{sz} - q\right)\left(k_z + q\right)} + \frac{q_1\sin\theta\left(k_y + v\right)}{k_z + q}\right. \\ & \left. - \frac{u\cos\theta\left(k_y + v\right)}{k_z + q} - \frac{v\sin\theta\left(k_{sy} + v\right)\left(k_y + v\right)}{\left(k_{sz} - q\right)\left(k_z + q\right)}\right]\end{aligned} \tag{A2}$$

$$\begin{aligned}\mathrm{C}_3 = {} & \frac{-\left(k_z + q\right)\sin\theta + \left(k_x + u\right)\cos\theta}{\left(k_{sz} - q\right)\left(k_z + q\right)} \\ & + \frac{\left[k_{sx}q\cos\left(\phi_s - \phi\right) + k_{sy}q\sin\left(\phi_s - \phi\right) + k_{sz}u\cos\left(\phi_s - \phi\right) + k_{sz}v\sin\left(\phi_s - \phi\right)\right]}{\left(k_{sz} - q\right)\left(k_z + q\right)}\end{aligned} \tag{A3}$$

$$\begin{aligned}\mathrm{C}_4 = {} & \cos\theta_s\sin\left(\phi_s - \phi\right)\left[\frac{\sin\theta\left(k_y + v\right)}{k_z + q} + \frac{\cos\theta\left(k_{sx} + u\right)\left(k_y + v\right)}{\left(k_{sz} - q\right)\left(k_z + q\right)}\right] \\ & + \cos\theta_s\cos\left(\phi_s - \phi\right)\left[\cos\theta + \frac{\sin\theta\left(k_x + u\right)}{k_z + q} - \frac{\cos\theta\left(k_{sy} + v\right)\left(k_y + v\right)}{\left(k_{sz} - q\right)\left(k_z + q\right)}\right] \\ & + \sin\theta_s\left[\frac{\cos\theta\left(k_{sx} + u\right)}{k_{sz} - q} + \frac{\sin\theta\left(k_{sx} + u\right)\left(k_x + u\right)}{\left(k_{sz} - q\right)\left(k_z + q\right)} + \frac{\sin\theta\left(k_{sy} + v\right)\left(k_y + v\right)}{\left(k_{sz} - q\right)\left(k_z + q\right)}\right]\end{aligned} \tag{A4}$$

$$\begin{aligned}\mathrm{C}_5 = {} & -\cos\theta_s\sin\left(\phi_s - \phi\right)\left[\frac{\left(k_{sx} + u\right)v}{k_{sz} - q} + \frac{\left(k_x + u\right)v}{k_z + q}\right] \\ & - \cos\theta_s\cos\left(\phi_s - \phi\right)\left[q + \frac{\left(k_x + u\right)u}{k_z + q} - \frac{\left(k_{sy} + v\right)v}{k_{sz} - q}\right] \\ & - \sin\theta_s\left[\frac{q_1\left(k_{sx} + u\right)}{k_{sz} - q} + \frac{u\left(k_{sx} + u\right)\left(k_x + u\right)}{\left(k_{sz} - q\right)\left(k_z + q\right)} + \frac{v\left(k_{sy} + v\right)\left(k_x + u\right)}{\left(k_{sz} - q\right)\left(k_z + q\right)}\right]\end{aligned} \tag{A5}$$

$$\begin{aligned}\mathrm{C}_6 = {} & \cos\theta_s \sin\left(\phi_s - \phi\right)\left[\frac{q\left(k_{sx}+u\right)\left(k_y+v\right)}{\left(k_{sz}-q\right)\left(k_z+q\right)} + \frac{u\left(k_y+v\right)}{k_z+q}\right] \\ & - \cos\theta_s \cos\left(\phi_s - \phi\right)\left[\frac{q_1\left(k_{sy}+u\right)\left(k_y+v\right)}{\left(k_{sz}-q\right)\left(k_z+q\right)} + \frac{v\left(k_y+v\right)}{k_z+q}\right] \\ & + \sin\theta_s\left[\frac{u\left(k_{sy}+v\right)\left(k_y+v\right)}{\left(k_{sz}-q\right)\left(k_z+q\right)} - \frac{u\left(k_{sx}+u\right)\left(k_x+v\right)}{\left(k_{sz}-q\right)\left(k_z+q\right)}\right]\end{aligned} \tag{A6}$$

$$\begin{aligned}\mathrm{B}_1 = {} & \cos\theta_s \sin\left(\phi_s - \phi\right)\left[1 - \frac{q\left(k_{sx}+u\right)\left(k_x+u\right)}{\left(k_{sz}-q\right)\left(k_z+q\right)}\right] \\ & + \cos\theta_s \cos\left(\phi_s - \phi\right)\frac{\sin\theta_s k_{sx} + \left(k_{sy}+v\right)}{k_{sz}-q}\frac{\left(k_x+u\right)\left(k_{sy}+v\right)}{\left(k_{sz}-q\right)\left(k_z+q\right)}\end{aligned} \tag{A7}$$

$$\begin{aligned}\mathrm{B}_2 = {} & \cos\theta_s \sin\left(\phi_s - \phi\right)\left[q\cos\theta - \frac{u\cos\theta\left(k_{sx}+u\right)}{k_{sz}-q} + \frac{q\sin\theta\left(k_x+u\right)}{k_z+q}\right. \\ & \left. - \frac{u\sin\theta\left(k_{sx}+u\right)\left(k_x+u\right)}{\left(k_{sz}-q\right)\left(k_z+q\right)} + \frac{v\cos\theta\left(k_y+v\right)}{k_z+q} - \frac{v\sin\theta\left(k_{sx}+u\right)\left(k_x+u\right)}{\left(k_{sz}-q\right)\left(k_z+q\right)}\right] \\ & + \sin\theta_s\left[\frac{q\cos\theta\left(k_{sy}+v\right)}{k_{sz}-q} + \frac{q_1\sin\theta\left(k_x+u\right)\left(k_{sy}+v\right)}{\left(k_{sz}-q\right)\left(k_z+q\right)} + \frac{q_1\sin\theta\left(k_{sx}+u\right)\left(k_y+v\right)}{\left(k_{sz}-q\right)\left(k_z+q\right)}\right. \\ & \left. + \frac{u\cos\theta\left(k_{sx}+u\right)\left(k_y+v\right)}{\left(k_{sz}-q\right)\left(k_z+q\right)} + \frac{v\cos\theta\left(k_{sy}+v\right)\left(k_y+v\right)}{\left(k_{sz}-q\right)\left(k_z+q\right)}\right] \\ & + \cos\theta_s \cos\left(\phi_s - \phi\right)\left[\frac{q\cos\theta\left(k_{sy}+v\right)}{k_{sz}-q} + \frac{u\sin\theta\left(k_x+u\right)\left(k_{sy}+v\right)}{\left(k_{sz}-q\right)\left(k_z+q\right)} - \frac{q\sin\theta\left(k_y+v\right)}{k_z+q}\right. \\ & \left. + \frac{u\cos\theta\left(k_y+v\right)}{k_z+q} + \frac{v\sin\theta\left(k_y+v\right)\left(k_{sy}+v\right)}{\left(k_{sz}-q\right)\left(k_z+q\right)}\right]\end{aligned} \tag{A8}$$

$$\begin{aligned}\mathrm{B}_3 = {} & -\cos\theta_s \sin\left(\phi_s - \phi\right)\left[\frac{q\sin\theta\left(k_{sx}+u\right)}{k_{sz}-q} + u\sin\theta - \frac{q\cos\theta\left(k_{sx}+u\right)\left(k_x+u\right)}{\left(k_{sz}-q\right)\left(k_z+q\right)} - \frac{u\cos\theta\left(k_x+u\right)}{k_z+q}\right] \\ & + \cos\theta_s \cos\left(\phi_s - \phi\right)\left[\frac{q_1\sin\theta\left(k_{sy}+v\right)}{k_{sz}-q} + v\sin\theta - \frac{q_1\cos\theta\left(k_{sy}+v\right)\left(k_x+u\right)}{\left(k_{sz}-q_1\right)\left(k_z+q\right)} - \frac{v\cos\theta\left(k_x+u\right)}{k_z+q}\right] \\ & - \sin\theta_s\left[\frac{u\sin\theta\left(k_{sy}+v\right)}{k_z-q} - \frac{u\cos\theta\left(k_{sy}+v\right)\left(k_x+u\right)}{\left(k_{sz}-q\right)\left(k_z+q\right)} - \frac{v\sin\theta\left(k_{sx}+u\right)}{k_{sz}-q} + \frac{v\cos\theta\left(k_{sx}+u\right)\left(k_x+u\right)}{\left(k_{sz}-q\right)\left(k_z+q\right)}\right]\end{aligned} \tag{A9}$$

$$\begin{aligned}\mathrm{B}_4 = {} & \cos\left(\phi_s - \phi\right)\left[\frac{\sin\theta\left(k_y+v\right)}{k_z+q} + \frac{\cos\theta\left(k_{sx}+u\right)\left(k_y+v\right)}{\left(k_{sz}-q\right)\left(k_z+q\right)}\right] \\ & - \sin\left(\phi_s - \phi\right)\left[\cos\theta + \frac{\sin\theta\left(k_x+u\right)}{k_z+q} - \frac{\cos\theta\left(k_{sy}+v\right)\left(k_y+v\right)}{\left(k_{sz}-q\right)\left(k_z+q\right)}\right]\end{aligned} \tag{A10}$$

$$\begin{aligned}\mathrm{B}_5 = &-\cos\left(\phi_s-\phi\right)\left[\frac{v\left(k_{sx}+u\right)}{k_{sz}-q}+\frac{v\left(k_x+u\right)}{k_z+q}\right]\\ &+\sin\left(\phi_s-\phi\right)\left[q-\frac{v\left(k_{sy}+v\right)}{k_{sz}-q}-\frac{u\left(k_x+u\right)}{k_z+q}\right]\end{aligned} \tag{A11}$$

$$\begin{aligned}\mathrm{B}_6 = &\cos\left(\phi_s-\phi\right)\left[\frac{q\left(k_{sx}+u\right)\left(k_y+v\right)}{\left(k_{sz}-q\right)\left(k_z+q\right)}+\frac{u\left(k_y+v\right)}{k_z+q}\right]\\ &+\sin\left(\phi_s-\phi\right)\left[\frac{q\left(k_{sy}+v\right)\left(k_y+v\right)}{\left(k_{sz}-q\right)\left(k_z+q\right)}+\frac{v\left(k_y+v\right)}{k_z+q}\right]\end{aligned} \tag{A12}$$

II Coefficients a, b, c in the Transition Function

Under the framework of the AIEM model, the three terms are:

$$a = k_i \left(\cos\theta_s + \cos\theta_i \right) \left| f_{qp} \right|^2 \tag{B1}$$

$$\begin{aligned}
b = \frac{1}{2} \Big\{ & f_{qp}^{*} \boldsymbol{\mathfrak{F}}_{qp}^{+}(-k_{ix}, -k_{iy})[k_i \cos\theta_s - k_{iz}][k_i \cos\theta_s + k_i \cos\theta_i] \\
& + f_{qp}^{*} \boldsymbol{\mathfrak{F}}_{qp}^{+}(-k_{sx}, -k_{sy})[k_i \cos\theta_s + k_{sz}][k_i \cos\theta_s + k_i \cos\theta_i] \Big\} \\
+ \frac{1}{2} \Big\{ & f_{qp}^{*} \boldsymbol{\mathfrak{F}}_{qp}^{-}(-k_{ix}, -k_{iy})[k_i \cos\theta_s + k_{iz}][k_i \cos\theta_s + k_i \cos\theta_i] \\
& + f_{qp}^{*} \boldsymbol{\mathfrak{F}}_{qp}^{-}(-k_{sx}, -k_{sy})[k_i \cos\theta_s - k_{sz}][k_i \cos\theta_s + k_i \cos\theta_i] \Big\} \\
+ \frac{1}{2} \Big\{ & f_{qp}^{*} \boldsymbol{\mathfrak{G}}_{qp}^{+}(-k_{ix}, -k_{iy})[k_i \cos\theta_s - \kappa_{tz}][k_i \cos\theta_s + k_i \cos\theta_i] \\
& + f_{qp}^{*} \boldsymbol{\mathfrak{G}}_{qp}^{+}(-k_{sx}, -k_{sy})[k_i \cos\theta_s + \kappa_{tsz}][k_i \cos\theta_s + k_i \cos\theta_i] \Big\} \\
+ \frac{1}{2} \Big\{ & f_{qp}^{*} \boldsymbol{\mathfrak{G}}_{qp}^{-}(-k_{ix}, -k_{iy})[k_i \cos\theta_s + \kappa_{tz}][k_i \cos\theta_s + k_i \cos\theta_i] \\
& + f_{qp}^{*} \boldsymbol{\mathfrak{G}}_{qp}^{-}(-k_{sx}, -k_{sy})[k_i \cos\theta_s - \kappa_{tsz}][k_i \cos\theta_s + k_i \cos\theta_i] \Big\}
\end{aligned} \tag{B2}$$

$$
\begin{aligned}
c = \frac{1}{16}\Big\{ & \boldsymbol{\mathfrak{F}}_{qp}^{+}\big(-k_{ix},-k_{iy}\big)\boldsymbol{\mathfrak{F}}_{qp}^{+^*}\big(-k_{ix},-k_{iy}\big)[k_i\cos\theta_s - k_{iz}][k_i\cos\theta_s - k_{iz}] \\
& + \boldsymbol{\mathfrak{F}}_{qp}^{+}\big(-k_{ix},-k_{iy}\big)\boldsymbol{\mathfrak{F}}_{qp}^{+^*}\big(-k_{sx},-k_{sy}\big)[k_i\cos\theta_s - k_{iz}][k_i\cos\theta_i + k_{sz}] \\
& + \boldsymbol{\mathfrak{F}}_{qp}^{+}\big(-k_{sx},-k_{sy}\big)\boldsymbol{\mathfrak{F}}_{qp}^{+^*}\big(-k_{ix},-k_{iy}\big)[k_i\cos\theta_i + k_{sz}][k_i\cos\theta_s - k_{iz}] \\
& + \boldsymbol{\mathfrak{F}}_{qp}^{+}\big(-k_{sx},-k_{sy}\big)\boldsymbol{\mathfrak{F}}_{qp}^{+^*}\big(-k_{sx},-k_{sy}\big)[k_i\cos\theta_i + k_{sz}][k_i\cos\theta_i + k_{sz}]\Big\} \\
+ \frac{1}{16}\Big\{ & \boldsymbol{\mathfrak{F}}_{qp}^{+}\big(-k_{ix},-k_{iy}\big)\boldsymbol{\mathfrak{F}}_{qp}^{-^*}\big(-k_{ix},-k_{iy}\big)[k_i\cos\theta_s - k_{iz}][k_i\cos\theta_s + k_{iz}] \\
& + \boldsymbol{\mathfrak{F}}_{qp}^{+}\big(-k_{ix},-k_{iy}\big)\boldsymbol{\mathfrak{F}}_{qp}^{-^*}\big(-k_{sx},-k_{sy}\big)[k_i\cos\theta_s - k_{iz}][k_i\cos\theta_i - k_{sz}] \\
& + \boldsymbol{\mathfrak{F}}_{qp}^{+}\big(-k_{sx},-k_{sy}\big)\boldsymbol{\mathfrak{F}}_{qp}^{-^*}\big(-k_{ix},-k_{iy}\big)[k_i\cos\theta_i + k_{sz}][k_i\cos\theta_s + k_{iz}] \\
& + \boldsymbol{\mathfrak{F}}_{qp}^{+}\big(-k_{sx},-k_{sy}\big)\boldsymbol{\mathfrak{F}}_{qp}^{-^*}\big(-k_{sx},-k_{sy}\big)[k_i\cos\theta_i + k_{sz}][k_i\cos\theta_i - k_{sz}]\Big\} \\
+ \frac{1}{16}\Big\{ & \boldsymbol{\mathfrak{F}}_{qp}^{+}\big(-k_{ix},-k_{iy}\big)\boldsymbol{\mathfrak{G}}_{qp}^{+^*}\big(-k_{ix},-k_{iy}\big)[k_i\cos\theta_s - k_{iz}][k_i\cos\theta_s - \kappa_{tz}] \\
& + \boldsymbol{\mathfrak{F}}_{qp}^{+}\big(-k_{ix},-k_{iy}\big)\boldsymbol{\mathfrak{G}}_{qp}^{+^*}\big(-k_{sx},-k_{sy}\big)[k_i\cos\theta_s - k_{iz}][k_i\cos\theta_i + \kappa_{tsz}] \\
& + \boldsymbol{\mathfrak{F}}_{qp}^{+}\big(-k_{sx},-k_{sy}\big)\boldsymbol{\mathfrak{G}}_{qp}^{+^*}\big(-k_{ix},-k_{iy}\big)[k_i\cos\theta_i + k_{sz}][k_i\cos\theta_s - \kappa_{tz}] \\
& + \boldsymbol{\mathfrak{F}}_{qp}^{+}\big(-k_{sx},-k_{sy}\big)\boldsymbol{\mathfrak{G}}_{qp}^{+}\ {*}\big(-k_{sx},-k_{sy}\big)[k_i\cos\theta_i + k_{sz}][k_i\cos\theta_i + \kappa_{tsz}]\Big\} \\
+ \frac{1}{16}\Big\{ & \boldsymbol{\mathfrak{F}}_{qp}^{+}\big(-k_{ix},-k_{iy}\big)\boldsymbol{\mathfrak{G}}_{qp}^{-^*}\big(-k_{ix},-k_{iy}\big)[k_i\cos\theta_s - k_{iz}][k_i\cos\theta_s + \kappa_{tz}] \\
& + \boldsymbol{\mathfrak{F}}_{qp}^{+}\big(-k_{ix},-k_{iy}\big)\boldsymbol{\mathfrak{G}}_{qp}^{-^*}\big(-k_{sx},-k_{sy}\big)[k_i\cos\theta_s - k_{iz}][k_i\cos\theta_i - \kappa_{tsz}] \\
& + \boldsymbol{\mathfrak{F}}_{qp}^{+}\big(-k_{sx},-k_{sy}\big)\boldsymbol{\mathfrak{G}}_{qp}^{-^*}\big(-k_{ix},-k_{iy}\big)[k_i\cos\theta_i + k_{sz}][k_i\cos\theta_s + \kappa_{tz}] \\
& + \boldsymbol{\mathfrak{F}}_{qp}^{+}\big(-k_{sx},-k_{sy}\big)\boldsymbol{\mathfrak{G}}_{qp}^{-^*}\big(-k_{sx},-k_{sy}\big)[k_i\cos\theta_i + k_{sz}][k_i\cos\theta_i - \kappa_{tsz}]\Big\} \\
+ \frac{1}{16}\Big\{ & \boldsymbol{\mathfrak{F}}_{qp}^{-}\big(-k_{ix},-k_{iy}\big)\boldsymbol{\mathfrak{F}}_{qp}^{+^*}\big(-k_{ix},-k_{iy}\big)[k_i\cos\theta_s + k_{iz}][k_i\cos\theta_s - k_{iz}] \\
& + \boldsymbol{\mathfrak{F}}_{qp}^{-}\big(-k_{ix},-k_{iy}\big)\boldsymbol{\mathfrak{F}}_{qp}^{+^*}\big(-k_{sx},-k_{sy}\big)[k_i\cos\theta_s + k_{iz}][k_i\cos\theta_i + k_{sz}] \\
& + \boldsymbol{\mathfrak{F}}_{qp}^{-}\big(-k_{sx},-k_{sy}\big)\boldsymbol{\mathfrak{F}}_{qp}^{+^*}\big(-k_{ix},-k_{iy}\big)[k_i\cos\theta_i - k_{sz}][k_i\cos\theta_s - k_{iz}] \\
& + \boldsymbol{\mathfrak{F}}_{qp}^{-}\big(-k_{sx},-k_{sy}\big)\boldsymbol{\mathfrak{F}}_{qp}^{+^*}\big(-k_{sx},-k_{sy}\big)[k_i\cos\theta_i - k_{sz}][k_i\cos\theta_i + k_{sz}]\Big\} \\
+ \frac{1}{16}\Big\{ & \boldsymbol{\mathfrak{F}}_{qp}^{-}\big(-k_{ix},-k_{iy}\big)\boldsymbol{\mathfrak{F}}_{qp}^{-^*}\big(-k_{ix},-k_{iy}\big)[k_i\cos\theta_s + k_{iz}][k_i\cos\theta_s + k_{iz}] \\
& + \boldsymbol{\mathfrak{F}}_{qp}^{-}\big(-k_{ix},-k_{iy}\big)\boldsymbol{\mathfrak{F}}_{qp}^{-^*}\big(-k_{sx},-k_{sy}\big)[k_i\cos\theta_s + k_{iz}][k_i\cos\theta_i - k_{sz}] \\
& + \boldsymbol{\mathfrak{F}}_{qp}^{-}\big(-k_{sx},-k_{sy}\big)\boldsymbol{\mathfrak{F}}_{qp}^{-^*}\big(-k_{ix},-k_{iy}\big)[k_i\cos\theta_i - k_{sz}][k_i\cos\theta_s + k_{iz}] \\
& + \boldsymbol{\mathfrak{F}}_{qp}^{-}\big(-k_{sx},-k_{sy}\big)\boldsymbol{\mathfrak{F}}_{qp}^{-^*}\big(-k_{sx},-k_{sy}\big)[k_i\cos\theta_i - k_{sz}][k_i\cos\theta_i - k_{sz}]\Big\}
\end{aligned}
\tag{B3}
$$

$$
\begin{aligned}
&+\frac{1}{16}\Big\{\mathfrak{F}_{qp}^{-}\left(-k_{ix},-k_{iy}\right)\mathfrak{G}_{qp}^{+^{*}}\left(-k_{ix},-k_{iy}\right)[k_i\cos\theta_s+k_{iz}][k_i\cos\theta_s-k_{tz}]\\
&\quad+\mathfrak{F}_{qp}^{-}\left(-k_{ix},-k_{iy}\right)\mathfrak{G}_{qp}^{+^{*}}\left(-k_{sx},-k_{sy}\right)[k_i\cos\theta_s+k_{iz}][k_i\cos\theta_i+k_{tsz}]\\
&\quad+\mathfrak{F}_{qp}^{-}\left(-k_{sx},-k_{sy}\right)\mathfrak{G}_{qp}^{+^{*}}\left(-k_{ix},-k_{iy}\right)[k_i\cos\theta_i-k_{sz}][k_i\cos\theta_s-k_{tz}]\\
&\quad+\mathfrak{F}_{qp}^{-}\left(-k_{sx},-k_{sy}\right)\mathfrak{G}_{qp}^{+^{*}}\left(-k_{sx},-k_{sy}\right)[k_i\cos\theta_i-k_{sz}][k_i\cos\theta_i+k_{tsz}]\Big\}\\
&+\frac{1}{16}\Big\{\mathfrak{F}_{qp}^{-}\left(-k_{ix},-k_{iy}\right)\mathfrak{G}_{qp}^{-^{*}}\left(-k_{ix},-k_{iy}\right)[k_i\cos\theta_s+k_{iz}][k_i\cos\theta_s+k_{tz}]\\
&\quad+\mathfrak{F}_{qp}^{-}\left(-k_{ix},-k_{iy}\right)\mathfrak{G}_{qp}^{-^{*}}\left(-k_{sx},-k_{sy}\right)[k_i\cos\theta_s+k_{iz}][k_i\cos\theta-k_{tsz}]\\
&\quad+\mathfrak{F}_{qp}^{-}\left(-k_{sx},-k_{sy}\right)\mathfrak{G}_{qp}^{-^{*}}\left(-k_{ix},-k_{iy}\right)[k_i\cos\theta_i-k_{sz}][k_i\cos\theta_s+k_{tz}]\\
&\quad+\mathfrak{F}_{qp}^{-}\left(-k_{sx},-k_{sy}\right)\mathfrak{G}_{qp}^{-^{*}}\left(-k_{sx},-k_{sy}\right)[k_i\cos\theta_i-k_{sz}][k_i\cos\theta_i-k_{tsz}]\Big\}\\
&+\frac{1}{16}\Big\{\mathfrak{G}_{qp}^{+}\left(-k_{ix},-k_{iy}\right)\mathfrak{F}_{qp}^{+^{*}}\left(-k_{ix},-k_{iy}\right)[k_i\cos\theta_s-\kappa_{tz}][k_i\cos\theta_s-k_{iz}]\\
&\quad+\mathfrak{G}_{qp}^{+}\left(-k_{ix},-k_{iy}\right)\mathfrak{F}_{qp}^{+^{*}}\left(-k_{sx},-k_{sy}\right)[k_i\cos\theta_s-\kappa_{tz}][k_i\cos\theta_i+k_{sz}]\\
&\quad+\mathfrak{G}_{qp}^{+}\left(-k_{sx},-k_{sy}\right)\mathfrak{F}_{qp}^{+^{*}}\left(-k_{ix},-k_{iy}\right)[k_i\cos\theta_i+\kappa_{tsz}][k_i\cos\theta_s-k_{iz}]\\
&\quad+\mathfrak{G}_{qp}^{+}\left(-k_{sx},-k_{sy}\right)\mathfrak{F}_{qp}^{+^{*}}\left(-k_{sx},-k_{sy}\right)[k_i\cos\theta_i+\kappa_{tsz}][k_i\cos\theta_i+k_{sz}]\Big\}\\
&+\frac{1}{16}\Big\{\mathfrak{G}_{qp}^{+}\left(-k_{ix},-k_{iy}\right)\mathfrak{F}_{qp}^{-^{*}}\left(-k_{ix},-k_{iy}\right)[k_i\cos\theta_s-\kappa_{tz}][k_i\cos\theta_s+k_{iz}]\\
&\quad+\mathfrak{G}_{qp}^{+}\left(-k_{ix},-k_{iy}\right)\mathfrak{F}_{qp}^{-^{*}}\left(-k_{sx},-k_{sy}\right)[k_i\cos\theta_s-\kappa_{tz}][k_i\cos\theta_i-k_{sz}]\\
&\quad+\mathfrak{G}_{qp}^{+}\left(-k_{sx},-k_{sy}\right)\mathfrak{F}_{qp}^{-^{*}}\left(-k_{ix},-k_{iy}\right)[k_i\cos\theta_i+\kappa_{tsz}][k_i\cos\theta_s+k_{iz}]\\
&\quad+\mathfrak{G}_{qp}^{+}\left(-k_{sx},-k_{sy}\right)\mathfrak{F}_{qp}^{-^{*}}\left(-k_{sx},-k_{sy}\right)[k_i\cos\theta_i+\kappa_{tsz}][k_i\cos\theta_i-k_{sz}]\Big\}\\
&+\frac{1}{16}\Big\{\mathfrak{G}_{qp}^{+}\left(-k_{ix},-k_{iy}\right)\mathfrak{G}_{qp}^{+^{*}}\left(-k_{ix},-k_{iy}\right)[k_i\cos\theta_s-\kappa_{tz}][k_i\cos\theta_s-k_{tz}]\\
&\quad+\mathfrak{G}_{qp}^{+}\left(-k_{ix},-k_{iy}\right)\mathfrak{G}_{qp}^{+^{*}}\left(-k_{sx},-k_{sy}\right)[k_i\cos\theta_s-\kappa_{tz}][k_i\cos\theta_i+k_{tsz}]\\
&\quad+\mathfrak{G}_{qp}^{+}\left(-k_{sx},-k_{sy}\right)\mathfrak{G}_{qp}^{+^{*}}\left(-k_{ix},-k_{iy}\right)[k_i\cos\theta_i+\kappa_{tsz}][k_i\cos\theta_s-k_{tz}]\\
&\quad+\mathfrak{G}_{qp}^{+}\left(-k_{sx},-k_{sy}\right)\mathfrak{G}_{qp}^{+^{*}}\left(-k_{sx},-k_{sy}\right)[k_i\cos\theta_i+\kappa_{tsz}][k_i\cos\theta_i+k_{tsz}]\Big\}\\
&+\frac{1}{16}\Big\{\mathfrak{G}_{qp}^{+}\left(-k_{ix},-k_{iy}\right)\mathfrak{G}_{qp}^{-^{*}}\left(-k_{ix},-k_{iy}\right)[k_i\cos\theta_s-\kappa_{tz}][k_i\cos\theta_s+k_{tz}]\\
&\quad+\mathfrak{G}_{qp}^{+}\left(-k_{ix},-k_{iy}\right)\mathfrak{G}_{qp}^{-^{*}}\left(-k_{sx},-k_{sy}\right)[k_i\cos\theta_s-\kappa_{tz}][k_i\cos\theta_i-k_{tsz}]\\
&\quad+\mathfrak{G}_{qp}^{+}\left(-k_{sx},-k_{sy}\right)\mathfrak{G}_{qp}^{-^{*}}\left(-k_{ix},-k_{iy}\right)[k_i\cos\theta_i+\kappa_{tsz}][k_i\cos\theta_s+k_{tz}]\\
&\quad+\mathfrak{G}_{qp}^{+}\left(-k_{sx},-k_{sy}\right)\mathfrak{G}_{qp}^{-^{*}}\left(-k_{sx},-k_{sy}\right)[k_i\cos\theta_i+\kappa_{tsz}][k_i\cos\theta_i-k_{tsz}]\Big\}
\end{aligned}
$$

where $k_{tsz}=\sqrt{{k_t}^2-{k_{sx}}^2-{k_{sy}}^2}$.

Yuan LIU

Analyse de sensibilité et estimation de l'humidité du sol à partir de données radar

Résumé

L'étude de la diffusion des ondes électromagnétiques par une surface rugueuse aléatoire est de première importance dans de nombreuses disciplines et conduit à diverses applications notamment pour le traitement des surfaces par télédétection. En connaissant les modes de rétrodiffusion, on peut détecter la présence de la rugosité aléatoire indésirable de la surface de réflection telle que le réflecteur d'antenne et par conséquent trouver un moyen de corriger ou compenser les erreurs de phase. Cette thèse porte sur l'obtention de l'humidité du sol de surface à partir de mesures radar. La description de la surface rugueuse de façon aléatoire est présentée, suivie par les interactions d'ondes électromagnétiques avec les média. En particulier, un modèle d'équation intégrale avancé (AIEM) est introduit. La validité du modèle AIEM, qui est adopté comme modèle de travail, se fait par une large comparaison avec des simulations numériques et des données expérimentales. On analyse également les caractéristiques des configurations radar bistatique et on étudie la sensibilité de la diffusion bistatique à l'humidité du sol et à la rugosité de surface et, dans le même temps, le cadre de la détermination de l'humidité du sol à partir de mesures radar utilisant un réseau de neurones àbase de filtres de Kalman récurrents est présenté. La formation du réseau et l'inversion des données sont décrits.

Résumé en anglais

Electromagnetic waves scattering from a randomly rough surface is of palpable importance in many fields of disciplines and bears itself in various applications spanned from surface treatment to remote sensing of terrain and sea. By knowing the backscattering patterns, one may detect the presence of the undesired random roughness of the reflection surface such as antenna reflector and accordingly devise a means to correct or compensate the phase errors. Therefore, it has been both theoretically and practically necessary to study the electromagnetic wave scattering from the random surfaces. This dissertation focuses on the retrieval of surface soil moisture from radar measurements. The description of the randomly rough surface is presented, followed by the electromagnetic wave interactions with the media. In particular, an advanced integral equation model (AIEM) is introduced. The validity of the AIEM model, which is adopted as a working model, is made by extensive comparison with numerical simulations and experimental data. Also analyzes the characteristics of the bistatic radar configurations and dissects the sensitivity of bistatic scattering to soil moisture and surface roughness of soil surfaces. Meanwhile presents a framework of soil moisture retrieval from radar measurements using a recurrent Kalman filter-based neural network. The network training and data inversion are described in detail.